


# IMPROVED MODELING OF STRUCTURAL JOINT DAMPING

THESIS

Gregory L. Leiker
Captain, USAF

AFIT/GAE/AA/86D-9



DEPARTMENT OF THE AIR FORCE
AIR UNIVERSITY
AIR FORCE INSTITUTE OF TECHNOLOGY

Wright-Patterson Air Force Base, Ohio

AFIT/GAE/AA/86-9



# IMPROVED MODELING OF STRUCTURAL JOINT DAMPING

THESIS

Gregory L. Leiker
Captain, USAF

AFIT/GAE/AA/86D-9

AFIT/GAE/AA/86D-9

# IMPROVED MODELING OF STRUCTURAL JOINT DAMPING

THESIS

Presented to the Faculty of the School of Engineering

of the Air Force Institute of Technology

Air University

in Partial Fulfillment of the

Requirements for the Degree of

Master of Science in Aeronautical Engineering




Gregory L. Leiker, B.S.

Captain, USAF


December 1986

Approved for public release; distribution unlimited

## Acknowledgements

I would like to express my sincere gratitude to Major Terry Hinnerichs for his continuous support, technical guidance, thought provoking questions, and many hours of discussion that saw me through to the completion of this project.

I would also like to express my sincerest gratitude and affection to my wife, Renee', who was often the target of my frustration in the early failings of this thesis, but was always there with a kind word and offer to help when I needed it most.

Gregory L. Leiker

A Columbia Personal Computer (IBM compatible) was used to complete this thesis. The word processing package used was Chiwriter by Horstmann Software Design. The printer used was a Panasonic KX-1091.

## Table of Contents

## List of Figures

## Abstract

The purpose of this thesis is to develop a better model of damping that occurs in structural joints due to coulomb friction when rotational slip occurs in the joints. A one-dimensional, indirect formulation, of the Boundary Element Method (BEM) is developed to calculate the displacement, rotation, moment and shear in beams which obey the assumptions of simple beam theory. This BEM code is then modified to account for friction damping at the joint of two beams due to a relative rotation between them. A gross slip model of the friction in the joint is used to establish basic behavior of the beam joint with friction damping. Next, a micro-slip model of friction is developed. The micro-slip model, depending on the applied moment, allows for the elastic rotation of the joint up to some threshold moment where partial slip begins. As the applied moment increases the region of partial slip expands until the entire joint is slipping and the gross slip condition exists.

Both the gross slip model and the micro-slip model of the joint friction are used to obtain measures of energy loss per cycle versus clamping pressure in the joint. Load controlled and deflection controlled loading cycles are used to exercise the joint in a quasi-dynamic model and generate

hysteresis loops in both force-diplacement and moment-rotation space.

The clamping pressure was varied between 0 Ksi and 20 Ksi. The energy loss per cycle curves generated show that there is a range of clamping pressures for which the energy loss per cycle curve reaches a peak for a given loading and amplitude of vibration.

The micro-slip model developed herein shows better behavior than the gross slip model both above and below the moment which causes gross slip. The hysteresis loops generated in both the load-deflection and moment-rotation space are comparable to other published data, however the allowance for the breakaway moment before partial slip begins seems to give a more conservative estimate of the energy loss per cycle for a given clamping pressure.

# IMPROVED MODELING OF STRUCTURAL JOINT DAMPING

## I. Introduction

### 1.1 Background.

The advent of a space based strategic defense and the increased push for a permanent space station by the year 2000 has caused an increased interest in the stability of large space structures. These structures must have sufficient damping to keep the vibration response within acceptable limits. In strategic defense applications demanding requirements will be placed on the load bearing structures supporting missile defense hardware. Presumably this hardware will create wide bandwidth high magnitude mechanical disturbances while generating power for the missile destroying mechanism. Structures will also be required to support the large rapidly rotating targeting mirrors which are called for in some defense schemes. These structures will need to make use of active as well as passive damping techniques to meet the requirements of disturbance isolation and target alignment.

The response of a structure to broad band excitation is known to be dominated by contributions at and near its

resonance (19). The amplitude of response of a system at resonance is governed by the damping characteristics of the system (11). Therefore, the response of a system to a broad band excitation will depend on the damping characteristics of the system.

A primary source of damping in all structures consisting of more than one discrete component is the damping that occurs as a result of the interface slip between components at their joints. Beards estimates that as much as 90 percent of the damping in structures takes place in the joints (3). Unfortunately, the current design of structures makes use of low mass materials and welded construction which eliminates the inherent damping mechanisms available to structures and as a result, complex artificial damping mechanisms are required to provide stability (2).

The damping which occurs in joints as a result of interface slip is called friction damping or Coulomb damping. Given that friction damping is the primary source of damping in structures, it provides the greatest potential increase in structural damping. Friction damping in joints has specific advantages. First, by using friction damping in joints as a source of energy dissipation, the use of complex artificial damping systems can be reduced. Second, by using friction damping in joints, the original geometry can be maintained. Finally, friction damping is low cost and has the potential for high energy dissipation (8).

Beards points to three reasons why this source of damping has not been used. First, the possibility of fretting corrosion which ultimately causes failure of the joint and potentially the entire structure. Second, it reduces the stiffness of the overall structural system. Finally, the nonlinearity of the friction problem presented problems in analysis (3).

The benefits gained by friction damping in joints can no longer be overlooked and the disadvantages of allowing friction in the joint can be overcome or reduced. The surface preparation of the contact surfaces can reduce the effects of fretting corrosion while still maintaining good energy dissipation characteristics (4). The overall stiffness characteristics of the structure can be maintained if joints are allowed to slip in rotation and not in translation (5). New and innovative methods are being developed to analyze the nonlinear nature of the Coulomb friction damping.

1.2 Purpose.

The purpose of this thesis is to develop a better model of the damping that occurs in structural joints due to Coulomb friction when rotational slip occurs in the joints.

1.3 General Approach.

A one-dimensional Boundary Element Method (BEM) is used to symmetrically model a two beam system with a frictional joint located at the point of symmetry. A bilinear gross slip model and a nonlinear micro-slip model of the joint

friction are used to obtain measures of energy loss per cycle versus clamping pressure in the joint. Load controlled and deflection controlled loading cycles are used to exercise the joint in a quasi-dynamic model and generate hysteresis loops in both force-displacement and moment-rotation space. Figure 1.1 shows the two beam geometry and the symmetric case BEM models used in the development.

A literature search showed that interest in the field of friction damping has been around for a long time but that the difficulty of experimentally verifying results and the nonlinear nature of the friction problem caused the consideration of friction to be ignored in most vibration data. A considerable amount of work is being done in the area of BEM but this is the first work done with BEM in the area of frictional damping due to rotational slip in structural joints.

This thesis is presented in six chapters. The present chapter seeks only to familiarize the reader with the basic problem and the solution procedure. Chapter 2 sets forth the basic assumptions and theory associated with Coulomb friction, beam theory, and the Boundary Element Method. Chapter 3 discusses the development of the gross slip model and the micro-slip model and their implementation in the BEM. Chapter 4 presents the results of the gross slip and micro-slip calculations for both the force and displacement controlled loading. Chapter 5 discusses the conclusions

drawn from the results and Chapter 6 provides recommendations for further study. In addition, there is an appendix which presents the BEM calculations for several base line test cases associated with the beam used in the friction models without the Coulomb friction joint.

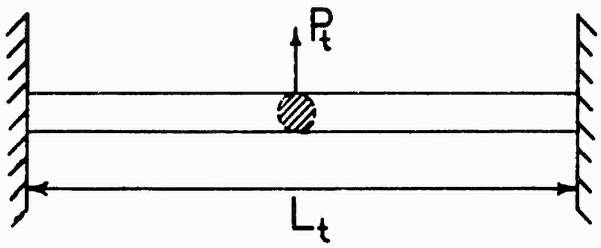


FIGURE 1-1a OVERALL MODEL GEOMETRY

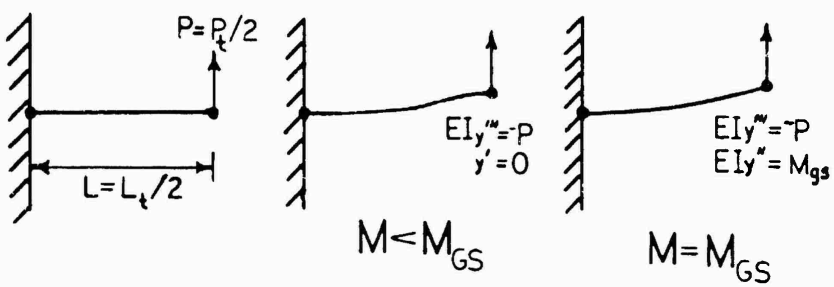


FIGUKE 1-1b SYMMETRIC GEOMETRY--BILINEAR MODEL

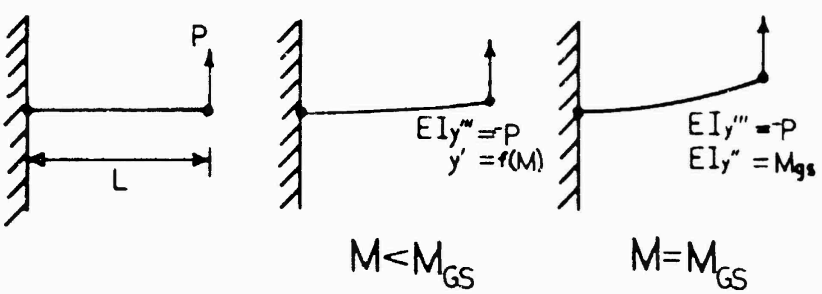


FIGURE 1-1c SYMMETRIC GEOMETRY--NONLINEAR MODEL

# II. Theory

## 2.1 Coulomb Damping Theory.

Coulomb or sliding friction forces arise whenever two or more bodies in contact with each other move relative to one another along a common dry surface. The friction force acts parallel to the contact surface. It is a dissipative force because the force of friction always opposes the relative motion of the objects in contact. The classical law of friction states that the frictional force is directly proportional to the normal force $N$, but is independent of the contact area and magnitude of the relative velocity so long as sliding exists (9). The force of friction $F_f$ as presented by Greenwood is:

$$F_f = -\mu N \, \mathrm{sgn}(v_r) \qquad (2\text{-}1)$$

where

$F_f$ = force of friction
$\mu$ = coefficient of sliding friction
$N$ = normal force
$v_r$ = relative velocity
$\mathrm{sgn}(v_r)$ = $\pm 1$ depending on sign of $v_r$

The coefficient of sliding friction $\mu$ depends only on the roughness of the sliding surfaces and the materials used (9). The function $\mathrm{sgn}(v_r)$ has the value of $\pm 1$ depending on the sign of the relative velocity $v_r$ such that the force of

friction always opposes the motion. For instance if $v_r$ is positive then $\text{sgn}(v_r)$ is also positive and $F_f$ is negative.

2.1.1 Spring-Mass Model. The motion of a system with a Coulomb friction damping force acting can be demonstrated with a spring-mass model. Consider the system shown in Figure 2.1. A block with mass m sits on a surface such that a coefficient of sliding friction $\mu$ exists between the block and the surface. A linear spring with stiffness k is attached to the mass to provide restoring forces against motion away from equilibrium. The damping force is given as:

$$F_d = \mu\, m\, g \qquad (2\text{-}2)$$

where

$F_d$ = damping force equals $F_f$
m = mass
g = acceleration of gravity

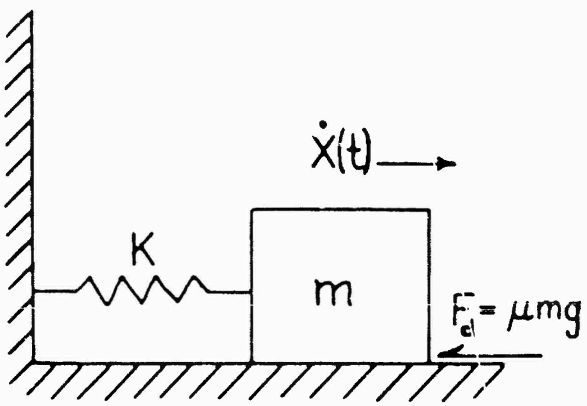


FIGURE 2-1 SPRING-MASS SYSTEM WITH FRICTION

With the system so defined, Meirovitch (14) gives the equation of motion as:

$$m\ddot{x} + F_d sgn(\dot{x}) + kx = 0 \qquad (2\text{-}3)$$

where

$\ddot{x}$ = acceleration of the mass
$\dot{x}$ = velocity of the mass
k = spring stiffness

The equation of motion is nonlinear because of the switching in the sign due to the $sgn(\dot{x})$ function. This nonlinear equation of motion can be separated into two linear equations of motion, each valid for a specific range of velocities (14). These equations are:

$$m\ddot{x} + kx = -F_d \qquad \dot{x} > 0 \qquad (2\text{-}4)$$

$$m\ddot{x} + kx = F_d \qquad \dot{x} < 0 \qquad (2\text{-}5)$$

It should be noted that the switching does not occur as an explicit function of time but is determined by the response of the system and could occur at various times depending on the forcing function and initial conditions (8). The solution of the equations of motion must take place over one time interval depending on the sign of $\dot{x}$.

For the purposes of this paper the specifics of the dynamic behavior are not investigated. However, some characteristics of the behavior are of interest and prove useful in the analysis of results.

The response of the system with Coulomb friction damping consists of a harmonic component and a constant

component superimposed on each other much the same way as in viscous damping, however here the decay envelope is linear in time as shown in Figure 2.2. The natural frequency of


FIGURE 2-2 FREE VIBRATION WITH COULOMB DAMPING (17)

Coulomb damped systems is the same as the natural frequency for free vibration and is given as:

$$\omega_{\mu} = \sqrt{k/m} \qquad (2\text{-}6)$$

suggesting that unlike viscous damping, which dissipates energy as a linear function of frequency of oscillation, Coulomb friction damping energy dissipation is independent of the frequency (17). The change in amplitude per cycle is a constant and equal to:

$$X_1 - X_2 = \frac{4F_d}{k} \qquad (2\text{-}7)$$

where $X_1$ and $X_2$ are the amplitudes of successive peaks as in Figure 2.2 and the term $4F_d/k$ defines the envelope of decay. Thomson (17) defines the energy lost per cycle due to

damping force as:

$$W_d = \oint F_d dx \qquad (2\text{-}8)$$

which upon integration yields

$$W_d = 2F_d(X_1 + X_2) \qquad (2\text{-}9)$$

where

$W_d$ = energy loss per cycle

Equation 2-8 allows the calculation of amplitude decay per cycle given the energy loss per cycle and the damping force.

2.1.2 The Rotating Circular Shaft. As an aid in considering the friction in a clamped joint, it is helpful to consider first the more general case of sliding friction arising from a frictional shear stress equal to $\mu$ times the normal force $N$, at the contact area of a rotating shaft of radius $R$, pressed against a plane surface (9). Assuming a uniform normal pressure at the contact area $\mathcal{A}$, there is a uniform frictional stress of magnitude:

$$\tau_f = \frac{\mu N}{\pi R^2} \qquad (2\text{-}10)$$

which is everywhere in direction normal to a radial line drawn from the center of the circular contact area (9). Figure 2-3 shows the circular contact area as well as the shear stress distribution on that surface. The incremental moment due to an annular element of width dr and area $2\pi r dr$

is:

$$dM = \frac{\mu N}{\pi R^2} 2 \pi r^2 dr \qquad (2\text{-}11)$$

which can be integrated to find the total frictional moment

$$M = \frac{2\pi N}{R^2} \int_0^R r^2 dr = \frac{2}{3} \mu N R \qquad (2\text{-}12)$$

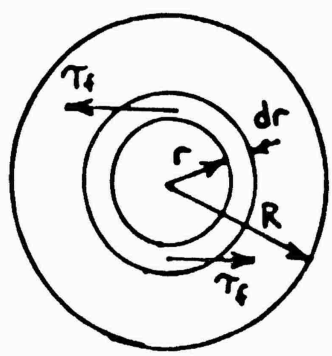


FIGURE 2-3 FRICTIONAL SHEAR STRESS ON A ROTATING CIRCULAR SURFACE

If $\mu = 0$, the contact surface is said to be perfectly smooth. If $\mu = \infty$, a perfectly rough surface is present. The first of these conditions corresponds to the no-clamp case in which the friction force is zero. The second case allows no relative velocity at the contact surface and is

referred to as the no-slip case (9). It is important to realize that in the first case no frictional force is present while in the second case the potential for a resisting frictional force is so great that the transition from static frictional force to a kinetic frictional force is not possible. As the load builds up to force motion in one direction, a static force of friction builds up in the other which causes static equilibrium to be maintained. For values of $\mu$ between these two extremes the static friction force builds up to a peak value and if the applied load exceeds this peak value of static friction, the entire contact surface of the joint begins to slip. The contact surfaces of the joint move relative to one another and this relative motion is resisted by Coulomb friction forces. As an extension to this analysis to the case of the friction damping in structural joints, the model developed by Richardson and Nolle has been referenced in many published articles.

2.1.3 The Richardson And Nolle Model. The Richardson and Nolle Model is a micro-slip model. A micro-slip model allows partial slip in the outer joint radius while the inner joint radius behaves like a rigid body.

The joint under consideration consists of two elastic members in contact over a circle of radius $R$ (see Figure 2-4). A constant force is applied normal to the contact surface resulting in a uniform clamping pressure $P^*$ throughout the joint. As seen in Figure 2-4 moments are

applied about the joint axis. These moments about the joint axis cause friction shear stresses to build up at the interface and micro-slip displacement between the two members occurs (15).

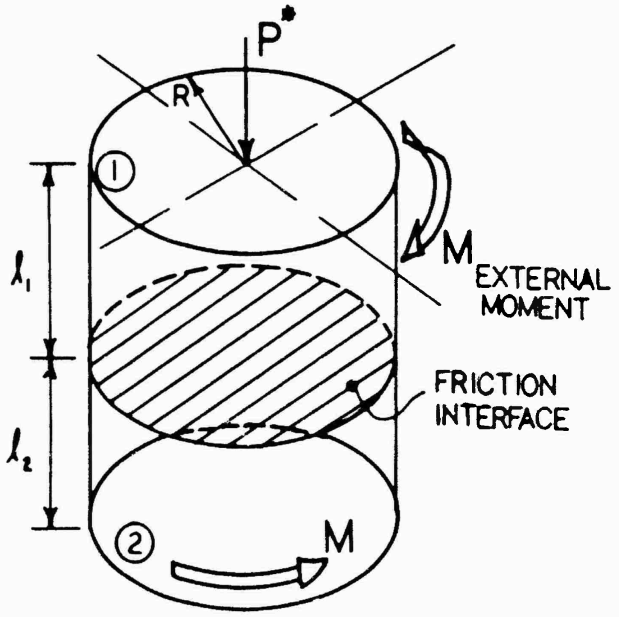


FIGURE 2-4 FRICTION JOINT LOADED BY EXTERNAL MOMENT(15)

The analysis proceeds on the basis of the following assumptions as stated by Richardson and Nolle:

1. The external moment is transferred between the two bodies by shear stresses due to friction.
2. The friction shear stress is of constant magnitude, given by $\mu P^*$, and exists only in those parts of the contact surface over which relative slip has occurred.
3. There are no surface shear stresses in regions where slip has not occurred.

4. There is no twisting of initially axial elements.
5. The deformation takes the form of a relative rotation between concentric cylinders of material of differing diameter and does not resemble that of an elastic shaft in torsion. (15)

The reason behind these assumptions is to relate the externally applied moment to a region of slip in the joint. The build-up of frictional shear stresses which causes the slip starts at the outer radius R and proceeds inward to that radius $a$ which balances the internal moment caused by the frictional shear stress in the slipped region and the external moment. These frictional shear stresses create a shear strain and thus a relative rotation in the joint which dissipates energy. Figure 2-5 shows the slipped region for a particular value of externally applied moment. A value of moment greater than that shown will decrease $a$ while a moment value less than that shown will increase $a$.

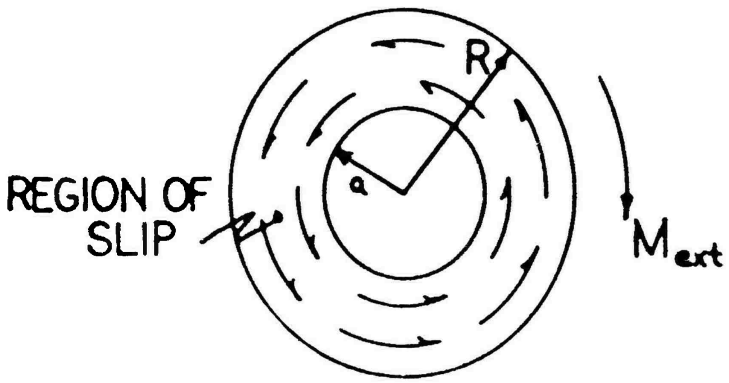


FIGURE 2-5 SLIPPED REGION AND DISTRIBUTION OF SHEAR STRESSE.

The full load cycle is considered in three parts, the initial loading, the unloading and the reloading. Each of these regions has its own set of governing equations which relate the applied moment to the region of slip and thus to relative rotation.

The initial loading phase need only be considered for the first quarter cycle of the loading and need not be considered again no matter how many cycles are run. The external moment is taken from a value of 0 to a value of $M_{max}$. The inner bounding radius is found from equilibrium of moments stated as follows:

$$M_{ext} - M_{fric} = 0 \tag{2-13}$$

where

$$M_{fric} = \int_{a}^{R} 2\pi r^2 \mu P^* dr \tag{2-14}$$

which upon integration and rearrangement yield

$$a^3 = R^3 - \frac{3 M_{ext}}{2\pi\mu P^*} \tag{2-15}$$

The Richardson and Nolle development requires that the external moment applied to the joint be equal to or less than the value for gross slip. By setting $a = 0$ the external moment which causes gross slip is found to be:

$$M_{gs} = \frac{2}{3} \pi \mu P^* R^3 \qquad (2\text{-}16)$$

This is the maximum moment which the joint can support. For values of moment between 0 and $M_{gs}$ Richardson and Nolle develop an equation which describes the relative rotation in the joint. Assuming that the material which has not slipped behaves as a rigid body, they calculate the net moment acting at any radius $r$ between $a$ and $R$. Using elasticity equations in polar coordinates, this net moment is equated to a circumferential shear strain which is in turn equated to displacement in the circumferential direction. The equation for the displacement in the circumferential direction is given as:

$$v_1(r) = (\mu P^* r^2 / 6 l_1 G_1)[2-3(a/r)+(a/r)^3] \qquad (2\text{-}17)$$

where the subscript 1 denotes that this is the displacement in body 1 of Figure 2-4 (15). The value $l_1$ is a geometric property of the joint and determines the length over which the shear stress were distributed and the value $G_1$ is the shear modulus of the material. To maintain rotational equilibrium in the whole joint, the moment in body 2 at any radius $r$ is equal and opposite to that in body 1 and thus the equation for $v_2$ is identical to that of $v_1$ except that the sign is opposite to that in $v_1$. Thus we have:

$$v_2(r) = -(\mu P^* r^2 / 6 l_2 G_2)[2-3(a/r)+(a/r)^3] \qquad (2\text{-}18)$$

The relative rotation between body 1 and body 2 at a radius $r$ is defined as $v_1(r)-v_2(r)$. The relative rotation, $\phi$, across the joint is defined arbitrarily at the outer radius $R$ (15). Figure 2-6 shows the relative circumferential displacement and $\phi$.

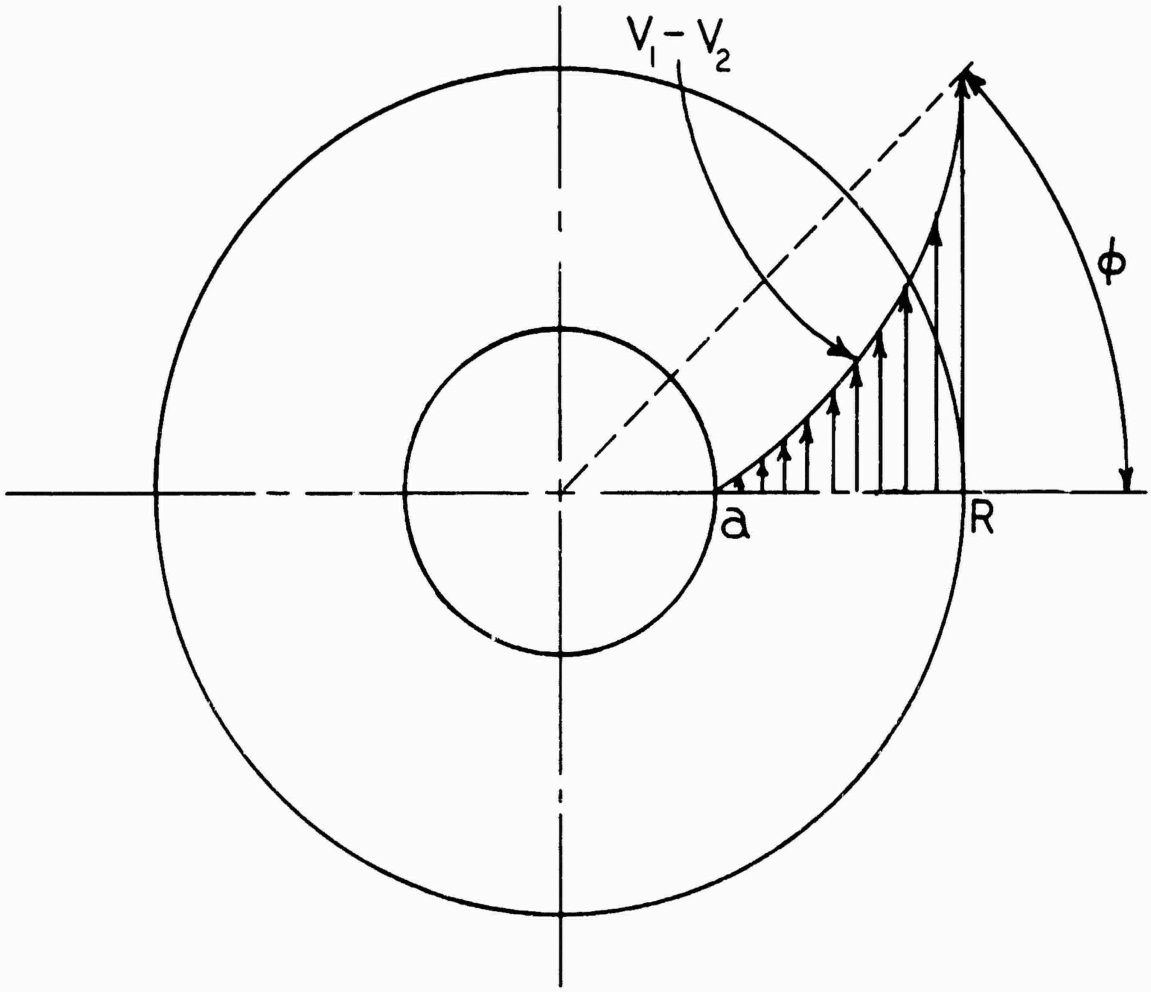


FIGURE 2-6 RELATIVE CIRCUMFERENTIAL DISPLACEMENT AND $\phi$ (15)

The final step in the development is to integrate the equation for $\phi$ over the entire slipped region:

$$\phi = \left[\frac{1}{I_1 G_1} - \frac{1}{I_2 G_2}\right] \int_a^R \frac{T_1(r)}{2\pi r}\, dr \qquad (2\text{-}19)$$

where for simplicity the term in front of the integral is defined as $S$ and $T_1(r)$ is defined as the net moment acting at radius r (15). The solution of this integral gives the rotation in the joint as:

$$\phi = (\mu P^* R/6S)[2-3(a/R)+(a/R)^3] \qquad (2\text{-}20)$$

where $a$ is given by equation 2-15. At the end of the initial loading $M = M_{max}$ which is less than $M_{gs}$. The radius associated with the slipped region at $M_{max}$ is designated $a_m$ and $\phi = \phi_{max}$.

This development is similar for the unloading and reloading regions of the curve. During unloading the joint undergoes counterslip from $\phi_{max}$ to $\phi_{min}$. The slip region proceeds again from the outer radius $R$ inward to some radius $\delta$. The equation for $\phi_{ul}$ is dependent on both the radius $a_m$ and the newly determined radius $\delta$. At the time when M equals $M_{min}$ the rotation is designated $\phi_{min}$ and the radius is designated $\delta_m$. The equation developed by Richardson and Nolle is given as:

$$\phi_{ul} = (\mu P^* R/6S)[-2-3(a_m/R) + (a_m/R)^3 + 6(\delta/R) - 2(\delta/R)^3] \qquad (2\text{-}21)$$

which at $\delta = R$ simplifies to equation 2-20 (15).

During the reloading phase of the cycle the equation for $\phi_{rl}$ is dependent on the two previous regions of slip and one expects to see the terms $a_m$ and $\delta_m$ in the governing equation. Physically the dependence of the equation for $\phi_{ul}$ on $a_m$ and the dependence of $\phi_{rl}$ on both $a_m$ and $\delta_m$ is a measure of the residual stresses which are locked in when the external loading moment reaches a peak and begins to reverse direction. Figure 2-7 is a picture of the physics of an entire cycle from initial loading to the completion of reloading.

Note, that after the completion of initial loading, residual shear stresses are locked in producing a residual moment in the joint. During the unloading phase these residual stresses are negated and a residual stress and corresponding residual moment are again locked in, acting in the opposite direction to those of the initial loading. Here the region of slip in the unloading is shown not to have exceeded that produced in the initial loading. This condition is not necessarily the case and for a general loading function the slipped region during unloading may exceed that of initial loading. The reloading phase is very similar to that of the unloading except now equilibrium is balanced between the externally applied moment, the frictional moment, and two locked in residual moments.

The energy dissipated by the cyclic loading can be determined by calculation of the area enclosed in a moment-

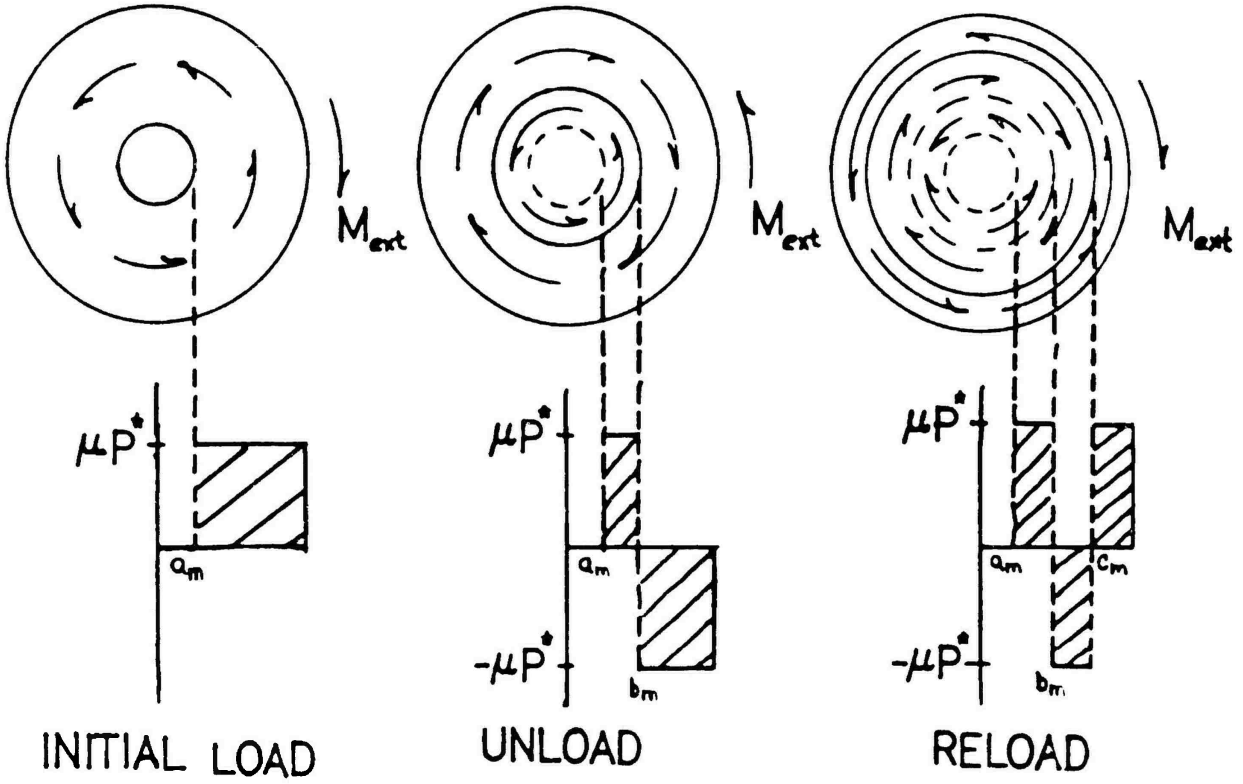


FIGURE 2-7 PHYSICAL INTERPRETATION OF RICHARDSON AND NOLLE MODEL

rotation diagram (M-$\theta$ diagram) as shown in Figure 2-8 and is represented by the equation:

$$\Delta E = \int_{M_{min}}^{M_{max}} (\phi_{ul} - \phi_{rl}) dM \qquad (2\text{-}22)$$

where the $\phi_{ul}$ and $\phi_{rl}$ are as defined by Richardson and Nolle in Reference 15.

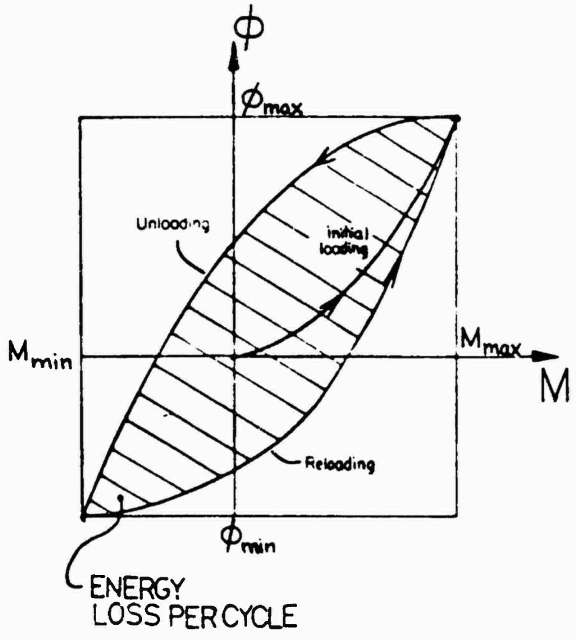


FIGURE 2-8 M-$\theta$ DIAGRAM FOR RICHARDSON AND NOLLE MODEL (15)

2.1.4 Gross Slip Model. As a first attempt at modelling the behavior of friction in a joint it is common to use a gross slip model. Such a model assumes that no rotation occurs in the joint until the value of the externally applied moment reaches the value of $-M_{gs}$ as defined in equation 2-16. The joint then rotates through an angle $\phi$ and the moment is limited to a maximum value of $-M_{gs}$ until the cycle reverses itself and then the value of $-M_{gs}$ and $\phi_{max}$ are locked in.

During unloading the joint again undergoes no rotation until a value of $+M_{gs}$ is reached and again the joint rotates to a value of $\phi_{min}$ while a value of $+M_{gs}$ is maintained until the applied moment reverses direction. The process reverses for the reloading case. The $+M_{gs}$ is locked in as well as the rotation $\phi_{min}$ until the external moment reaches a value of $-M_{gs}$ when again rotation is allowed to

occur. This model produces a square M-$\theta$ diagram as shown in Figure 2-9. Note, the direction of the cycle can be reversed without loss of generality.

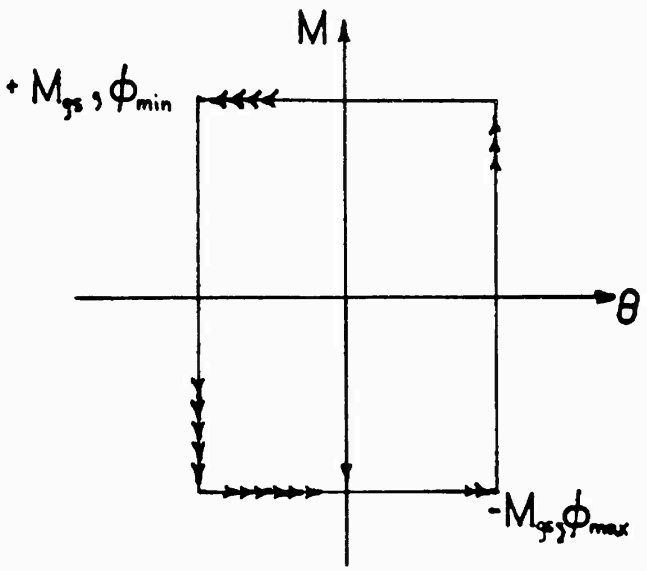


FIGURE 2-9 M-$\theta$ DIAGRAM FOR GROSS SLIP MODEL

The specifics of this model are discussed in more detail in Chapter 3. For now we will move on to describe the theory behind the equations used to model the beams which are connected at the joint.

2.2 Elementary Beam Theory.

2.2.1 Euler-Bernoulli Beam Theory. The beam under consideration in this analysis is generally referred to as

an Euler-Bernoulli beam and several key assumptions are necessary in order for the analysis to have any meaning. Therefore, the following assumptions are made:

1. Plane sections remain plane under conditions of bending.
2. The beam has linear elastic material properties and is homogeneous.
3. The beam undergoes pure bending with no local distortions and neglects the effects of shear.
4. The geometric properties of the beam are constant along the length.
5. Bending of the beam occurs in a single plane.

In addition to the above assumptions it is generally assumed that the loading is static in nature. To avoid confusion in the development of the governing equations and to better understand the nature of the loading in the beam it is advantageous to define a consistent sign convention to be used throughout the rest of this analysis. Figure 2-10 shows the sign convention chosen for this analysis. A positive moment causes compression in the top fibers of the beam and negative moment causes tensile loading in the top fibers. If the normal vector from the cut beam face, $\eta$, is in the $+x$ direction and the reaction at the cut is acting in the $-y$ direction, the shear is positive. Likewise, when $\eta$ is acting in the $-x$ direction and the reaction is $+y$, the shear is positive. External transverse loads are considered positive in the $+y$ direction.

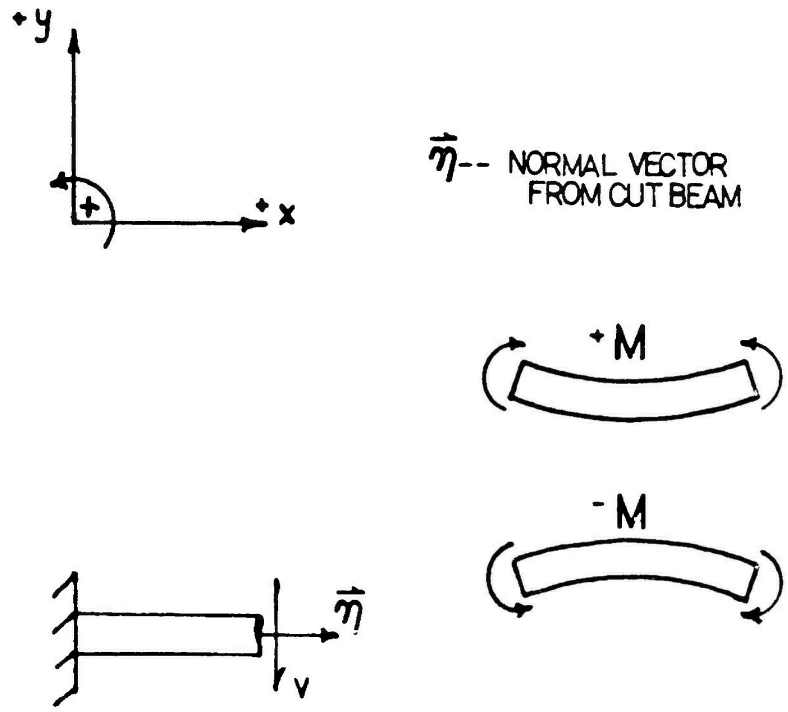


FIGURE 2-10 THE SIGN CONVENTION FOR BEAM ANALYSIS

2.2.2 Built-In Beam Problem. The geometry of the joint friction problem before slip occurs in the joint is that of a built-in beam shown in Figure 2-11. This is a statically indeterminate problem and must be solved in a piecewise fashion using the fourth order beam equation. Griffel has tabulated the results for a number of beam loading geometries and, as seen in Figure 2-11, has plotted the shear and moment diagrams for the specific case under consideration (10). It can be seen that at the midpoint of the beam a point of symmetry exists.

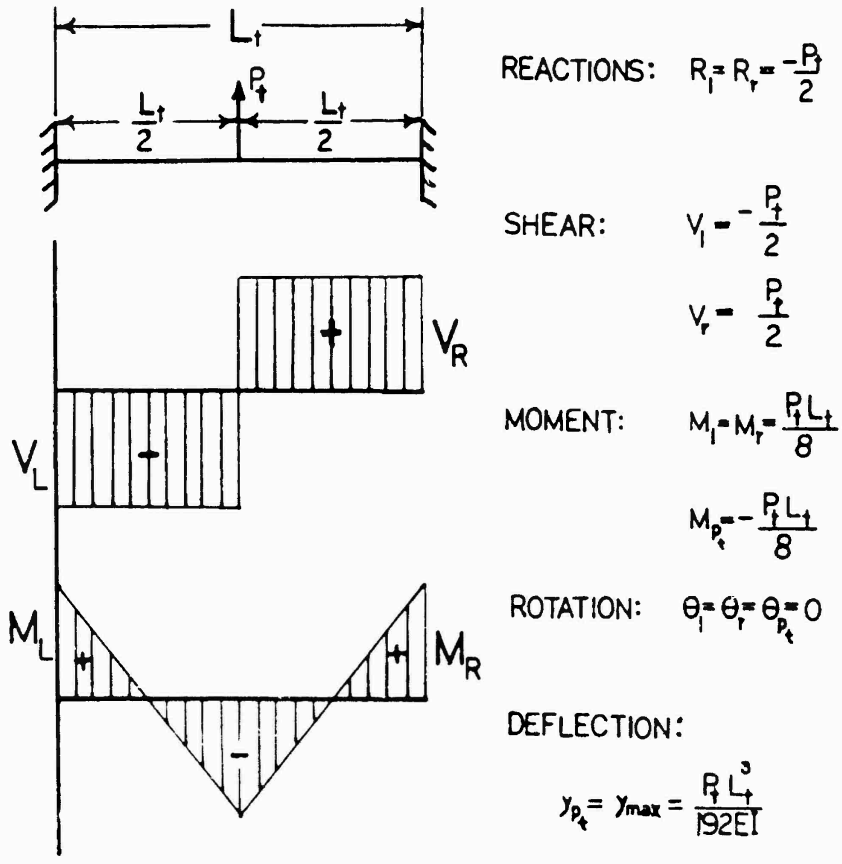


FIGURE 2-11 BUILT-IN BEAM GEOMETRY AND ANALYSIS (6)

The symmetric case of the built-in beam problem is the geometry that we will use in the analysis of the friction damping of a rotary structural joint. Figure 2-12 shows the geometry and loading of this beam. The boundary conditions for the left end of the beam are $y(0)=0$ and $y'(0)=0$ and

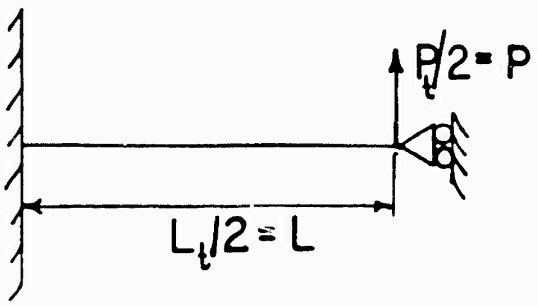


FIGURE 2-12 SYMMETRIC BUILT-IN BEAM GEOMETRY AND LOADING

the boundary conditions at the right end are $y'''(L_t/2) = -P_t/2$ and $y'(L_t/2)=0$. Here $y'$ denotes $dy/dx$ and $y''$ denotes $d^2y/dx^2$ and so forth. The subscript "t" in the statement of the boundary conditions refers to the "total" built-in beam geometry and loading to distinguish it from the symmetric beam geometry and loading. The solution to this problem in terms of the "total" beam geometry, using the fourth order Euler-Bernoulli beam equation, yields the following results:

$$EIy''' = -P_t/2 \qquad (2\text{-}23a)$$

$$EIy'' = -\frac{P_t x}{2} + \frac{P_t L_t}{8} \qquad (2\text{-}23b)$$

$$EIy' = -\frac{P_t x^2}{4} + \frac{P_t L_t x}{8} \qquad (2\text{-}23c)$$

$$EIy = -\frac{P_t x^3}{12} + \frac{P_t L_t x^2}{16} \qquad (2\text{-}23d)$$

where

$P_t$ = the load applied to the built-in beam

$L_t$ = the length of the built-in beam

To avoid confusion, the load applied to the symmetric beam is designated $P$ and the length of the symmetric beam is designated $L$. Thus, the relationship between the built-in beam geometry and loading and the symmetric beam geometry and loading is given as:

$$P = P_t/2 \qquad (2\text{-}23e)$$

$$L = L_t/2 \qquad (2\text{-}23f)$$

Equations 2-23a through 2-23d can be written in terms of the symmetric beam geometry and loading as:

$$EIy''' = -P \qquad (2\text{-}24a)$$

$$EIy'' = -P\,x + \frac{P\,L}{2} \qquad (2\text{-}24b)$$

$$EIy' = -\frac{P\,x^2}{2} + \frac{P\,L\,x}{2} \qquad (2\text{-}24c)$$

$$EIy = -\frac{P\,x^3}{6} + \frac{P\,L\,x^2}{4} \qquad (2\text{-}24d)$$

These equations are used to construct the shear and moment diagrams for the symmetric built-in beam analysis. Figure 2-13 shows the shear and moment diagrams.

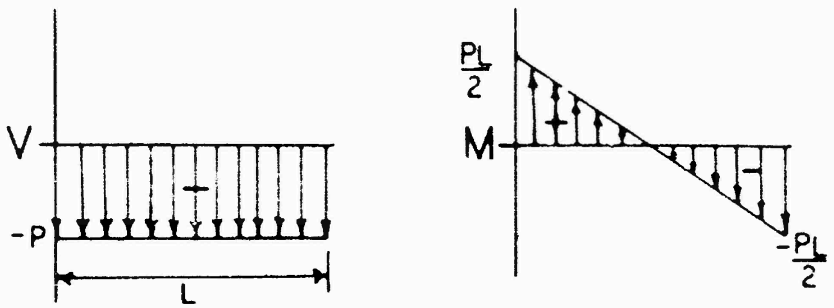


FIGURE 2-13 SHEAR AND MOMENT DIAGRAMS FOR SYMMETRIC BUILT-IN BEAM

As expected, the shear and moment diagrams for the symmetric case match the results as given by Griffel. Having the solution to the built-in beam symmetric case we can now move on to the development of the Boundary Element theory.

## 2.3 Indirect Direct Boundary Element Method.

2.3.1 Boundary Elements vs. Finite Elements. As a brief introduction to the Boundary Element Method (BEM) it is helpful to compare this method to the more familiar finite element method (FEM). The finite element method seeks to solve a series of differential equations by approximating the solution to these differential equations at all interior points of the domain in which they apply. The solution at the boundary of the domain may or may not be exact. The boundary element method seeks to solve the same set of differential equations exactly at all interior points of the domain and approximate the solution at the boundary. Sometimes the former is referred to as domain method and the latter as a boundary method.

The boundary element method, sometimes called the boundary integral equation method, solves the differential equations by transforming them into equivalent integral equations. Like the solution to any integral, the answer is obtained by evaluation of the integral at the upper and lower limits of integration - the boundary elements. Of course this is a crude explanation of an elegant method, but it allows one to visualize physically what the method does. The boundary element method reduces the dimensionality of

the problem by one (6). For instance, a three-dimensional problem, as in stress analysis of solids, is reduced to a two-dimensional problem; a two-dimensional problem, such as the stress analysis of a membrane, is reduced to a one-dimensional problem; and a one-dimensional problem, as in the analysis of beams, is reduced to the solution of a point problem. Figure 2-14 shows, for a two-dimensional problem, the one-dimensional nature of the boundary element model and for a one-dimensional problem, the point nature of the boundary element model.

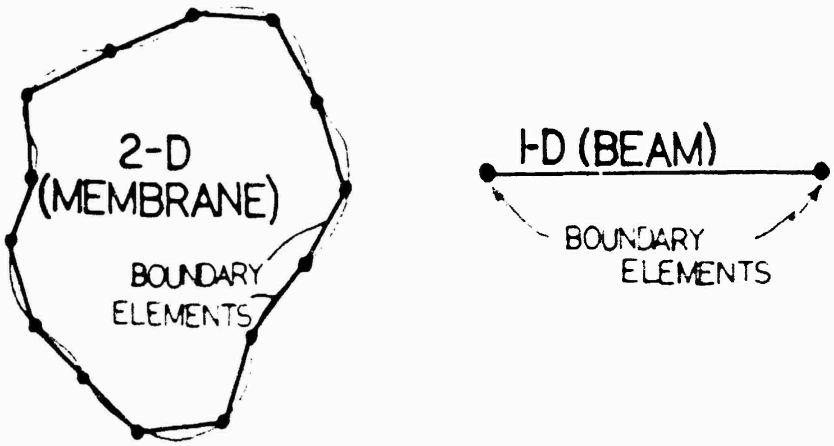


FIGURE 2-14 REDUCTION OF DIMENSIONALITY USING BEM

As far as the numerical calculations go, the boundary element method has no great advantage over the finite element method for one-dimensional and low order two-dimensional problems in terms of speed. The advantage comes in high order

two-dimensional problems and three-dimensional problems where the BEM shows a time advantage of from four to ten to one over the finite element method (6). This is because the BEM always has a fully populated stiffness matrix where the FEM has a sparsely populated stiffness matrix usually distributed along the diagonal of the matrix. However, the size of the stiffness matrix increases more rapidly for the finite element method than for the BEM as the order of the problem increases, exactly like the increase in area verses the increase in perimeter of geometrical problems.

One final advantage of the BEM over FEM is the amount of input required to set up a problem for calculation. The BEM requires only boundary geometric data where as the FEM requires geometric data throughout the domain. So, in general, the BEM requires much less input and thus saves time.

2.3.2 Solution Procedure - Indirect Method. There are two general methods of implementing the BEM, the direct method and the indirect method. The differences between these two methods are subtle and a discussion of them is beyond the scope of this paper. The method used in this development is the indirect formulation of the BEM.

Once the boundary value problem has been completely stated, the solution procedure proceeds in three basic steps as set out in Reference 16.

1. Establish the infinite-domain unit singular solution appropriate to the boundary value problem.

2. Form and solve the auxiliary boundary value problem in the infinite domain by employing superposition of the established solutions.
3. Use the solution of the auxiliary boundary value problem to obtain the solution to the original boundary value problem.

The unit singular solution is a known solution to the governing differential equation of the boundary value problem. The unit singular solution is very much like an influence function which gives the response, say displacement, at some field point due to a prescribed unit force at some other point, called the source point or load point. Green's functions are often the unit singular solutions that are used in this step. The unit singular sclutions must be known in order for the procedure to be used.

The second step in the solution process calls for the formulation of the auxiliary problem and then use of the unit infinite solution to solve this problem. This is accomplished by the superposition of the applicable unit singular solutions. The word superposition implies that the method is limited to linear elastic material behavior. The boundary value problem is buried within an infinite domain and the forces, displacements, etc., that define the true boundary value problem are determined in terms of the unit infinite solutions.

The final step in the solution procedure is to use the

solution of the auxiliary boundary problem to solve the original boundary value problem. The exact means of solving the original boundary value problem from the solution of the auxiliary boundary value problem is best understood by working through an example.

2.3.3 Built-In Beam Problem Symmetric Case.

2.3.3.1 Formulation Of The Boundary Value Problem. The formal statement of the boundary value problem associated with the built-in beam problem is considered in Figure 2-15. It is essentially the fourth order beam equation and the associated boundary conditions as follows:

$$EI \frac{d^4y}{dx^4} = 0 \qquad (2\text{-}25)$$

where

at x = 0, $y = 0$ and $\theta = 0$
at x = $L$, $y = 0$ and $s = -P$

where $y$ is the displacement and $\theta$ is the rotation of the beam and $s$ is the shear. In addition $m$ will be defined as the moment.

2.3.3.2 Unit Singular Solutions. The unit singular solutions for the boundary value problem at hand are given in Reference 6. The unit singular solutions for displacement, rotation, moment and shear due to a

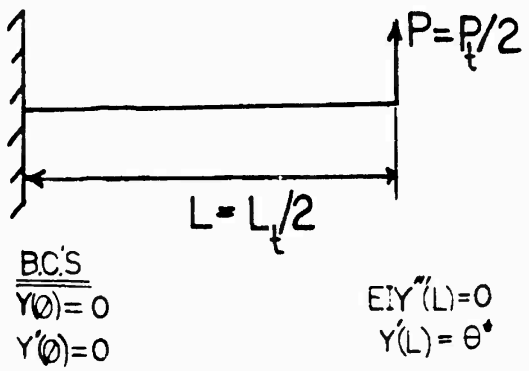


FIGURE 2-15 BUILT-IN BEAM SYMMETRIC CASE

concentrated load $\phi_1$ are:

$$y(x) = \phi_1\left[\lambda L^3(2 + |\rho|^3 + 3|\rho|^2)\right] = \phi_1(\xi)\ G(x,\xi) \qquad (2\text{-}26a)$$

$$\theta(x) = \frac{dy}{dx} = \phi_1\left[3\lambda L^2|\rho|(|\rho|-2)(\text{sgn }\rho)\right] = \phi_1(\xi)\ F(x,\xi) \qquad (2\text{-}26b)$$

$$m(x) = EI\ \frac{d^2y}{dx^2} = \phi_1\left[-\frac{L}{2}(1 - |\rho|)\right] = \phi_1(\xi)\ E(x,\xi) \qquad (2\text{-}26c)$$

$$s(x) = EI\ \frac{d^3y}{dx^3} = \phi_1\left[\frac{(\text{sgn }\rho)}{2}\right] = \phi_1(\xi)\ D(x,\xi) \qquad (2\text{-}26d)$$

where $\lambda = 1/12EI$

$\rho = r/L$

$r = (x - \xi)$ (Fig 2-16)

sgn $\rho$ = +1 if $\rho$ is positive

= -1 if $\rho$ is negative

$x$ is the field point of interest (Fig 2-16)

$\xi$ is the location of the load point (Fig 2-16)

Here the signs of the last two equations have been changed as presented in the reference to be consistent with the sign convention as presented in Figure 2-10. The function sgn($\rho$) is undefined for $\rho = 0$ and this situation must be avoided in the analysis. This will be discussed in more depth in a later section. Before formulating the problem in the infinite domain we still need the unit infinite solutions for a concentrated moment as the solutions are not the same as those for a concentrated force. Again from reference 6 we have for the concentrated moment $\phi_2$:

$$y(x) = \phi_2 \left\{-\left[\lambda L^2 |\rho| (|\rho|^2 - 3|\rho| + 2)(\text{sgn } \rho)\right]\right\} \qquad (2\text{-}27a)$$

$$= \phi_2(\xi)\ K(x,\xi)$$

$$\theta(x) = \phi_2 \left\{-\left[\lambda L (3|\rho|^2 - 6|\rho| + 2)\right]\right\} = \phi_2(\xi)\ \mathcal{L}(x,\xi) \qquad (2\text{-}27b)$$

$$m(x) = \phi_2 \left[(1 - |\rho|)\frac{(\text{sgn } \rho)}{2}\right] = \phi_2(\xi)\ M(x,\xi) \qquad (2\text{-}27c)$$

$$s(x) = \phi_2 \left[-(1/2L)\right] = \phi_2(\xi)\ N(x,\xi) \qquad (2\text{-}27d)$$

where the same parameters as defined in equations 2-26 apply. Again the sign of the last two equations have been changed to be consistent with the chosen sign convention. Equations 2-26 and 2-27 are the complete set of solutions for the posed boundary value problem. All of these equations will not be required to solve the problem at hand.

2.3.3.3 Defining The Auxiliary Problem. The next step in the solution procedure is to define the auxiliary problem. To accomplish this we embed the original problem in an infinite domain. Figure 2-16 shows the embedded beam. In Figure 2-16 the $\phi_1(0), \phi_2(0), \phi_1(L)$ and $\phi_2(L)$ are the applied forces and moments which force the auxiliary problem to maintain the same boundary conditions as the original problem. These are at present unknown. The $\psi(\xi)$ is the load at point $\xi$ which for our problem is $P(L)$.
Keeping in mind Figure 2-16 the auxiliary problem is now

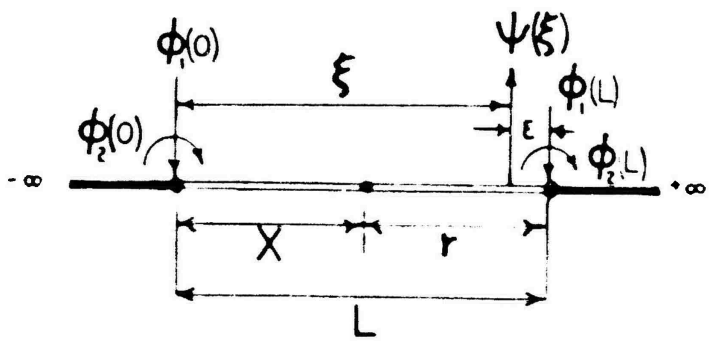


FIGURE 2-16 AUXILIARY PROBLEM FOR SYMMETRIC BEAM

stated as:

> Find the concentrated forces and moments applied at the points 0 and $L$ that, together with the load point at $\xi$, satisfy the boundary conditions of the original problem.

In general, the solution for the deflection, rotation, moment, and shear at any field point $x$ (double line in Figure 2-16) can be written as the superposition of the contributions of all concentrated forces and moments acting in the domain. Thus we have:

$$y(x) = \phi_1(0)G(x,0) + \phi_2(0)K(x,0) + \phi_1(L)G(x,L) + \phi_2(L)K(x,L) + \psi_1(\xi)G(x,\xi) + \psi_2(\xi)K(x,\xi) + C_1 + \{C_2 \cdot x\} \quad (2\text{-}28a)$$

$$\theta(x) = \phi_1(0)F(x,0) + \phi_2(0)\mathcal{K}(x,0) + \phi_1(L)F(x,L) + \phi_2(L)\mathcal{K}(x,L) + \psi_1(\xi)F(x,\xi) + \psi_2(\ )\rightarrow(x,\xi) + C_2 \quad (2\text{-}28b)$$

$$m(x) = \phi_1(0)E(x,0) + \phi_2(0)M(x,0) + \phi_1(L)E(x,L) + \phi_2(L)M(x,L) + \psi_1(\xi)E(x,\xi) + \psi_2(\xi)M(x,\xi) \quad (2\text{-}28c)$$

$$s(x) = \phi_1(0)D(x,0) + \phi_2(0)N(x,0) + \phi_1(L)D(x,L) + \phi_2(L)N(x,L) + \psi_1(\xi)D(x,\xi) + \psi_2(\xi)N(x,\xi) \quad (2\text{-}28d)$$

where

- $D, E, F, G, K, \mathcal{K}, M$, and $N$ are defined in equations 2-26 and 2-27
- $\phi_1$ and $\phi_2$ are the concentrated forces and moments applied at the end points of the embedded beam
- $\psi_1$ and $\psi_2$ are the concentrated forces and moments applied to the original beam

- $C_1$ is a rigid body displacement
- $C_2$ is a rigid body rotation

For the case of the symmetric beam loaded by the force $P$ we have only a $\psi_1$ term that shows up in the equations and the value of $\xi$ is $L$. There is no $\psi_2$ because the original problem did not have a concentrated moment applied.

The constant values $C_1$ and $C_2$ require some additional explanation. Because we could choose to embed the original problem in an infinite solution at any arbitrary value of y and at any arbitrary angle to the x axis, a summation of forces and moments on the auxiliary problem, in general, does not satisfy equilibrium. Mathematically stated:

Summation of Forces $\sum F_Y \neq 0$ (2-29a)

$\phi_1(0) + \phi_1(L) + \psi_1(L) \neq 0$

in general

Summation of Moments $\sum M_Z \neq 0$

$\phi_2(0) + \phi_2(L) \neq 0$ (2-29b)

in general

By including the values of $C_1$ and $C_2$ in the equations and making them unknown constants which must be solved for, we can enforce the conditions of static equilibrium. This is more clearly understood if the equations 2-28 are stated in matrix form. Following the development in Reference 6 we get:

$$\begin{Bmatrix} y(x) \\ \theta(x) \\ m(x) \\ s(x) \\ 0 \\ 0 \end{Bmatrix} = \begin{bmatrix} G(x,0) & K(x,0) & G(x,L) & K(x,L) & 1 & x \\ F(x,0) & \mathcal{L}(x,0) & F(x,L) & \mathcal{L}(x,L) & 0 & 1 \\ E(x,0) & M(x,0) & E(x,L) & M(x,L) & 0 & 0 \\ D(x,0) & N(x,0) & D(x,L) & N(x,L) & 0 & 0 \\ 1 & 0 & 1 & 0 & 0 & 0 \\ 0 & 1 & 0 & 1 & 0 & 0 \end{bmatrix} \begin{Bmatrix} \phi_1(0) \\ \phi_2(0) \\ \phi_1(L) \\ \phi_2(L) \\ C_1 \\ C_2 \end{Bmatrix} +$$

$$\begin{bmatrix} G(x,L) \\ F(x,L) \\ E(x,L) \\ D(x,L) \\ 1 \\ 0 \end{bmatrix} \quad \{\psi_1(L)\} \qquad (2\text{-}30)$$

Notice the last two rows in equation 2-30. Row five ensures that $C_1$ is chosen such that the summation of forces is satisfied thus equation 2-29a is false. Row six ensures that $C_2$ is chosen such that the summation of moments is zero and thus equation 2-29b is false.

Equation 2-30 presents a clear method with which one may solve the auxiliary problem. From equation 2-30 and from Figure 2-15 we have the boundary conditions of the original problem. By using a form of equation 2-30 with the correct equations for the given boundary conditions we can solve for the unknown $\phi_1$'s and $\phi_2$'s and determine the necessary constants $C_1$and $C_2$to ensure equilibrium. The properly formulated equation is:

$$\underset{\{bc\}}{\begin{Bmatrix} y(0)=0 \\ \theta(0)=0 \\ \theta(L)=0 \\ s(L)=0 \\ 0 \\ 0 \end{Bmatrix}} = \underset{[K]}{\begin{bmatrix} G(0+\varepsilon,0) & K(0+\varepsilon,0) & G(0+\varepsilon,L) & K(0+\varepsilon,L) & 1 & 0 \\ F(0+\varepsilon,0) & \mathcal{L}(0+\varepsilon,0) & F(0+\varepsilon,L) & \mathcal{L}(0+\varepsilon,L) & 0 & 1 \\ F(L-\varepsilon,0) & \mathcal{L}(L-\varepsilon,0) & F(L-\varepsilon,L) & \mathcal{L}(L-\varepsilon,L) & 0 & 1 \\ D(L-\varepsilon,0) & N(L-\varepsilon,0) & D(L-\varepsilon,L) & N(L-\varepsilon,L) & 0 & 0 \\ 1 & 0 & 1 & 0 & 0 & 0 \\ 0 & 1 & 0 & 1 & 0 & 0 \end{bmatrix}} \underset{\{\Phi\}}{\begin{Bmatrix} \phi_1(0) \\ \phi_2(0) \\ \phi_1(L) \\ \phi_2(L) \\ C_1 \\ C_2 \end{Bmatrix}} +$$

$$\underset{[H]}{\begin{bmatrix} G(0+\varepsilon,L) \\ F(0+\varepsilon,L) \\ F(L-\varepsilon,L) \\ D(L-\varepsilon,L) \\ 1 \\ 0 \end{bmatrix}} \underset{\{\Psi\}}{\begin{Bmatrix} \psi_1(L) \end{Bmatrix}} \qquad (2\text{-}31)$$

Here again some new notation has been introduced. Earlier it was mentioned that if $\rho = 0$ the function $\text{sgn}(\rho)$ is undefined. For this reason a field point and load point may never coincide. If the load point and field point coincide, the load point is adjusted some $\varepsilon$ to the left or right of the field point except at the left or right boundaries. At the left boundary, 0, the field point is taken to the boundary element at 0 from some $\varepsilon$ just to the right of the boundary element. At the right boundary, $L$, the field point is taken to the boundary element at $L$ from some $\varepsilon$ just to the left of the boundary element. Thus, the terms $(0+\varepsilon)$ and $(L-\varepsilon)$ appear in the kernel functions. It is important to take the field point to the boundary elements from inside the domain or the wrong problem is modeled.

The solution of the auxiliary problem is now reduced to the solution of the equation 2-31. Using the notation found in equation 2-31 we have:

$$\{\Phi\}=[K]^{-1}(\{bc\}-[H]\{\Psi\}) \qquad (2\text{-}32)$$

2.3.3.4 Solution to Original Problem. The solution of the auxiliary problem by use of equation 2-32 gives a column vector of forces and moments as well as a rigid body displacement and rotation. The $\Phi$ vector can be placed directly into equation 2-30 and, recalling that 0 is replaced by $\varepsilon$, and $L$ is replaced by $L-\varepsilon$, the solution for the displacement, rotation, moment and shear at any location $x$ in the beam can be found. A flow diagram of the entire process with the appropriate equations referenced appears in Figure 2-17.

A Fortran computer program which follows the flow diagram of Figure 2-17 was developed as part of this thesis effort. It takes as input the material properties of the beam, the variable $\varepsilon$, two boundary conditions at each end of the beam and the associated values of those boundary conditions. The code also looks for applied loads and the location at which they are applied. The code outputs the material properties, the boundary conditions, and the displacement, rotation, moment, and shear at up to 500 locations throughout the beam. In addition the code writes shear and moment files which can be plotted to see the shear and moment diagrams for a particular loading case.

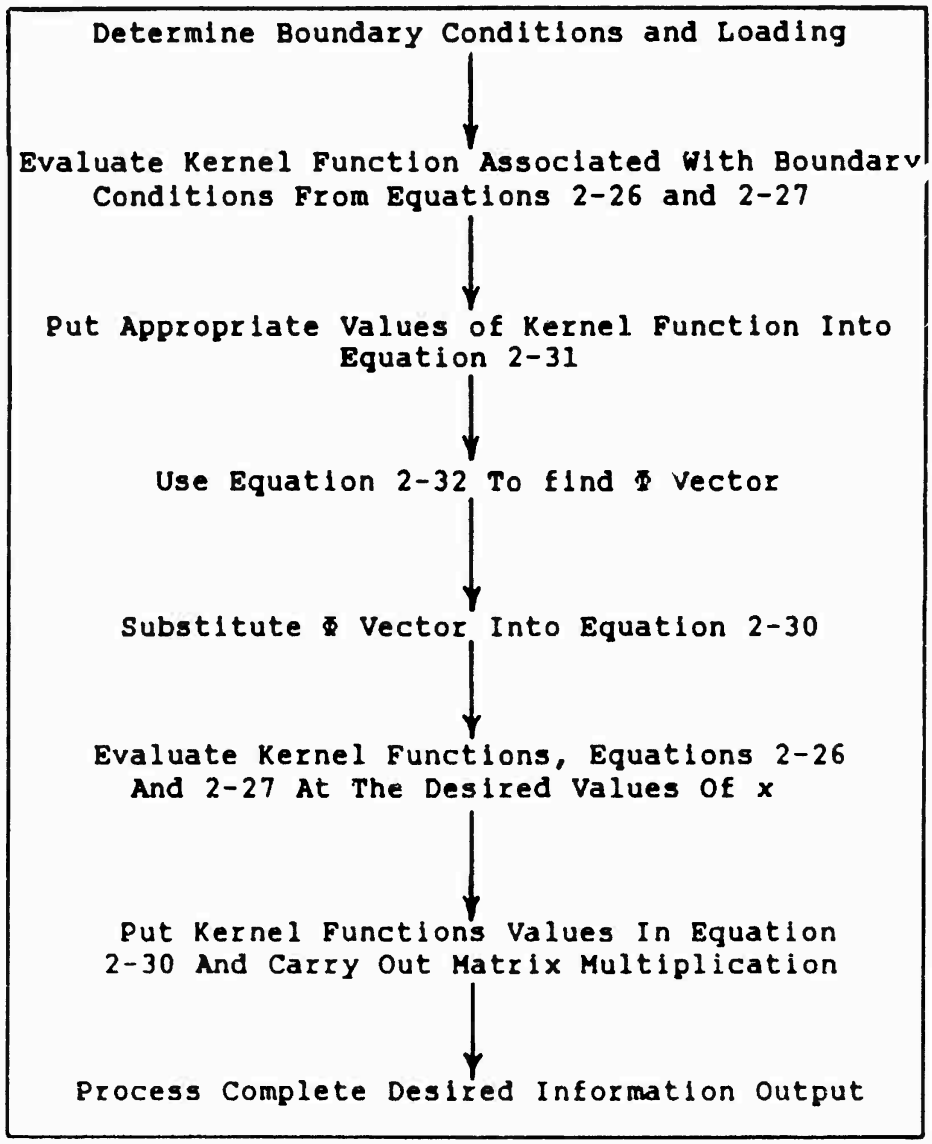


FIGURE 2-17 FLOW DIAGRAM FOR INDIRECT BEM

The Appendix contains several computer runs using the one-dimensional BEM. Included are the built-in beam problem, the built-in beam symmetric case, and a cantilever beam problem. Both displacement controlled and force controlled runs are presented. In addition, to demonstrate the general

versatility of the code, a built-in beam with a distributed load applied across the span is shown for both the full length and the symmetric case problems. Also shown are the shear and moment diagrams for the loading cases studied.

As a side note, an extensive literature search was accomplished and the only similar code found was in Reference 16 where Shugar and Cox develop a code in basic which calculates the displacement, rotation, moment, and shear for beams on elastic foundations. The nature of the free space Green's functions for such a problem are such that the constants $C_1$ and $C_2$ need not be determined (6). The solutions are already uniquely determined inherent to the kernel functions.

Reference 6 gives a general account of the solution of the problem when the calculation of $C_1$ and $C_2$ is necessary, however several errors were found in this reference which required further development before the code functioned correctly. With a reliable method of determining the beam response for a given input at the boundary conditions and an applied load acting on the beam, we move on to the development of the friction model.

# III. The Friction Models

## 3.1 Joint Geometry And General Assumptions.

The built-in beam geometry has already been discussed in the theory section. The present study assumes the same geometry with one major change. The built-in beam geometry consists of two cantilever beams extending from opposite directions to a common joint where Coulomb friction is assumed. Figure 3-1 shows a scale drawing of the physical dimensions of the two-beam arrangement. A uniform clamping pressure $P^*$ holds the beams together at the joint.

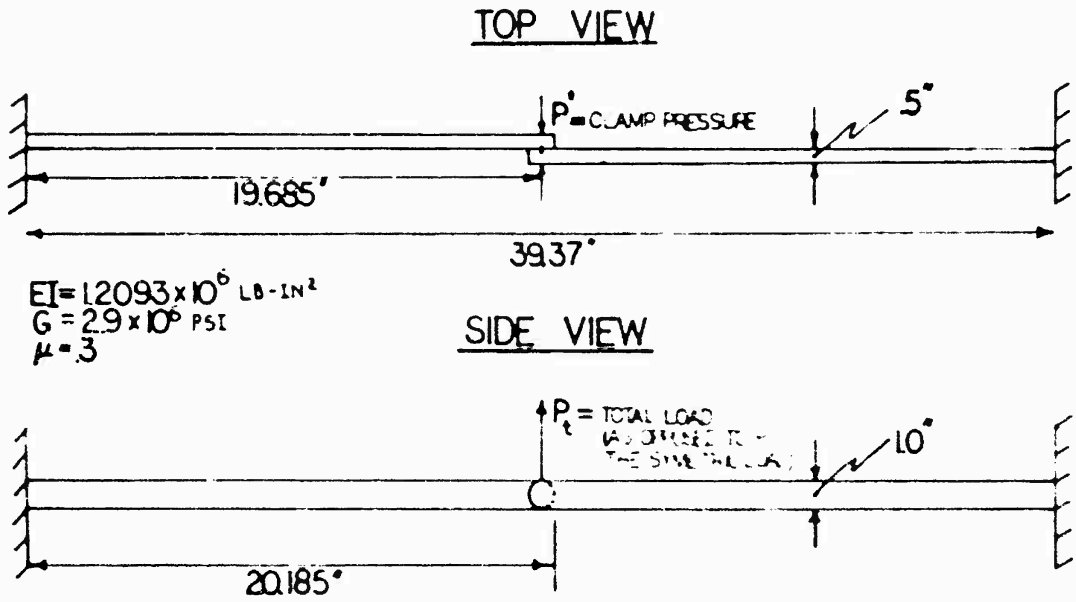


FIGURE 3-1 DAMPING MODEL GEOMETRY, MATERIAL AND LOADING

The beams are each of equal dimension and are both made of structural steel with the material properties as shown in Figure 3-1. Under all loading conditions considered herein the individual beams observe linear elastic material behavior.

Figure 3-2 shows an enlarged view of the joint and shows that a circular contact area is assumed at the joint. The joint has a radius of .5 in. The contact area is assumed homogeneous i.e., a hole where a rivet or bolt is connecting the beams is not considered.

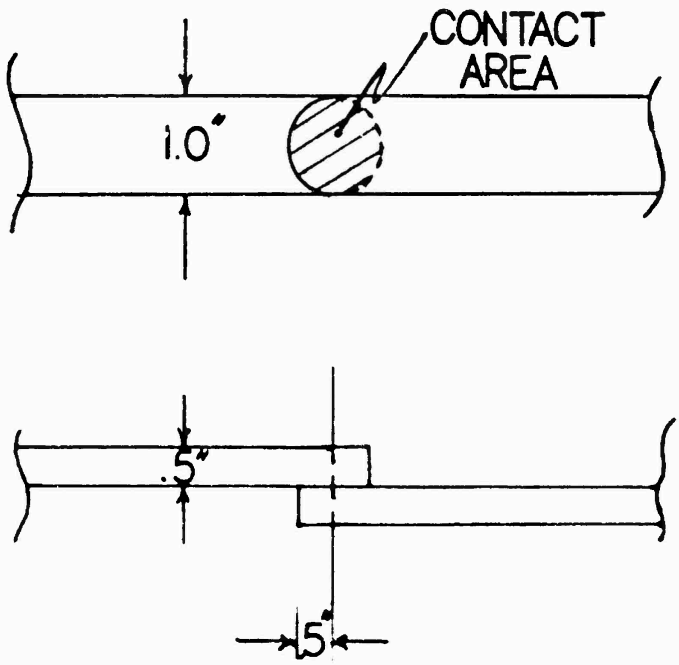


FIGURE 3-2 ENLARGEMENT OF BEAM JOINT

The load $P_t$ is applied at the joint so that no twisting of the beams occurs. The beam joint system undergoes deformation in an x-y plane that can be thought of as an extension of the contact area of the joint. Figure 3-3 shows this x-y plane containing the contact area. All

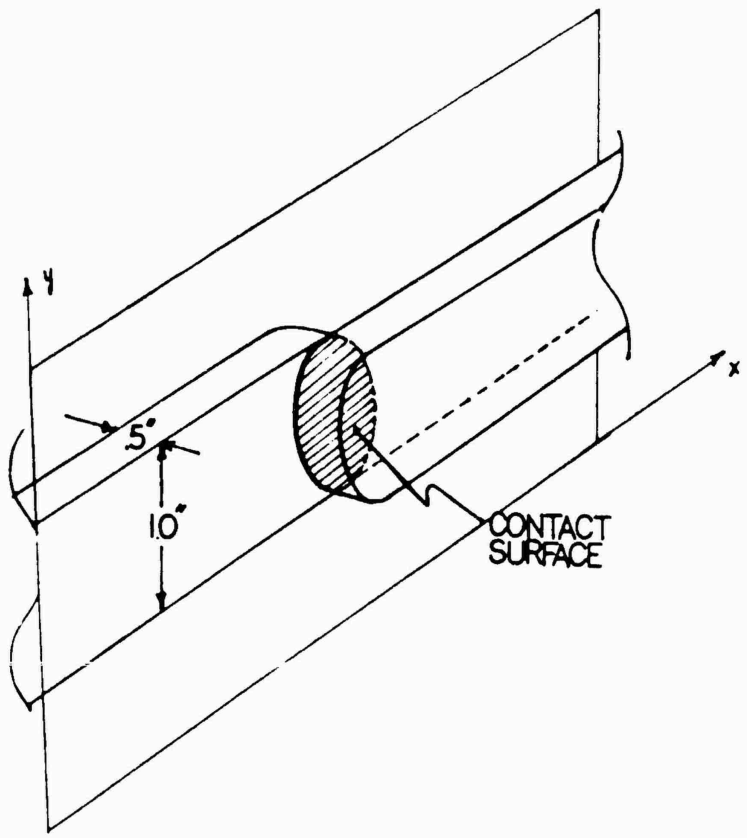


FIGURE 3-3 X-Y PLANE CONTAINING CONTACT AREA OF JOINT

forces generated are symmetric about this plane and the beams sides remain parallel to this plane. With the joint geometry defined and the general assumptions laid out, we can proceed with the discussion of the friction models.

3.2 Gross Slip Model.

As discussed in Chapter 2 the first step in the analysis of the friction damping in a joint is to assume that the joint dissipates no energy until the moment in the joint reaches a value that causes the entire contact area of the joint to slip. The value of the moment at which this gross slip of the joint occurs is designated $M_{gs}$ and is given in equation 2-16. It follows that $M_{gs}$ is also the maximum moment the joint can support.

The beam geometry used in the analysis of the joint under consideration consists of the symmetric beam case. Figure 3-4 shows the original geometry and the boundary conditions assumed for the various ranges of the moment value in the joint. The load $P$ is assumed to be applied as a sinusoidal time varying load which varies in 1 and 1/4 cycles from 0 to the maximum value of load $P_{max}$ to a minimum value $-P_{max}$ and back to $P_{max}$ again. The analysis is quasi-dynamic, and the inertia effects of the beam are not considered. The loading cycle is broken into three distinct regions of interest; the initial loading, the unloading, and the reloading, in the same way the Richardson and Nolle model was studied.

3.2.1 Initial Loading. In the initial loading phase the applied load changes between 0 and the maximum load $P_{max}$. The joint does not rotate until the moment in the joint exceeds the moment developed by the maximum allowable frictional shear stress acting over the contact surface of

the joint. This value of moment is given by equation 2-16 and is repeated here:

$$M_{gs} = \frac{2}{3} \pi \mu P^* R^3 \qquad (3\text{-}1)$$

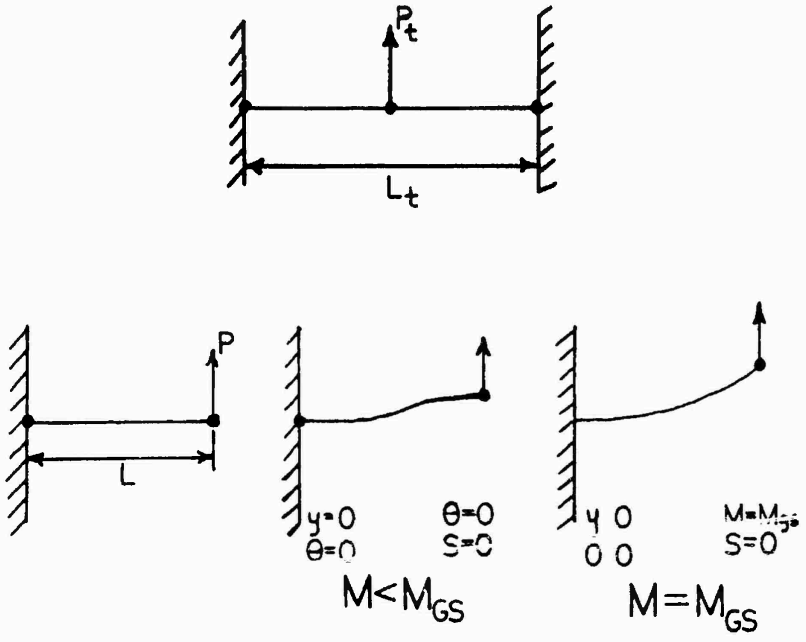


FIGURE 3-4 ORIGINAL GEOMETRY AND BOUNDARY CONDITIONS FOR THE GROSS SLIP MODEL OF FRICTION

Until this value of moment is reached the boundary conditions are given as:

$$\left.\begin{matrix} y = 0 \\ \theta = 0 \end{matrix}\right\} \quad \text{at } x = 0$$
$$\left.\begin{matrix} \theta = 0 \\ s = 0 \end{matrix}\right\} \quad \text{at } x = L \qquad (3\text{-}2)$$

where the symmetry of the built-in beam about the joint

allows the $s(L)=0$ boundary condition. It should be mentioned here that the boundary conditions at $x = 0$ remain the same for the entire analysis.

Figure 3-5 shows that as the load increases towards $P_{max}$ a moment, $M_{ext}$, builds up in the joint acting in a negative direction. At the point where the moment in the beam equals the moment caused by the frictional shear stress, $-\frac{2}{3}\pi\mu P^{*}R^{3}$ (where the minus sign signifies clockwise direction), the limit moment, $-M_{gs}$ in the joint is reached. Thus we have:

$$M_{ext} = -M_{gs} \qquad (3\text{-}3)$$

$$M_{ext} = -\frac{2}{3}\pi\mu P^{*}R^{3}$$

The value of load $P$ which causes the moment in the joint to reach $-M_{gs}$ is designated $P_{gs}$. If $P_{max} \leq P_{gs}$ the M-$\theta$ diagram is a vertical line which encloses no area and thus the jointed beam behaves as the continuous beams investigated in the Appendix. The case of interest is where $P_{max} > P_{gs}$.

When $P_{max} > P_{gs}$ the initial loading curve continues. The boundary conditions change to reflect the condition that the limit value of moment due to frictional shear stress has been reached. This condition relates directly, through equation 3-3, to a limit on the magnitude of moment the joint can support and the boundary conditions at $x = L$ change to:

$$\left.\begin{aligned} m &= -M_{gs} \\ s &= 0 \end{aligned}\right\} \quad \text{at } x = L \qquad (3\text{-}4)$$

The joint is allowed to rotate until the loading force $P$

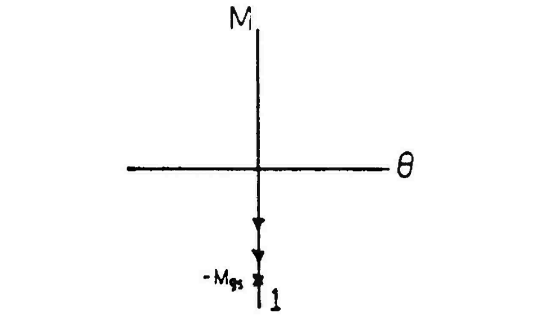


M-θ CURVE

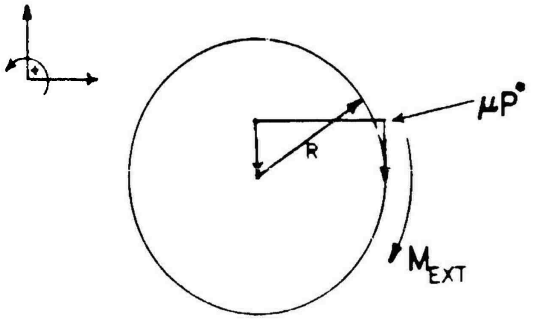


FRICTION MODEL

FIGURE 3-5 GROSS SLIP MODEL INITIAL LOADING ($0 < P \leq P_{gs}$)

reaches $P_{max}$. The rotation at $P_{max}$ is designated $\theta_{max}$. Figure 3-6 shows the M-$\theta$ diagram and the friction model.

3.2.2 Unloading. The next interval of the loading cycle to be considered is the unloading phase where the load P varies between $P_{max}$ and $-P_{max}$. Once the load has reached

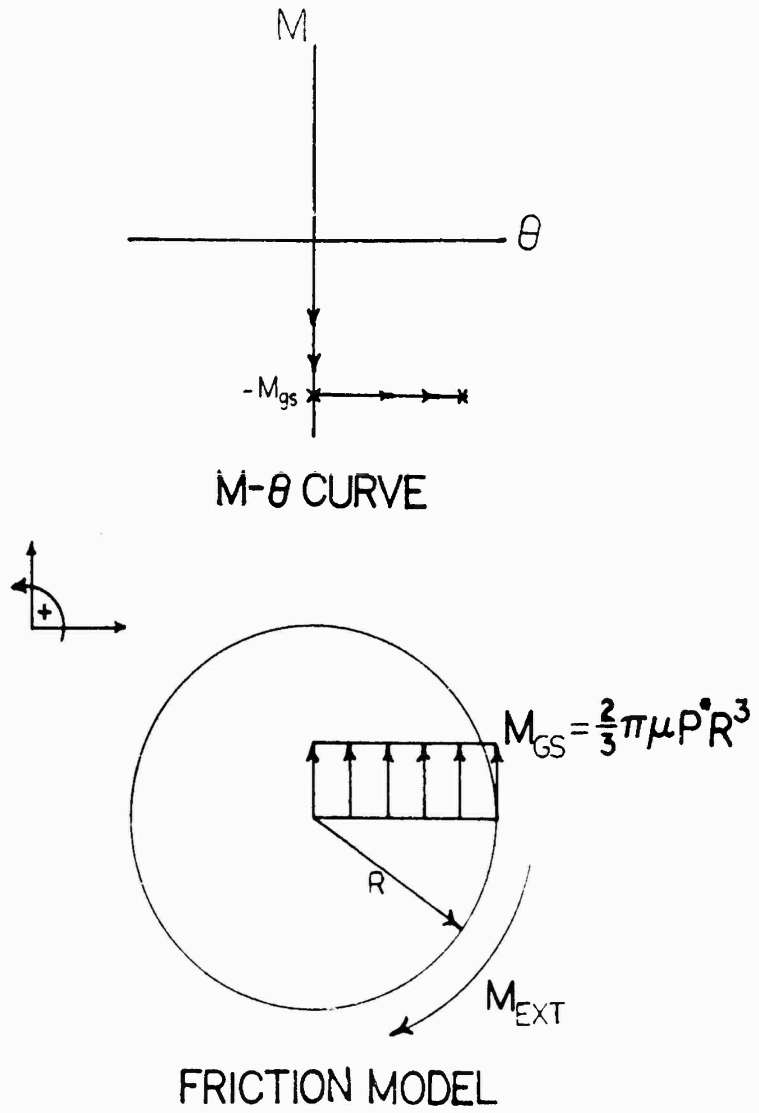


FIGURE 3-6 GROSS SLIP INITIAL LOADING ( $P_{gs} < P \leq P_{max}$ )

its maximum value of $P_{max}$ in the initial load phase the boundary conditions change again. The rotation at the joint is fixed at the maximum rotation $\theta_{max}$. Fixing the rotation at $\theta_{max}$ locks in the frictional shear stress built up in the initial loading phase of the cycle, $-\mu P^*$, which causes a

residual moment $M_{res} = -M_{gs}$ in the joint. The boundary conditions at $x = L$ are:

$$\left.\begin{matrix}\theta=\theta_{max} \\ s=0\end{matrix}\right\} \quad \text{at } x = L \tag{3-5}$$

As the applied load now changes from $P_{max}$ toward $-P_{max}$, the moment in the joint, $M_{ext}$, builds up in the positive direction. $M_{ext}$ will continue to build up in the joint until moment caused by the frictional shear stress reaches the limit value of $+\frac{2}{3} \pi \mu P^{*}R^{3}$ and $M_{ext} = +M_{gs}$. For this to occur the residual frictional shear stress of $-\mu P^{*}$ must first be negated, giving the value of allowable frictional shear stress for the unloading phase as $2\mu P^{*}$. The load associated with the point at which the moment caused by the frictional shear stress is exceeded in the unloading phase is designated $P_{ugs}$. Figure 3-7 shows the loading, M-$\theta$ diagram and friction model for this region of the unloading phase.

The boundary conditions once again change when the frictional shear stress moment is exceeded to reflect the limited moment carrying capability of the joint, $M_{gs}$, and thus become:

$$\left.\begin{matrix}m = M_{gs} \\ s = 0\end{matrix}\right\} \quad \text{at } x = L \tag{3-6}$$

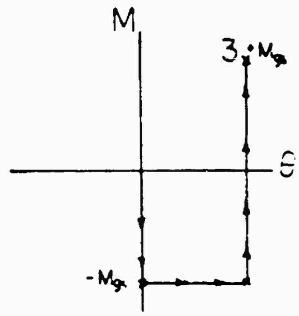


M-θ CURVE

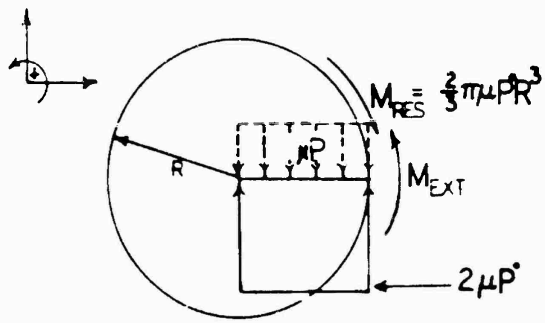


FRICTION MODEL

## 3-7 GROSS SLIP UNLOADING ($P_{max} > P \geq P_{ugs}$)

The load continues to increase in amplitude from $P_{ugs}$ to $-P_{max}$ and as it does so the joint rotates from $\theta_{max}$ to $\theta_{min}$. Figure 3-8 shows this region of the unloading curve.

When the load reaches $-P_{max}$ the load cycle changes direction again. The value of $\theta_{min}$ is locked in the joint and replaces the moment boundary condition at the right end. Formally stated the boundary conditions are:

$$\left.\begin{aligned} \theta &= \theta_{min} \\ s &= 0 \end{aligned}\right\} \quad \text{at } x = L \qquad (3\text{-}7)$$

Setting the $\theta = \theta_{min}$ boundary condition locks in residual frictional shear stress and thus creates a residual moment, $M_{res}$, in

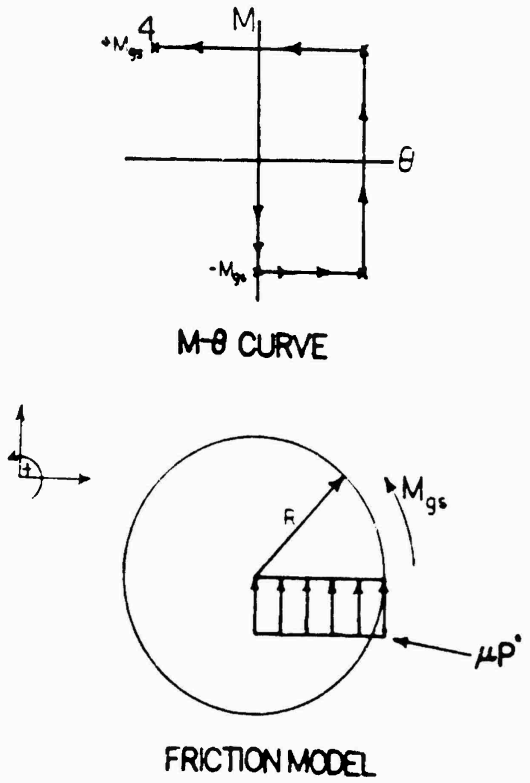


FIGURE 3-8 GROSS SLIP UNLOADING ($-P_{max} \leq P < P_{ugs}$)

the joint. The joint is now ready to begin the reloading phase of the load cycle.

3.2.3 Reloading. In this phase of the loading cycle the applied load changes from $-P_{max}$ to $P_{max}$, completing the entire 1 and 1/4 cycles. As the load changes from $-P_{max}$ the frictional shear stress moment again builds up until the limit value $-M_{gs}$ is acting at the joint. Figure 3-9 shows the allowable frictional shear stress in the reloading phase is $-2\mu P^*$. The load associated with the limit value of frictional shear stress during reload is designated $P_{rgs} = -P_{ugs}$.

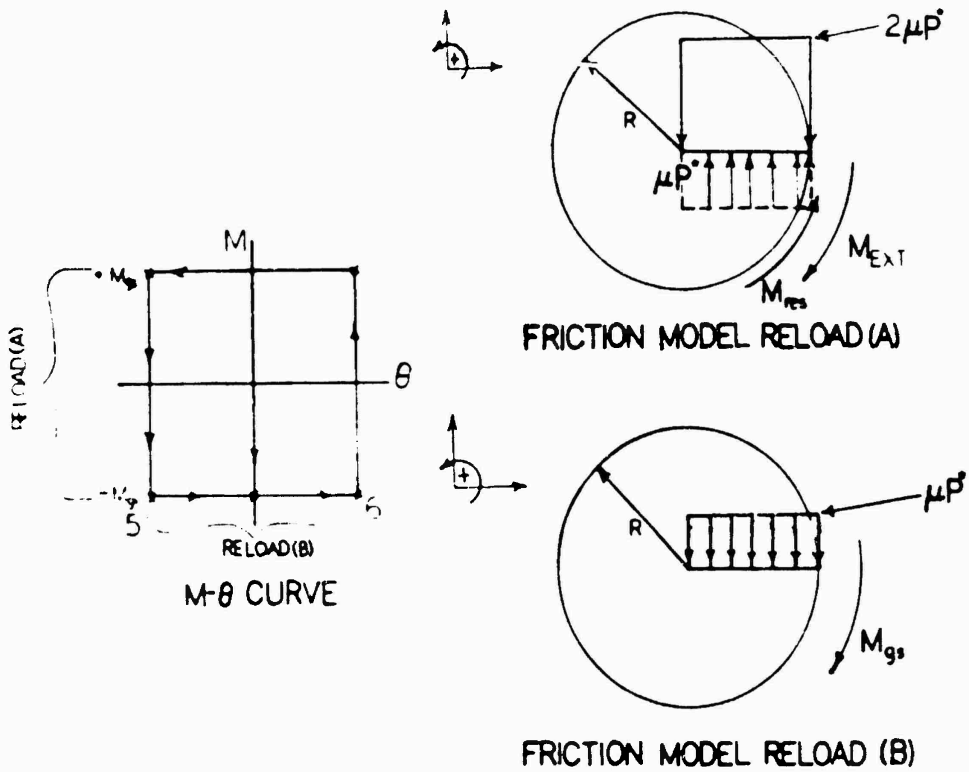


FIGURE 3-9 GROSS SLIP RELOADING ($-P_{max} > P \geq P_{max}$)

Following the same physics of the unload curve, the boundary conditions now change to reflect the fact that the limit moment is again acting in the joint. The boundary conditions are given in equation 3-4. The load continues to change from $P_{rgs}$ to $P_{max}$ and the rotation at the joint goes from $\theta_{min}$ to $\theta_{max}$ completing the hysteresis loop and the load cycle. The entire loop is governed by one equation

(3-1) and several different boundary conditions (equations 3-2,and 3-4 through 3-7). The gross slip model is thus easily implemented in a computer code.

3.2.4 Computer Implementation Of Gross Slip Model. The computer implementation of the gross slip model proved quite simple given the capability of the boundary element method to use any of the four boundary conditions possible at either end of the beam. It requires at the most the calculation of six points and in some cases (the no-slip and no-clamp cases) only three points are calculated.
The first step in the computer implementation of the gross slip model is to calculate, using equation 3-1, the value of $M_{gs}$. If the value of $M_{gs}$ is zero or negligible with respect to the maximum applied load the no-clamp case is assumed and the program branches to a routine that calculates the M-$\theta$ diagram and $P$-$\delta$ diagram for this case.

Next, a combination of equations 3-2 and 3-4 are used to set the boundary conditions prior to running the BEM. In Figure 3-5 the point (1) is located at a point where the boundary conditions are equation 3-2 and equation 3-4. This collocation of boundary conditions along with equation 2-24a is used instead of incrementing the load in time. The procedure is to set the boundary conditions for the initial BEM run to the following:

$$
\begin{aligned}
y(0) &= 0 \\
\theta(0) &= 0 \\
\theta(L) &= 0 \\
m(L) &= -M_{gs}
\end{aligned}
\qquad (3\text{-}8)
$$

The value of applied load is set to zero and the BEM is run. As a result, the displacement, rotation, moment, and shear at any point in the beam is available. Now equation 2-24a is used indirectly. It states that the value of the shear at any point in the beam is equal in magnitude and opposite in direction to the applied load. Using this information the shear at $x = 0$ is used to determine the applied load as follows:

$$
\begin{aligned}
EIy'''(0) &= -P \\
s(0) &= -P \\
P &= -s(0)
\end{aligned}
\qquad (3\text{-}9)
$$

This simple procedure determines directly the point $P_{gs}$ without incrementing through time. If $P_{gs} \geq P_{max}$ the no-slip condition exists and the code branches to a routine to calculate the M-$\theta$ and P-$\delta$ diagrams and the routine stops. When $P_{gs} < P_{max}$ the $m, s, \theta$ and $\delta$ information for point (1) is stored and the routine continues.

The next point calculated is point (2) in Figure 3-6. The boundary conditions of equation 3-4 are set in the BEM and the applied load is set to $P_{max}$. The BEM again gives $\delta$, $\theta$, $m$ and $s$ at any point in the beam. Here the value of $\theta(L)$

equals $\theta_{max}$ and of course $m(L)$ equals $-M_{gs}$ from the boundary conditions.

The calculation of point (3) in Figure 3-7 follows a similar procedure to the one used to calculate point (1). The applied load is set to zero and a combination of equations 3-5 and 3-6 are used in the boundary conditions such that:

$$\theta(L) = \theta_{max}$$
$$m(L) = +M_{gs} \qquad (3\text{-}10)$$

The result of the BEM are used in combination with equation 3-9 to find the load $P_{ugs}$ .

The calculation of point (4) in Figure 3-8 follows closely the development for the calculation of point (2) and will not be presented in detail here. Figure 3-10 is a flow diagram for the entire cycle of loading. The details of the no-clamp case and no-slip case are also not discussed as these problems are presented in the Appendix as the cantilever beam problem and the built-in beam problem (symmetric case) respectively. The development for the displacement as the time varying input is not discussed here but follows the development for the force varying input very closely. Figure 3-11 is the flow diagram for a time varying displacement input.

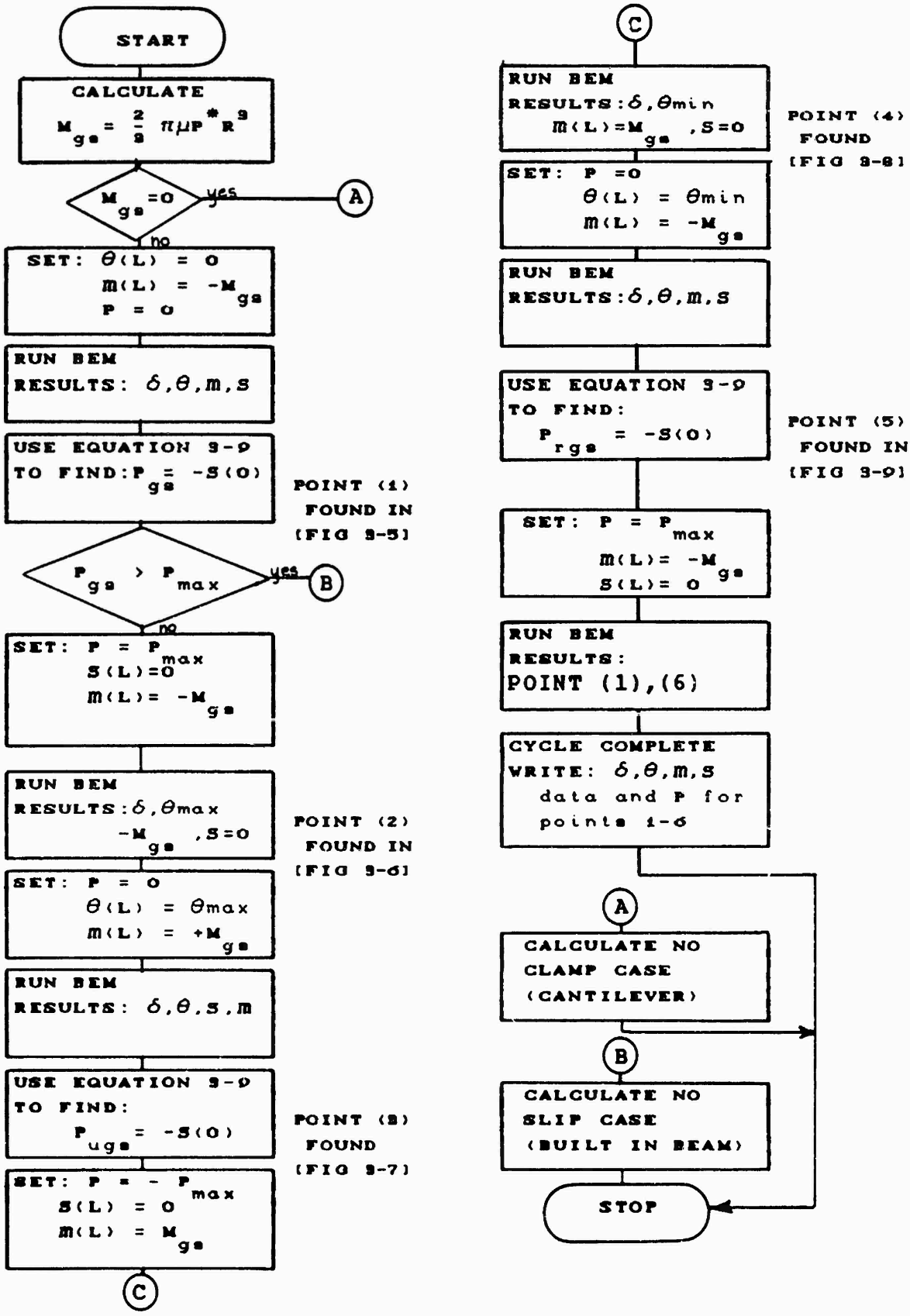


FIGURE 3-10 GROSS SLIP ALGORITHM (FORCE CONTROLLED)

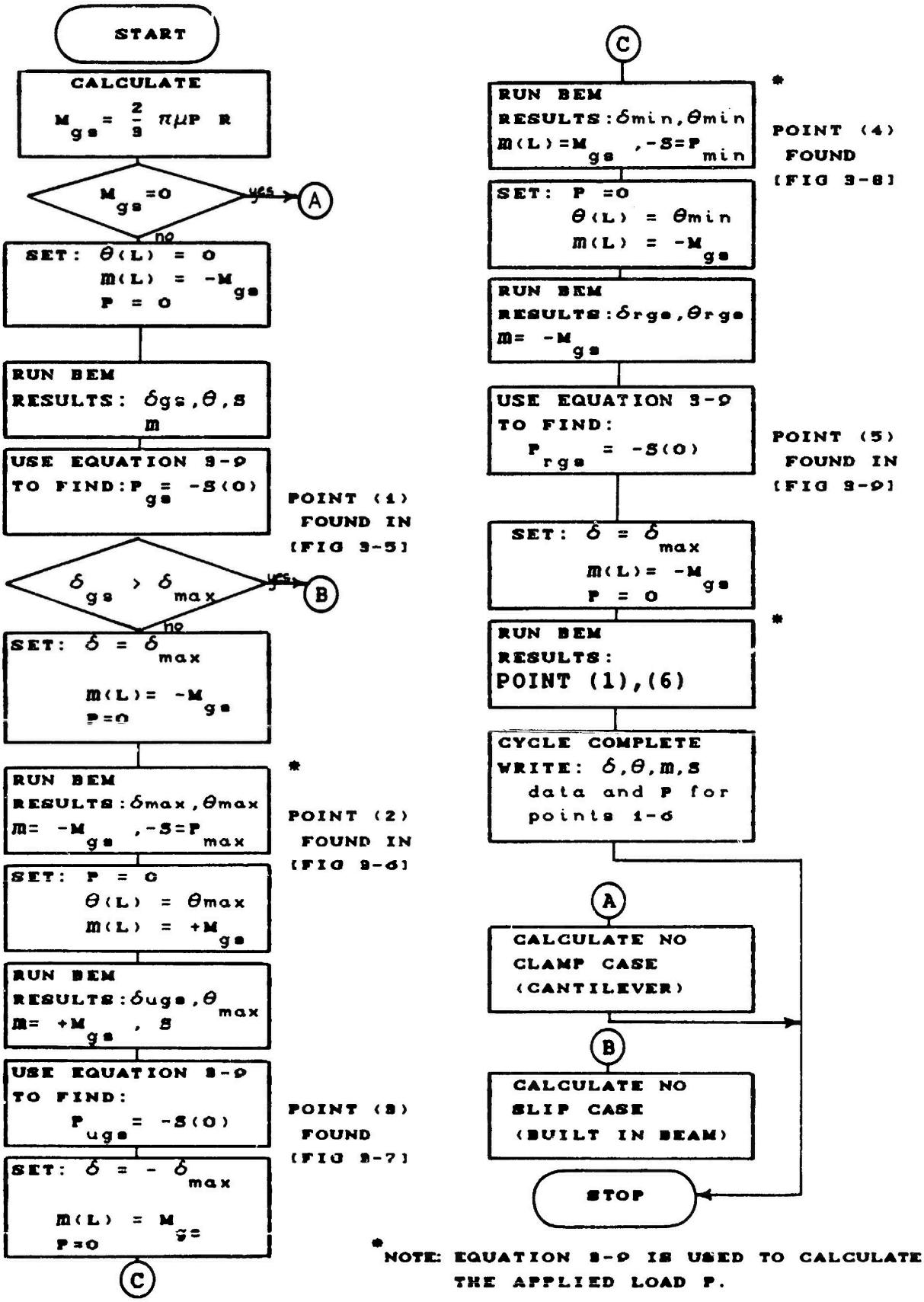


FIGURE 3-11 GROSS SLIP ALGORITHM (DISPLACEMENT CONTROLLED)

As mentioned before the gross slip model is a good starting point in the analysis of the friction in a clamped joint. Now a more accurate model of the joint behavior will be developed, one which allows partial slip of the joint prior to the gross slip condition.

3.3 Micro Slip Model.

The assumptions which governed the behavior of the gross slip model are still applicable in the micro-slip model of friction with one major change. The joint will be allowed to undergo rotation prior to reaching the limit of moment developed by frictional shear stress in the joint.

The model is different from the Richardson and Nolle model in two major ways. The first difference is that where Richardson and Nolle assume the unslipped region of the joint behaves as a rigid body, the model discussed presently assumes the unslipped region behaves as an elastic circular shaft which twists under any finite level of torque. The second difference shows up in the definition of the rotation at the joint. Richardson and Nolle define the rotation as the integration of the displacement due to the shear strains in the slipped region of the joint at the arbitrarily chosen outer radius of the joint. The model presented here defines the rotation in the joint as the angle between the neutral axes of the clamped beams.

Figure 3-12 shows the overall loading and the behavior of the clamped joint for different ranges of moment in the joint. Notice that the rotation at the joint, for values of

moment less than that required for gross slip, is a function of the moment. The development of the functional relationship between the rotation and the moment is the focus of the next section.

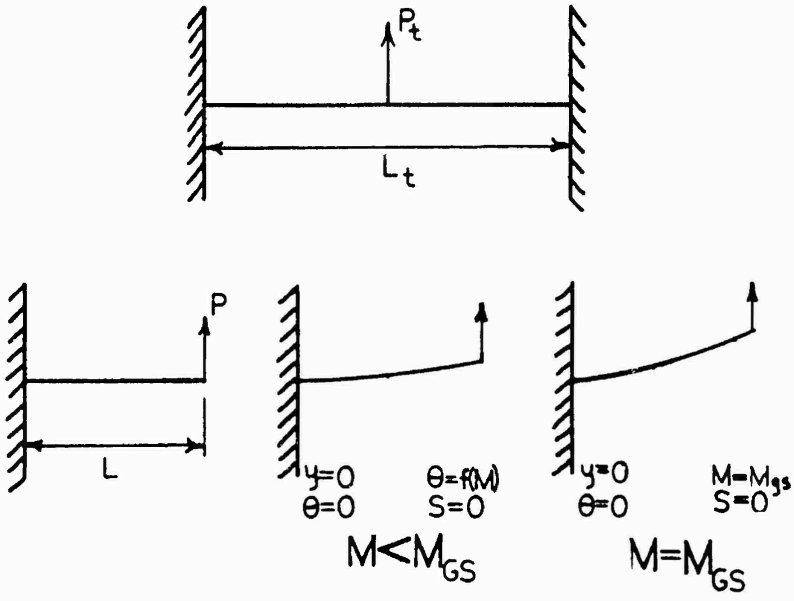


FIGURE 3-12 MICRO-SLIP LOADING AND GENERAL BEHAVIOR

3.3.1 Micro-slip Joint Geometry. The geometry of the micro-slip joint is shown in Figure 3-13. The left and right beams are joined at the Coulomb friction joint. As the joint undergoes deformation a region of slip develops and works its way in from the outer radius $R$ to some radius $a$. The micro-slip model assumes that the region interior to the radius $a$ behaves as a solid elastic circular shaft of radius $a$. Figure 3-14 shows the geometry of this circular shaft of radius $a$. As a first approximation, the length of the circular shaft is assumed to be the width of one of the connected beams as shown in Figure 3-13. This is a major

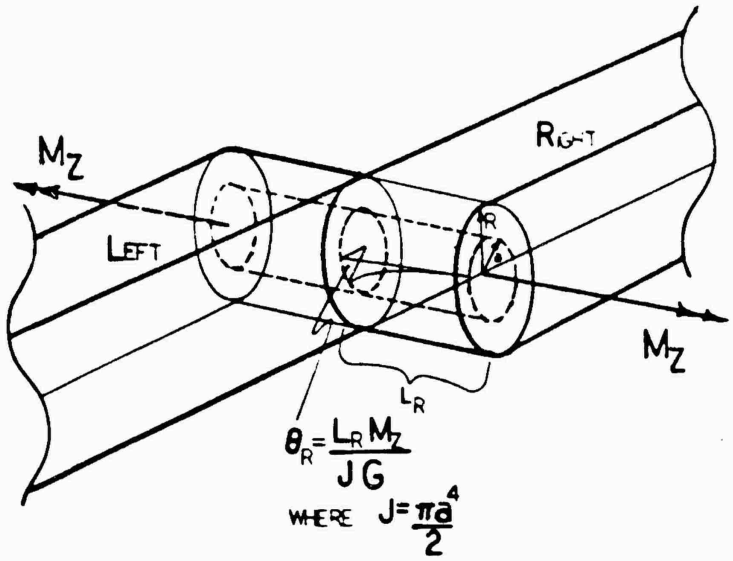


FIGURE 3-13 MICRO-SLIP MODEL OF COULOMB FRICTION JOINT

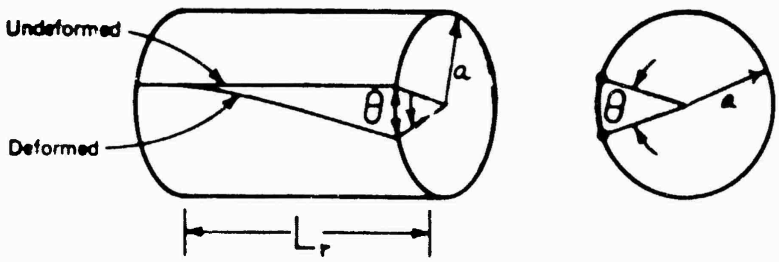


FIGURE 3-14 CIRCULAR SHAFT OF RADIUS $a$

assumption and the model is very sensitive to this length parameter.

Because of our earlier assumption that the beams deform without twist it can be shown from symmetry considerations that the cross-sections of this circular shaft remain planer during deformation (1). Making use of the assumptions of

linear elastic and homogeneous material, Reference 12 uses the theory of elasticity to develop the classical strength of materials equation:

$$\theta = \frac{b\,M}{J\,G} \qquad \text{or} \qquad M = K\,\theta \qquad (3\text{-}11)$$

where

b = the length of the shaft
M = moment applied to shaft
J = polar moment of inertia
G = shear modulus
K = JG/b

The polar moment of inertia for a circular shaft is given in Figure 3-13. The rotation, $\theta$, of the circular shaft and the rotation $\theta(L) = dy/dx$ of the beams connected at the Coulomb friction joint are one and the same. Figure 3-15 is an exploded view of the joint. The figure clearly shows that, because the rotation was not fixed at zero, for any deflection $\delta$ of the beam-joint system a rotation in the circular shaft, and therefore the beam-joint, is produced and is governed by equation 3-11.

Figure 3-15 also shows that the total relative rotation that the joint undergoes is two times the rotation of just one of the beams. It is important to keep this in mind when doing energy loss per cycle calculations since the data generated from a symmetric beam study of the friction problem will only take into account one of the beams and thus only predict half the actual energy loss.

The loading for the micro-slip model, like the gross

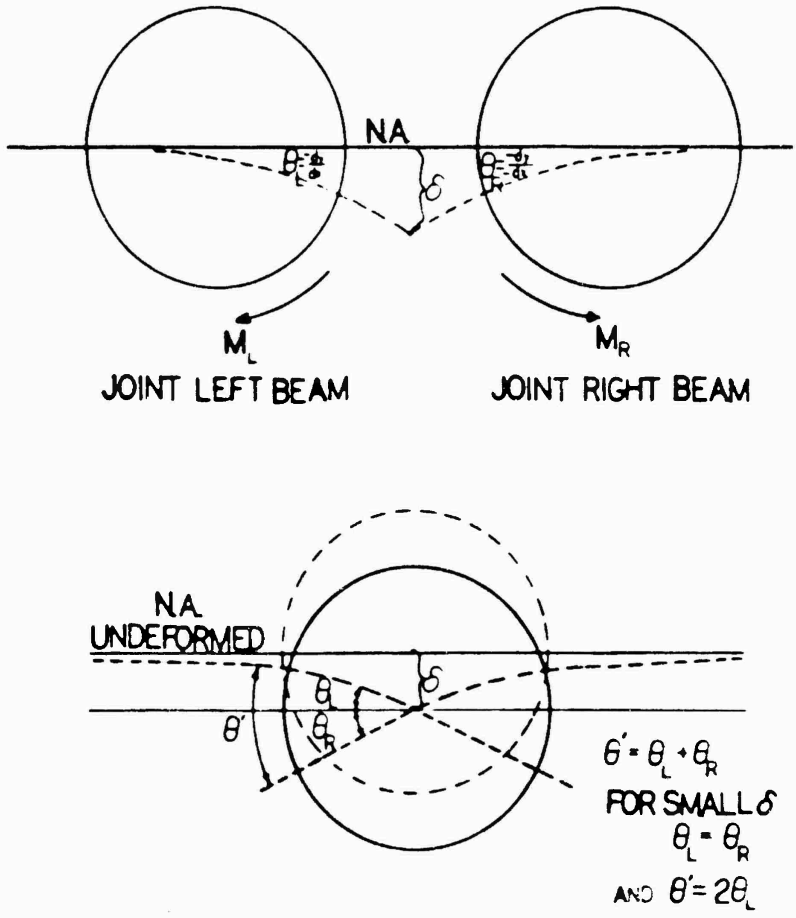


FIGURE 3-15 EXPLODED VIEW OF COULOMB FRICTION JOINT

slip model, is studied for 1 and 1/4 cycles and is divided into the initial loading, the unloading and the reloading phases.

3.3.2 Initial Loading. Before a load is applied to the Coulomb friction joint the following conditions are assumed in the joint. First, the rotation at the joint is zero; second, there is not yet a slipped region in the joint and

the slip radius $a$ equals the joint radius $R$. The boundary conditions at the joint for the entire initial loading phase are:

$$\theta(L) = f(M_{elas}) \qquad (3\text{-}12)$$
$$s(L) = 0$$

where

$M_{elas}$ is from (3-15)

As a load is applied (we will assume an initially positive load without loss of generality) a negative moment, $M_{ext}$, builds up in the joint. The frictional shear stress on the friction interface resists rotation. However, a rotation is present because of the elastic circular shaft assumption for the unslipped region of the joint. The beam undergoes rotation without slip, $a = R$, governed by equation 3-11 until the moment at the joint reaches a value which overcomes the frictional shear stress resisting slip in the joint. This value of moment can be determined by use of the torsion formula as developed in Reference 12:

$$\tau = M\,\rho/J \qquad (3\text{-}13)$$

where

$\tau$ = shear stress
$\rho$ = radius of interest
M = applied moment to shaft
J = polar moment of inertia

Now by making use of the definition of the polar moment of inertia, choosing as $\rho$ the outer radius of the joint $R$ and recalling that initially the joint has no slipped region, $a$

equals $R$, the limit moment for elastic behavior is:

$$M_{ext} = \frac{1}{2} \pi \mu P^* R^3 \qquad (3\text{-}14)$$

where from 3-13

$$\tau = \mu P^*$$
$$M = M_{ext}$$

The moment associated with the limit for elastic behavior is designated $M_{ith}$ and thus for an initial positive load $-M_{ith}$ equals $M_{ext}$. The load $P$ applied to the beam-joint system at $-M_{ith}$ is designated $P_{ith}$ and the rotation $\theta$ is designated $\theta_{ith}$. Figure 3-16 shows the loading, M-$\theta$ curve and friction model for this region of the initial loading phase. If $P_{max} \leq P_{ith}$ then the beam-joint system behaves linearly for the entire load cycle and dissipates zero energy. For the case when $P_{max} > P_{ith}$ the beam-joint system goes into the nonlinear region of the initial loading phase.

As the load increases from $P_{ith}$ to $P_{max}$ the joint develops a region of slip and $a < R$. Equation 3-14 is now generalized for the case when the radius is any radius $a < R$ and the moment associated with the new equation is designated $M_{elas}$. The new equation gives the moment supported by the elastic torsional shaft of radius $a$ as:

$$M_{elas} = \frac{1}{2} \pi \mu P^* a^3 \qquad (3\text{-}15)$$

The moment in the slipped region is found from rearrangement

of equation 2-15 to be:

$$M_{fric} = \frac{2}{3} \pi \mu P^{*}(R^{3}-a^{3}) \qquad (3\text{-}16a)$$

Therefore the entire moment in the joint, $M_{ext}$, from equilibrium of moments is:

$$M_{ext} = -M_{elas} - M_{fric} \qquad (3\text{-}16b)$$

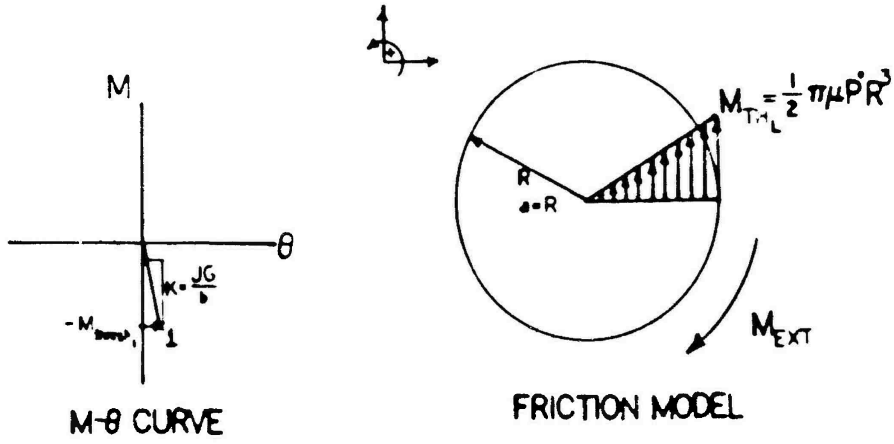


FIGURE 3-16 MICRO-SLIP FRICTION MODEL
INITIAL LOADING ( $P \leq P_{th}$)

The rotation in this region is found from equation 3-11 by setting $M = M_{elas}$ . Making this substitution yields:

$$\theta = \frac{b \mu P^{*}}{a G} \qquad (3\text{-}17)$$

There are several methods of describing the nonlinear region

of M-$\theta$ curve using equations 3-15 through 3-17 and the discussion of a particular method is presented in the discussion of the computer implementation of the micro-slip model.

Figure 3-17 shows the M-$\theta$ curve and friction model for the nonlinear region of the initial loading phase. Notice that if the applied load $P_{max} > P_{gs}$ the entire joint will slip , $a = 0$, and the model reduces to the gross slip model of the joint until $P_{max}$ is reached. Figure 3-18 shows this condition.

Comparing the micro-slip model to the gross slip model we see that the micro-slip model essentially connects the vertical (where here the curve actually has as slope K as defined in equation 3-11 as opposed to vertical) and horizontal lines of the gross slip M-$\theta$ curve with a nonlinear curve where $\theta = f(M)$.

When the applied load reaches $P_{max}$ the load begins to reduce and the frictional shear stress and resulting moment are locked in the joint by setting the boundary condition at the joint to $\theta_{max}$ and setting the slip radius $a = R$.

3.3.3 Unloading. As the applied load reduces to zero and then begins to increase in amplitude in the opposite (negative) direction the joint again undergoes linear rotation, rotation without slip in the joint, defined by equation 3-11 with $M = M_{ext}$. The rotation occurs in the opposite direction to the rotation that occurred in the initial loading. The residual frictional shear stress

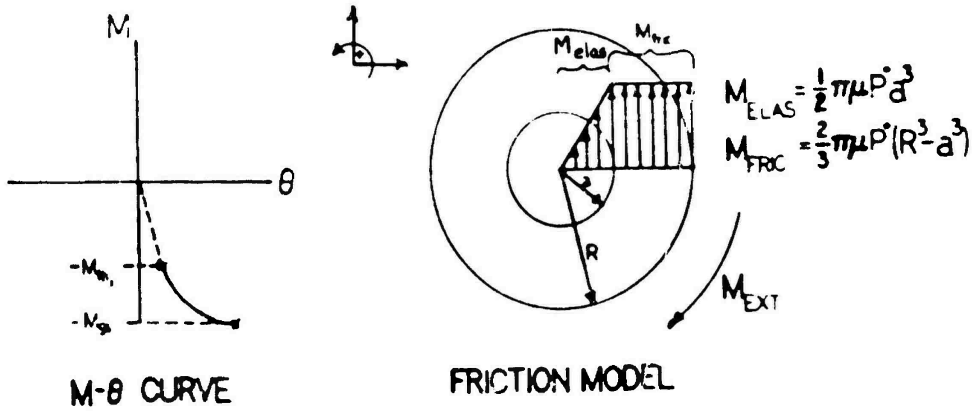


FIGURE 3-17 MICRO-SLIP FRICTION MODEL
INITIAL LOADING ($P_{ith} < P \leq P_{gs}$)

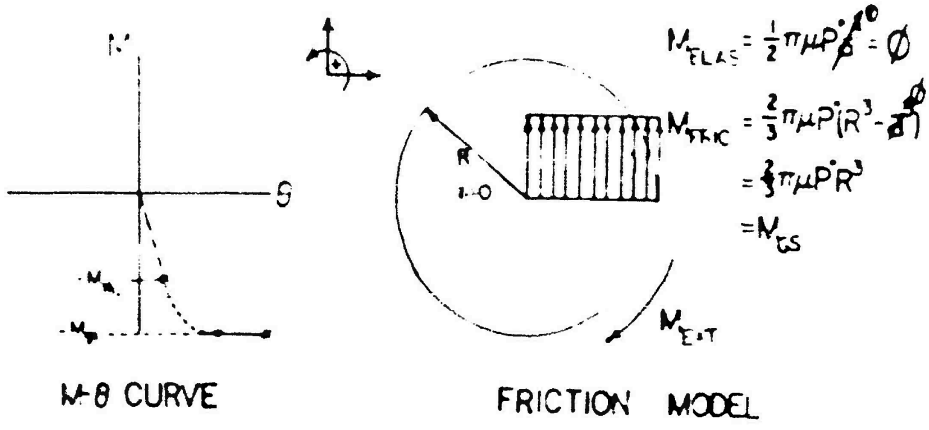


FIGURE 3-18 MICRO-SLIP FRICTION MODEL
INITIAL LOADING ($P_{gs} < P \leq P_{max}$)

allows the slip free rotation to continue until $M_{ext}$ reaches the value $M_{thul}$ defined by the following equation:

$$M_{thul} = -M_{res} + 2M_{th} = \frac{4}{9} \pi \mu P^* R^3 \quad (3\text{-}18)$$

where the joint again begins to slip and $a \leq R$. The load associated with $M_{thul}$ is designated $P_{thul}$. Figure 3-19 shows the M-$\theta$ curve and friction model at the end of the elastic counter rotation.

The moment in the nonlinear region of the unloading phase is found from the following equation:

$$M_{ext} = -M_{res} + 2M_{elas} + 2M_{fric} = \frac{2}{9} \pi \mu P^* R^3 - \frac{4}{9} \pi \mu P^* a^3 \quad (3\text{-}19)$$

and the rotation can be found by use of equation 3-11 with M equal $-2M_{elas}$ to be:

$$\theta = \theta_{max} - \frac{2b \mu P^*}{a G} \quad (3\text{-}20)$$

where here the $\theta_{max}$ term is included to account for the rotation locked in during the initial load phase of the load cycle. Figure 3-20 shows the M-$\theta$ curve and friction model associated with the nonlinear region of the unloading cycle.

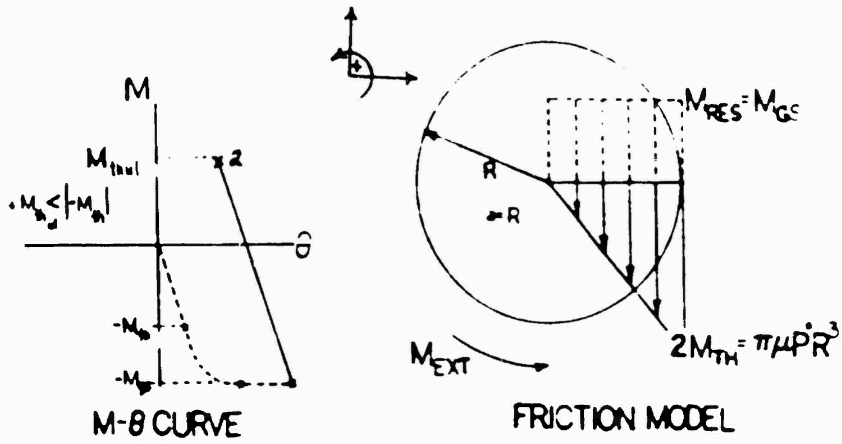


FIGURE 3-19 MICRO-SLIP FRICTION MODEL
UNLOADING ( $P_{thul} \leq P < P_{max}$ )

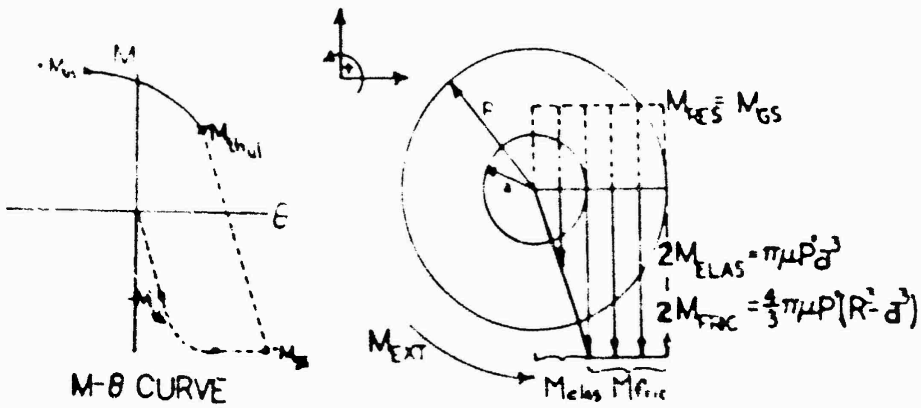


FIGURE 3-20 MICRO-SLIP FRICTION MODEL
UNLOADING ( $P_{thul} > P \geq P_{gs}$ )

Once again if the applied load is such that the loading forces the entire joint to slip, $a = 0$, the model reduces to the gross slip case and that model can be used. The gross slip model is used to calculate rotation at $-P_{max}$ . Figure 3-21 shows the M-$\theta$ diagram and associated friction model at the point where the load has reached $-P_{max}$ and the reload phase is about to begin.

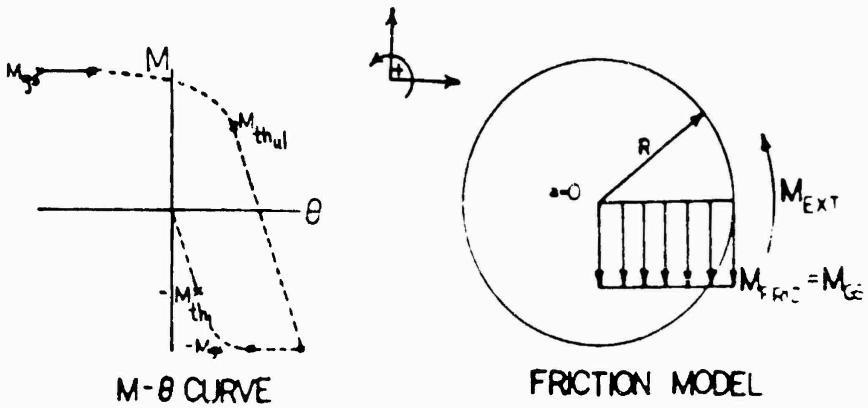


FIGURE 3-21 MICRO-SLIP FRICTION MODEL UNLOADING ($P_{gs} > P \geq -P_{max}$)

It should be pointed out that as the model reaches the point of gross slip behavior the equations which give the rotation in the nonlinear region of both the initial

loading curve and of the unloading curve of the M-$\theta$ diagram are not valid. These equations are based on the assumption of an elastic circular shaft in torsion and when $a$ = 0 this assumption is not valid. The method to find the rotation is presented in the computer implementation section and basically uses a cutoff limit to restrict how far $a$ may move in towards a radius of 0 at the center of the joint.

3.3.4 Reloading. The reloading phase is the antisymmetric case of the unloading phase. At the end of the unloading the rotation is set to a value $\theta_{min}$ and $a = R$ which locks in residual frictional shear stresses and thus causes a residual moment in the joint acting opposite in direction to the residual stress locked in at the end of initial loading. The equations for the moments at the joint are very similar to the unloading case and only differ in sign. The rotation is defined from the locked in value of $\theta_{min}$ and equation 3-11 with $M = M_{elas}$ used to define the rotation in the nonlinear region of the reloading cycle. Finally, for the reloading phase as with the initial loading and unloading phase the equations for $\theta$ are not valid in the gross slip region. Figure 3-22 shows the friction model and the associated equations for the moment acting at the joint for the reloading phase of the load cycle. The moment equation which is in effect can be found by a summation of moments using the sign convention shown. With the entire cycle defined we can move on to the implementation of the micro-slip model on the computer.

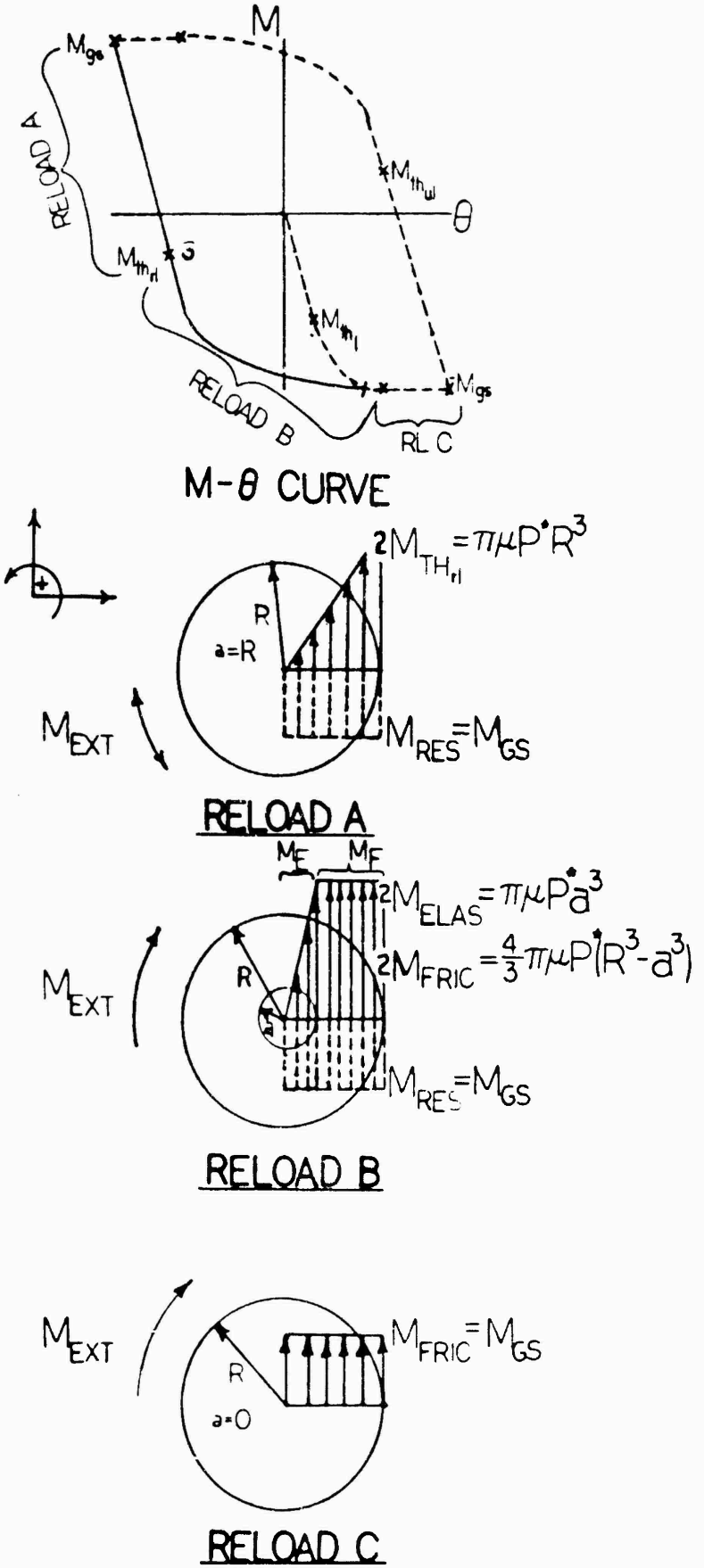


FIGURE 3-22 MICRO-SLIP FRICTION MODEL- RELOAD PHASE

3.3.5 Computer Implementation of The Micro Slip Model. The computer implementation of the micro-slip model is very similar in nature to the implementation of the gross slip model. The calculation of the moment in the nonlinear region of the M-$\theta$ diagram involves an incremental approach in which the value of $a$ is determined based on an increment of the rotation. The process will be laid out in the three different phases of the loading cycle.

3.3.5.1 Initial Loading. The implementation of the code starts by assuming that the load is starting from initial value of zero, the rotation in the joint is zero and $a = R$. The value of the $M_{th}$ is calculated using equation 3-14. The rotation $\theta_{th}$ is determined using equation 3-11 as:

$$\theta_{th} = M_{th} / K \qquad (3\text{-}21)$$

The BEM is used to calculate $P_{th}$. If $P_{max} \leq P_{th}$ then the code will calculate the linear response of the beam-joint system for the entire cycle. If $P_{th} < P_{max}$ point (1) in Figure 3-16 is found.

The next step in the calculation involves describing the nonlinear region of the initial loading curve. The value of $\theta$ is incremented an amount $\Delta\theta$ and the value of $a$ is determined from equation 3-17 in the form:

$$a = \frac{b \mu P^*}{(\theta + \Delta\theta)G} \qquad (3\text{-}22)$$

External moment is determined by equation 3-16b. BEM is used

with the boundary conditions at the right end of $\theta(L) = \theta + \Delta\theta$ and $m(L) = M_{ext}$ as calculated in equation 3-16. The results of the boundary element method are used to determine when to stop incrementing the $\theta$ value. The loop stops if the value of $a$ is within a given tolerance of zero and the code enters a gross slip routine and thus the validity of equation 3-17 is maintained. The loop also stops if the value of the force as given by equation 3-9 exceeds the maximum force amplitude. This latter case is of particular interest as it shows the real advantage of the micro-slip model over the gross slip model.

Figure 3-23 shows the M-$\theta$ curve and P-$\delta$ curve for the initial loading phase of a gross slip model and a micro-slip model. It is easy to see, if the peak load value lies between the load which causes the threshold moment to be exceeded and the load at which the gross slip moment is exceeded, the micro-slip model will dissipate energy while the gross slip model will not.

Irregardless of which test caused the code to jump out of the $\theta$ incrementing loop the code uses the value of $\theta$ at that point and sets it to $\theta_{max}$ . The radius $a$ which has been moving towards 0 is reset to $R$ and $M_{res} = M_{ext}$.

3.3.5.2 Unloading. The next point on the curve that is calculated is point (2) in Figure 3-19. The boundary conditions are set as follows:

$$\theta(L) = \theta_{thul} = \theta_{max} - \frac{2M_{th}}{K}$$
$$m(L) = M_{thul} = M_{res} + 2M_{th} \qquad (3\text{-}23)$$

where equation 3-20 with $a = R$ gives the first boundary condition and equation 3-18 gives the second. The BEM is used to calculate the load, $P_{thul}$, associated with this point. The code again enters a $\theta$ incrementing loop. The equation used to

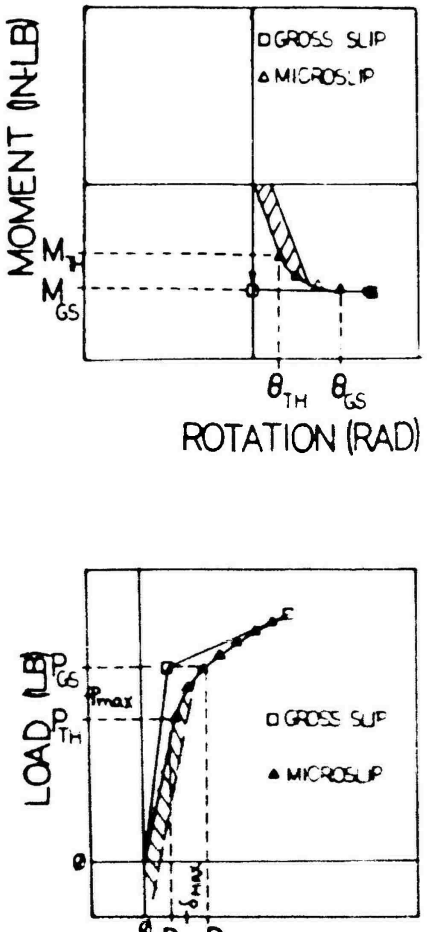


FIGURE 3-23 THE CASE FOR A MICRO-SLIP MODEL

determine $a$ is 3-20. The value of the external moment is determined by equation 3-19. Again the BEM is run after every increment of $\theta$ and the boundary conditions are:

$$\begin{aligned} \theta(L) &= (\theta + \Delta\theta) \\ m(L) &= M_{ext} \end{aligned} \qquad (3\text{-}24)$$

The same two tests are used as in the initial loading phase of the code to determine when looping should end. The computer code sets the value of $\theta = \theta_{min}$ and $M_{res} = M_{ext}$ and the value of $a = R$ again. The code is now prepared to calculate the rest of the loading cycle.

3.3.5.3 Reloading The computer code next calculates the point (3) in Figure 3-22. The associated boundary conditions are:

$$\begin{aligned} \theta(L) &= \theta_{thrl} = \theta_{min} + \frac{2M_{th}}{K} \\ m(L) &= M_{thrl} = M_{res} - 2M_{th} \end{aligned} \qquad (3\text{-}25)$$

The BEM calculates the load associated with these conditions. The code enters the increment on theta for the final time and calculates the nonlinear region of the reloading curve. The governing equations are the negative of the equations 3-19 and 3-20. When the code jumps out of the $\theta$ incrementing loop it has generated the entire hysteresis loop for the loading cycle.

Figure 3-24 shows the general algorithm for the micro-slip model for the time varying applied load. It is general enough that to develop the case for the time varying

displacement the only change that needs to be made to the algorithm is to replace the check on the force with a check on displacement.

As a last point on the micro-slip model for the case of general loading the residual shear stress interference pattern is shown in Figure 3-25. This should be compared to the interference pattern which occurs in the Richardson and Nolle model as shown in Figure 2-8. It is clear that the micro-slip model presented here accounts for an elastic residual shear stress in the beam that Richardson and Nolle do not account for.

The friction models have now been described and the general algorithms presented which model the Coulomb friction joint. Chapter 4 presents the results of some calculations.

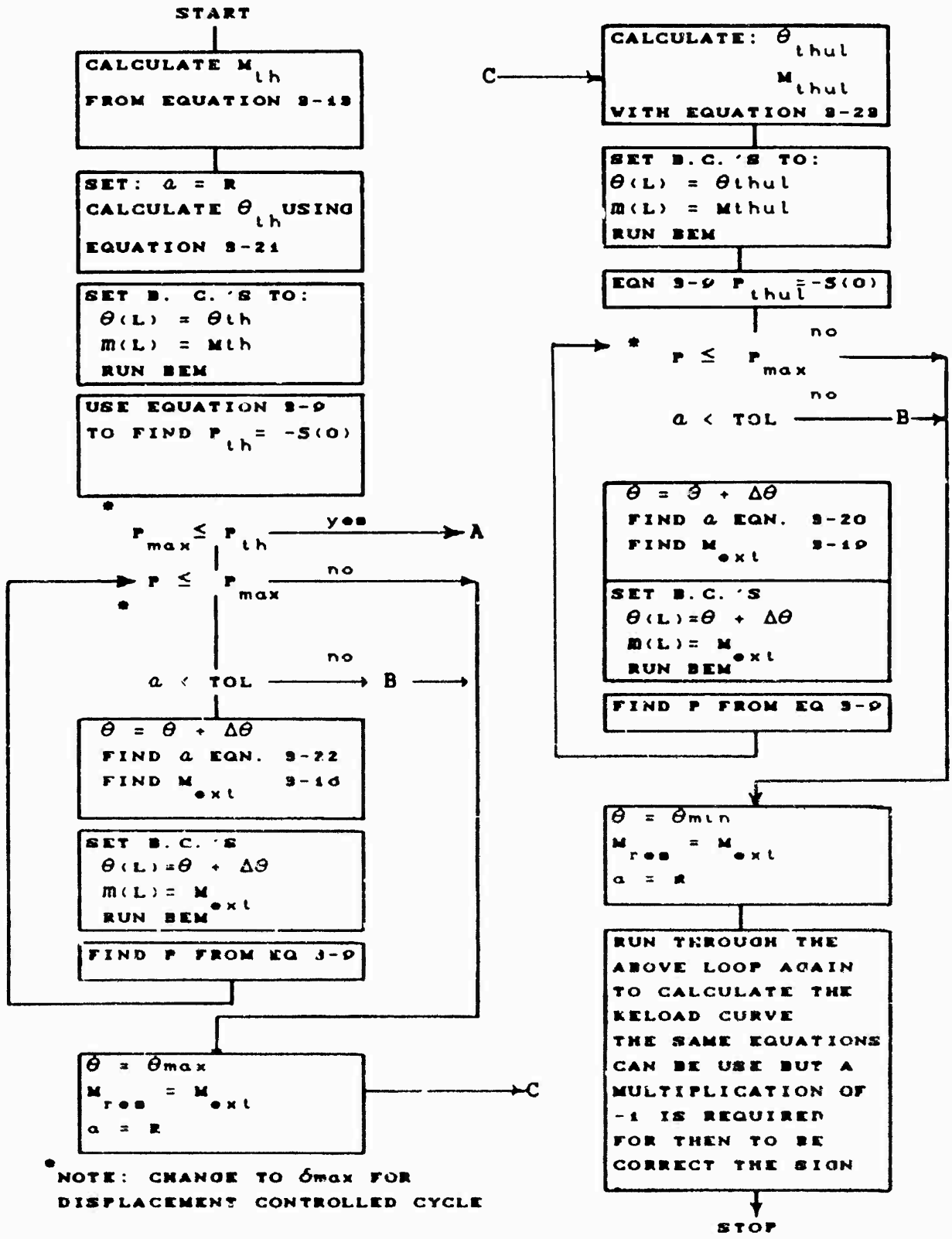


A - LINEAR FOR ENTIRE CYCLE  B - GROSS SLIP MODEL

FIGURE 3-24 GENERAL ALGORITHM FOR MICRO-SLIP MODEL

# IV. Results

## 4.1 Parameters Studied.

The gross slip model and the micro-slip model were used to calculate the energy loss per cycle verses the clamping pressure for both a force controlled and for a displacement controlled system. The applied load or displacement was large enough to force the joint model into the gross slip region. In addition a single case was set up to show the situation where the micro-slip model predicts an energy loss and the gross slip model predicts no loss as discussed in Chapter 3.

The clamping pressure applied at the joint ranges from 0 to 20 Ksi. For a force controlled run the maximum force amplitude applied at the joint is 200 lb. When the displacement control is used the maximum displacement amplitude at the joint is .1 in. The $P$-$\delta$ curve and the M-$\theta$ curve for the force controlled and displacement controlled loading of both the gross slip model and the micro-slip model are presented.

Figures 4.1-4.5 show a comparison of the gross slip model and the micro-slip model $P$-$\delta$ curves for the force controlled loading and displacement controlled loading for increasing values of clamping pressure. It can be seen that the 0.0 Ksi clamping pressure (no-clamp case) reverts

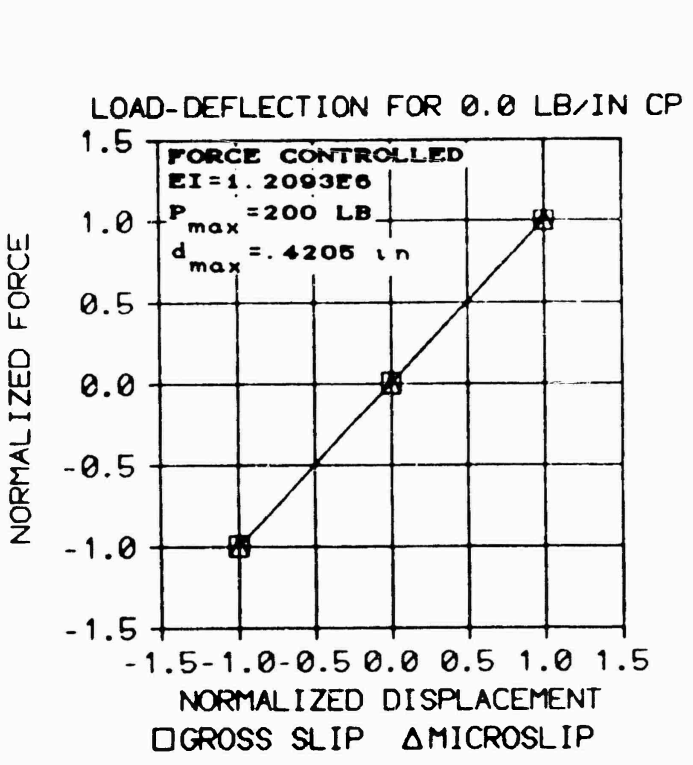


**FORCE CONTROLLED LOADING**

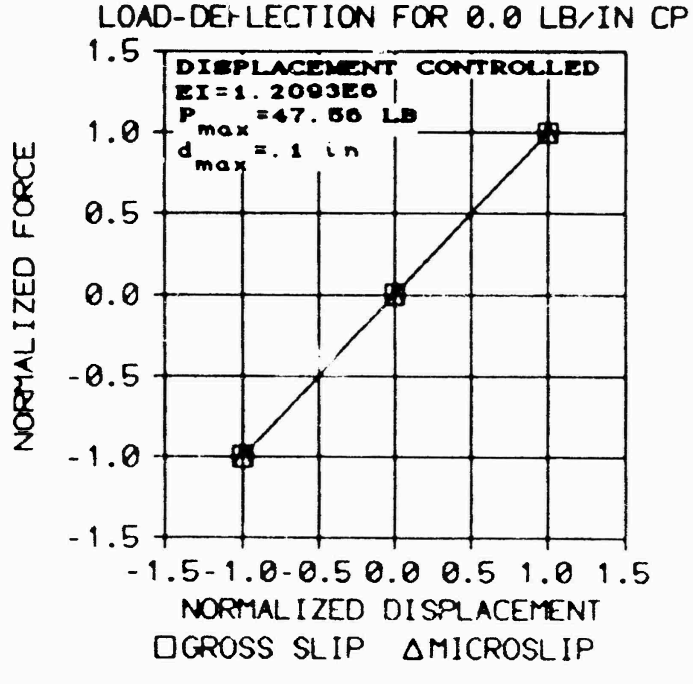


**DISPLACEMENT CONTROLLED LOADING**

**FIGURE 4-1 P-δ CURVES FOR 0 KSI CLAMPING PRESSURE**

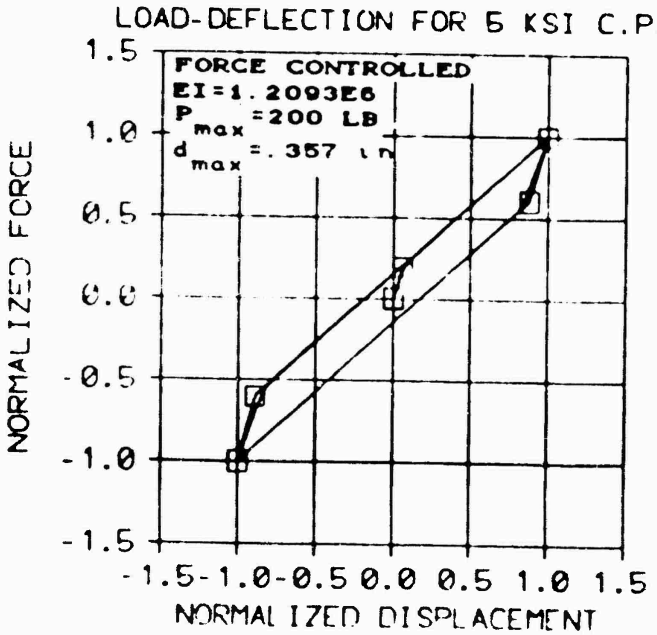


**FORCE CONTROLLED LOADING**

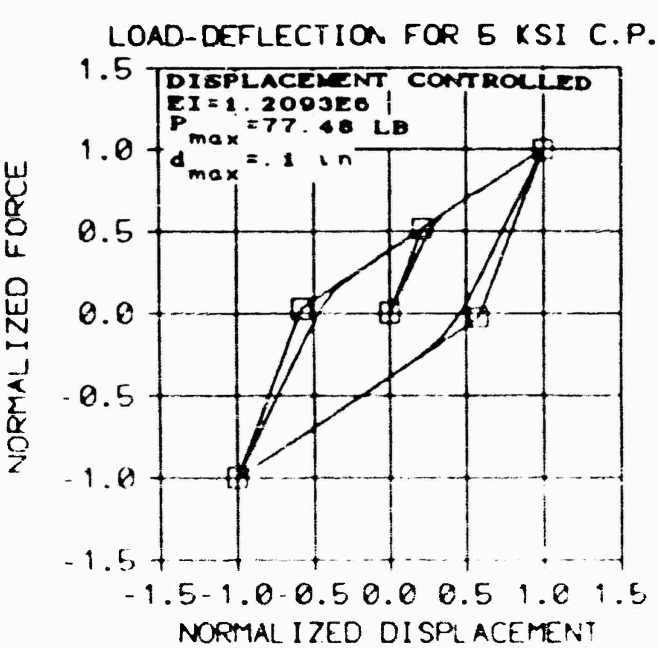


**DISPLACEMENT CONTROLLED LOADING**

**FIGURE 4-2 P-δ CURVES FOR 5 KSI CLAMPING PRESSURE**

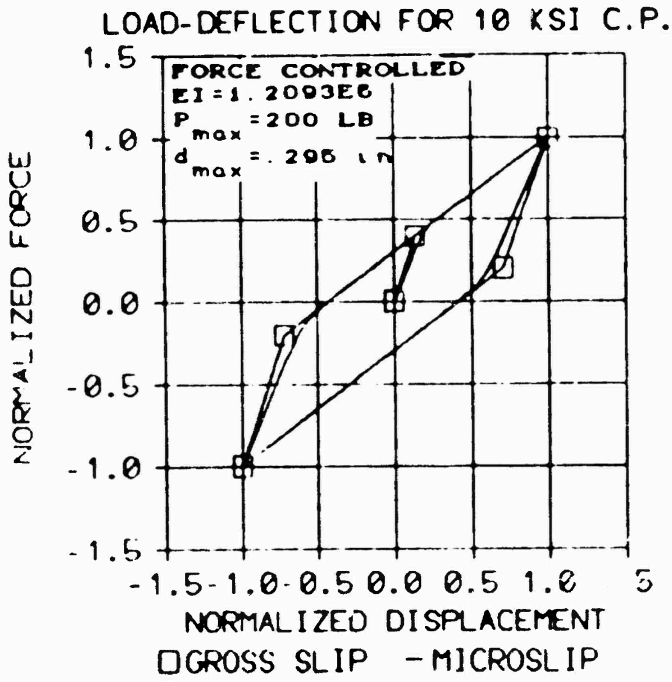


**FORCE CONTROLLED LOADING**

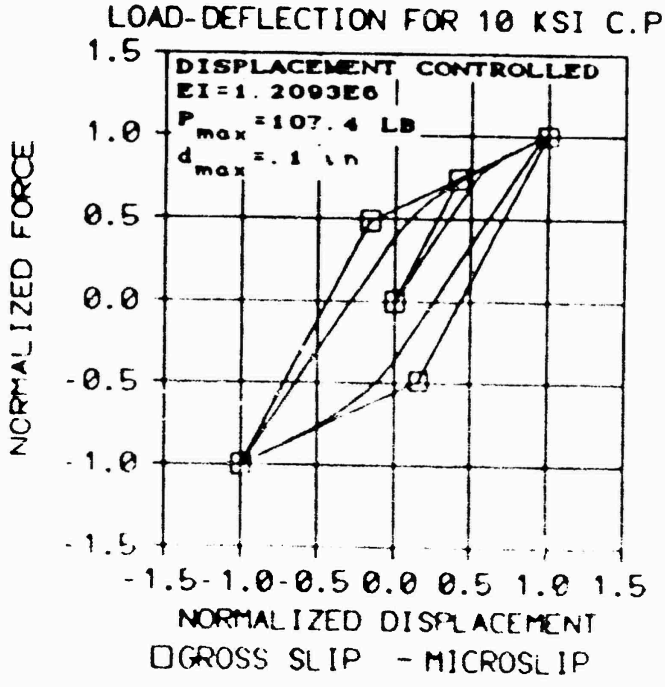


**DISPLACEMENT CONTROLLED LOADING**

**FIGURE 4-3 P-δ CURVES FOR 10 KSI CLAMPING PRESSURE**

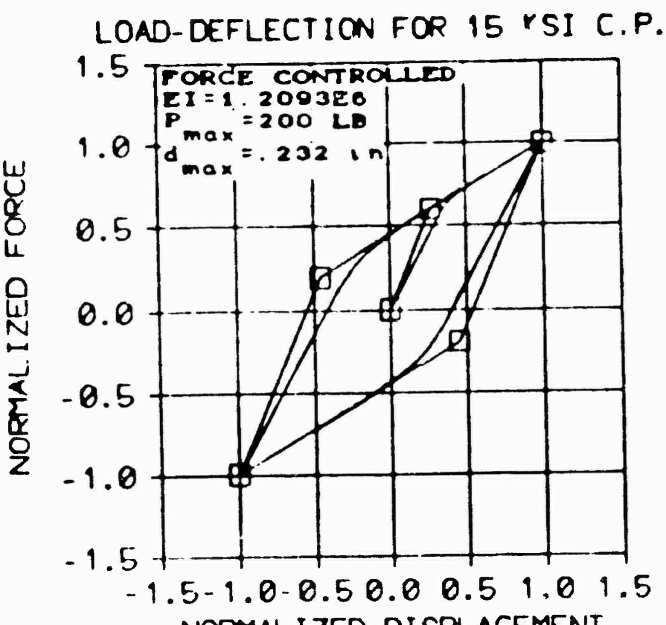


**FORCE CONTROLLED LOADING**

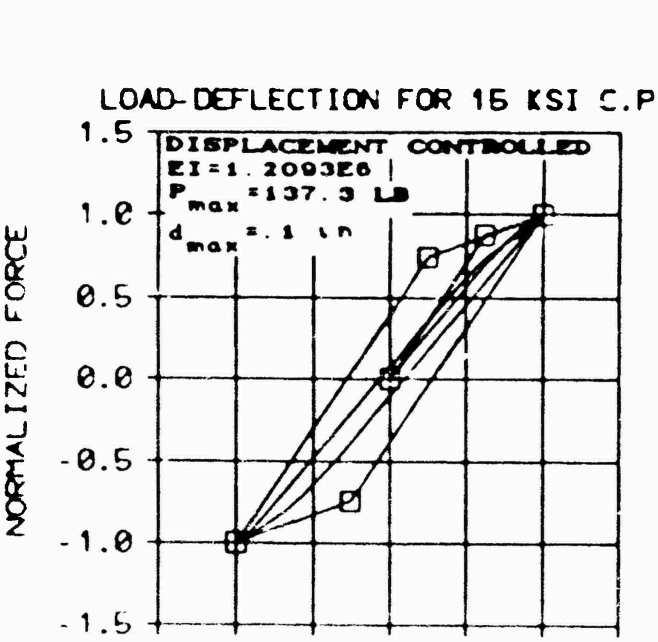


**DISPLACEMENT CONTROLLED LOADING**

**FIGURE 4-4 P-δ CURVES FOR 15 KSI CLAMPING PRESSURE**

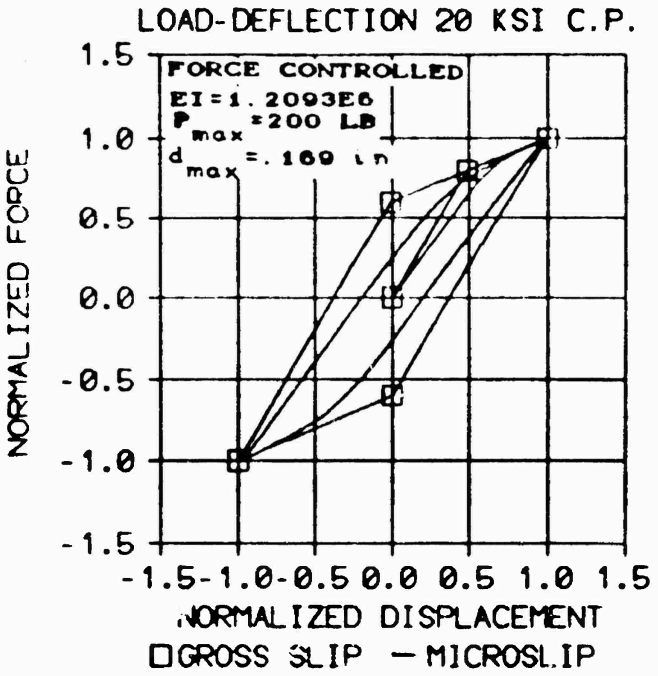


**FORCE CONTROLLED LOADING**

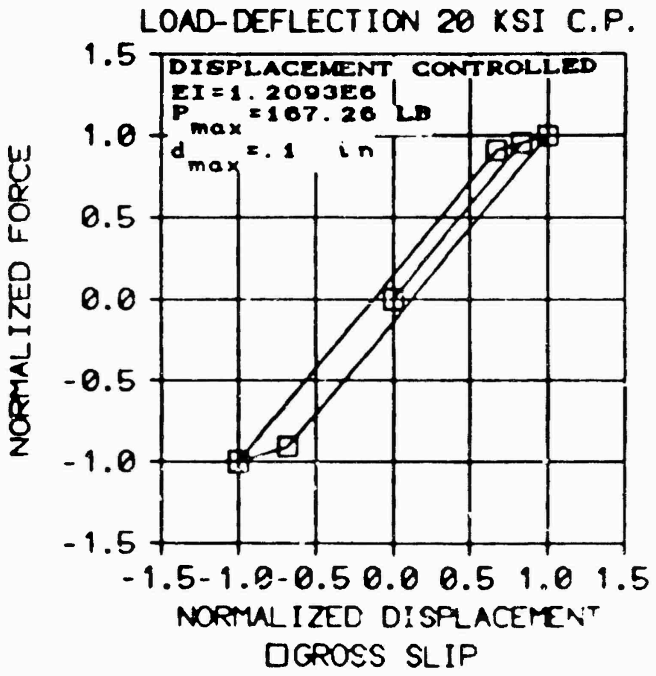


**DISPLACEMENT CONTROLLED LOADING**

**FIGURE 4-5 P-δ CURVES FOR 20 KSI CLAMPING PRESSURE**

to the cantilever beam as presented in the Appendix on pages 105 and 106. At the 20 Ksi load the behavior approaches that of the continuous built in beam (no-slip case) as shown in the Appendix on pages 103 and 104. The region of interest for this analysis is between these two extremes. Figures 4-6 through 4-10 show the M-$\theta$ diagrams that are associated with the P-$\delta$ curves presented in Figures 4-1 through 4-5.

The energy loss per cycle as defined by the area inside the hysteresis loops is calculated for both the gross slip model and the micro-slip model. The curves showing the normalized energy loss as a function of clamping pressure are shown in Figure 4-11 for the displacement controlled and the force controlled loading cycles. The normalization parameter for both cases is the maximum strain energy in the beam for the no-slip case and can be found from the equation:

$$\Delta E_{max} = \frac{1}{2} P_t \delta \qquad (4\text{-}1)$$

where $P_t$ and $\delta$ can be determined as in the Appendix on page 102. It should be noted that the energy loss calculated from the hysteresis loops is only half of the actual energy lost by the entire system since only half the beam system was used to generate the loops. This factor of two was taken into account when generating the curves in Figure 4-11.

The curves in Figure 4-11 show that as the clamping pressure increases from 0 Ksi to 25 Ksi the energy loss per cycle first increases and then decreases. Torvik shows that

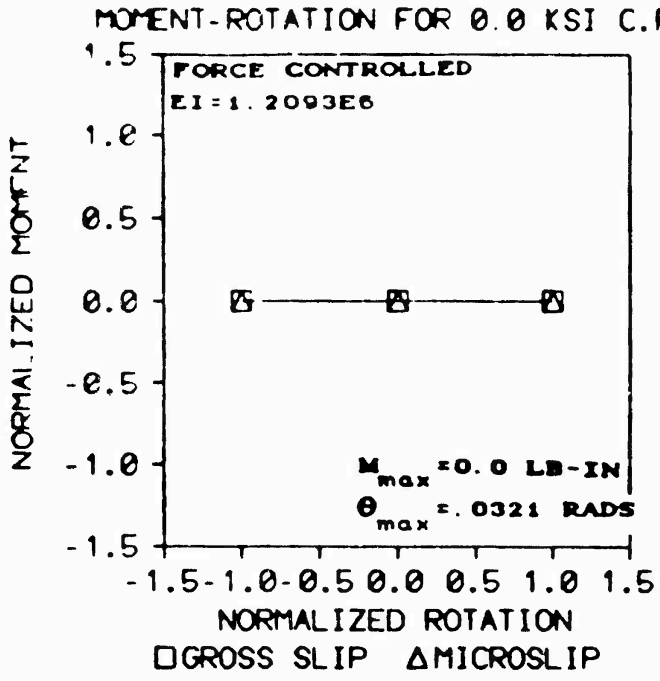


**FORCE CONTROLLED LOADING**

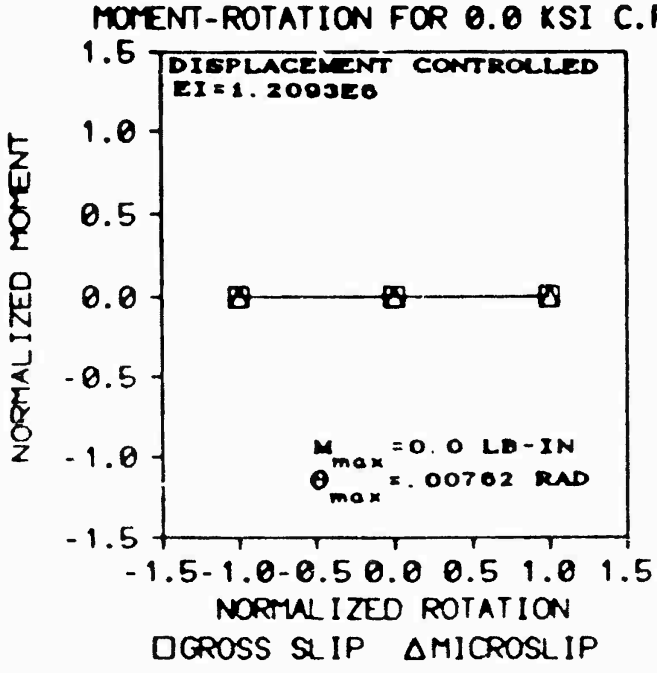


**DISPLACEMENT CONTROLLED LOADING**

FIGURE 4-6 M-$\theta$ CURVES FOR 0 KSI CLAMPING PRESSURE

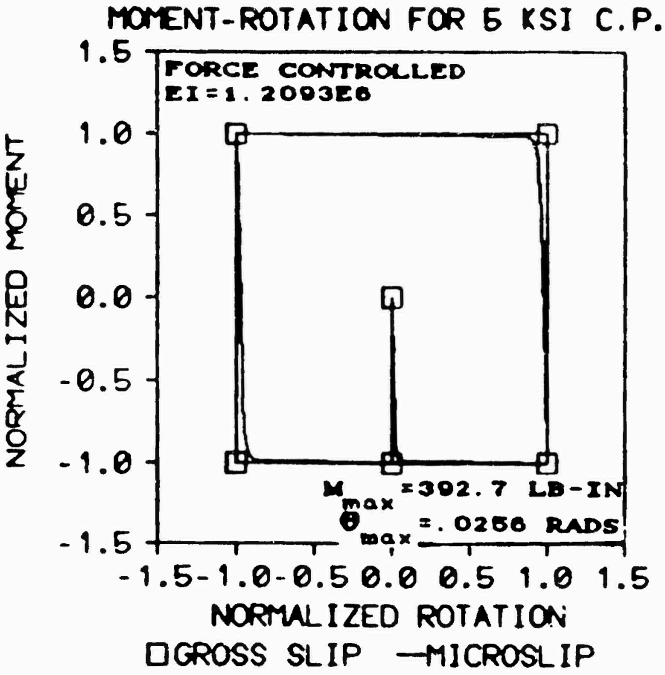


**FORCE CONTROLLED LOADING**

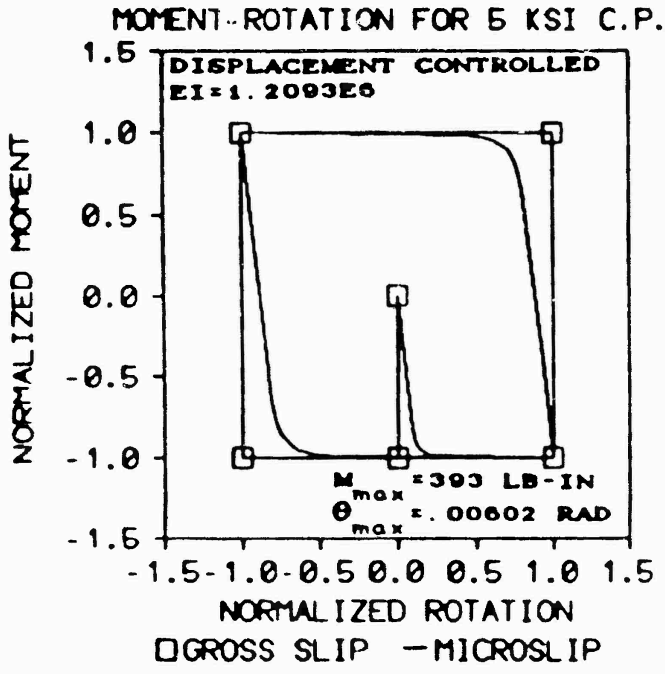


**DISPLACEMENT CONTROLLED LOADING**

FIGURE 4-7 M-θ CURVES FOR 5 KSI CLAMPING PRESSURE

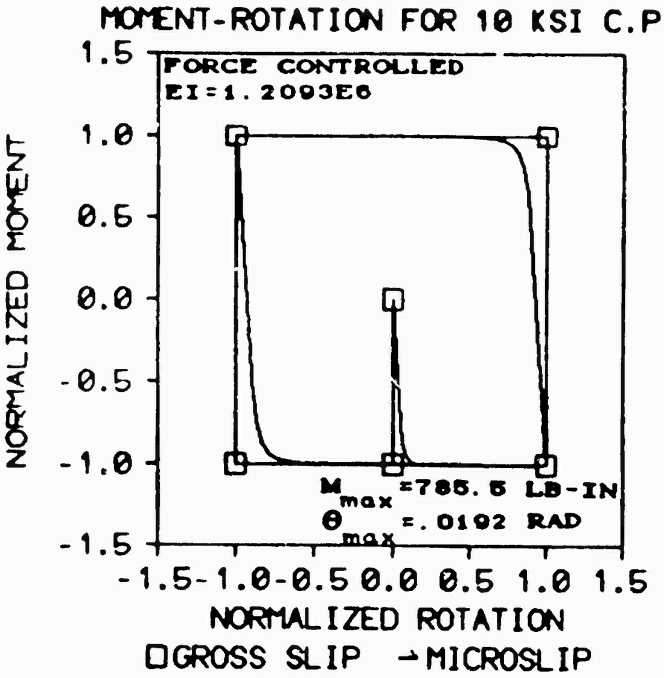


**FORCE CON' .OLLED LOADING**

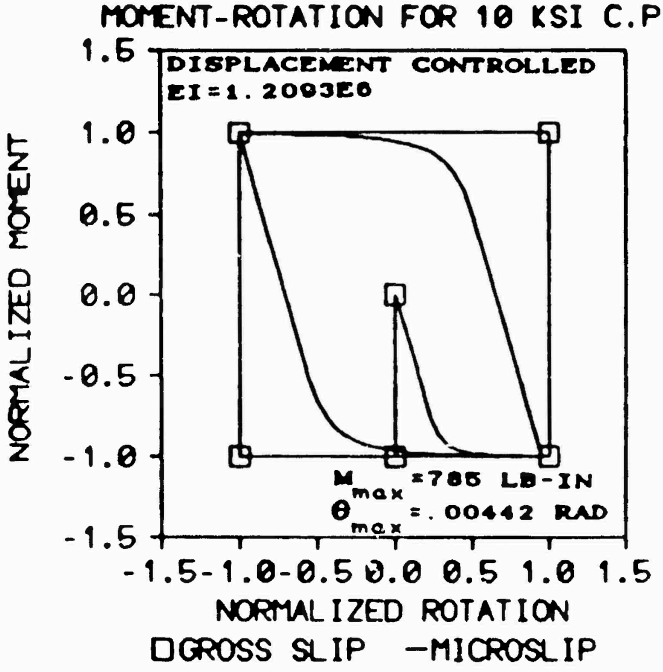


**DISPLACEMENT CONTROLLED LOADING**

**FIGURE 4-8 M-θ CURVES FOR 10 KSI CLAMPING PRESSURE**

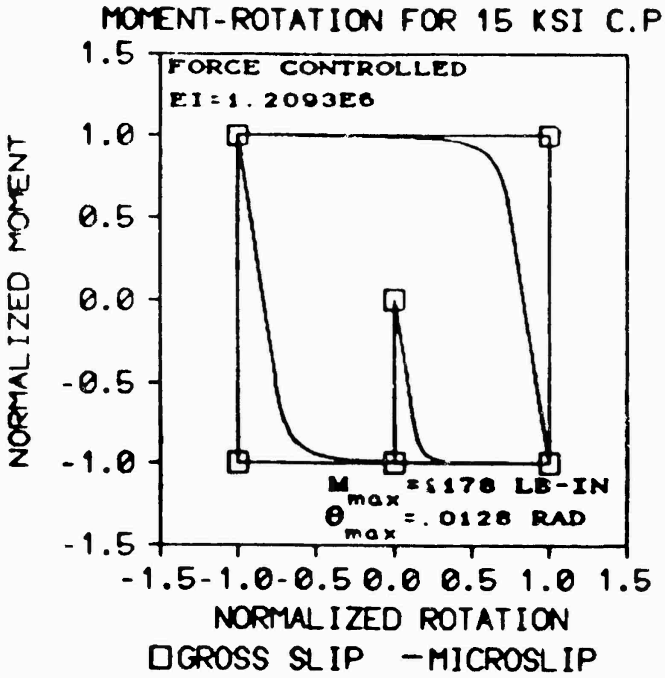


**FORCE CONTROLLED LOADING**

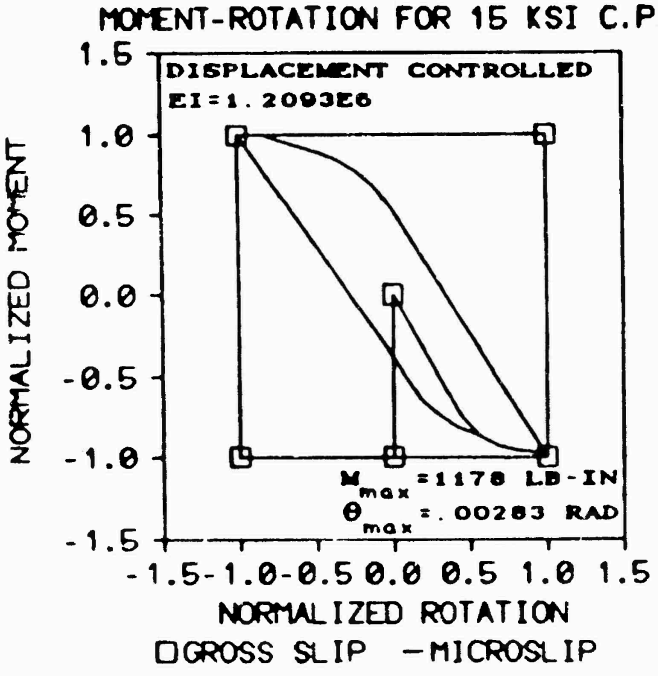


**DISPLACEMENT CONTROLLED LOADING**

**FIGURE 4-9 M-θ CURVES FOR 15 KSI CLAMPING PRESSURE**

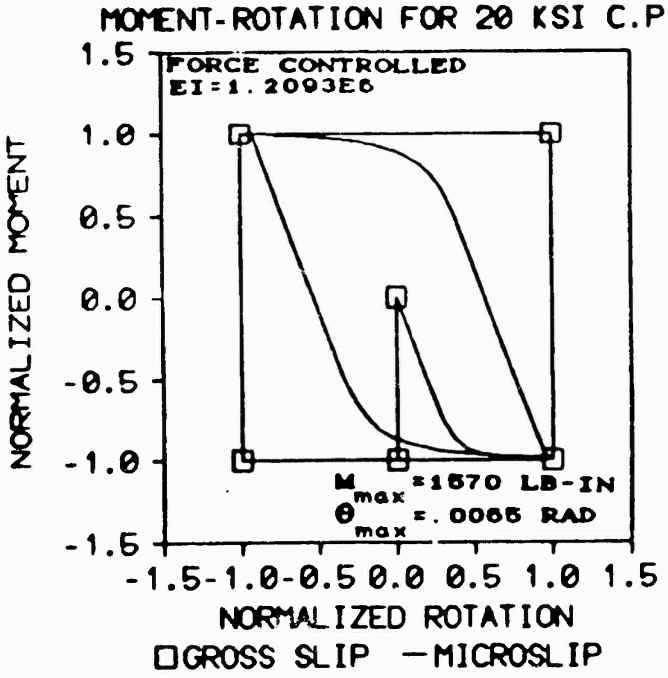


**FORCE CONTROLLED LOADING**

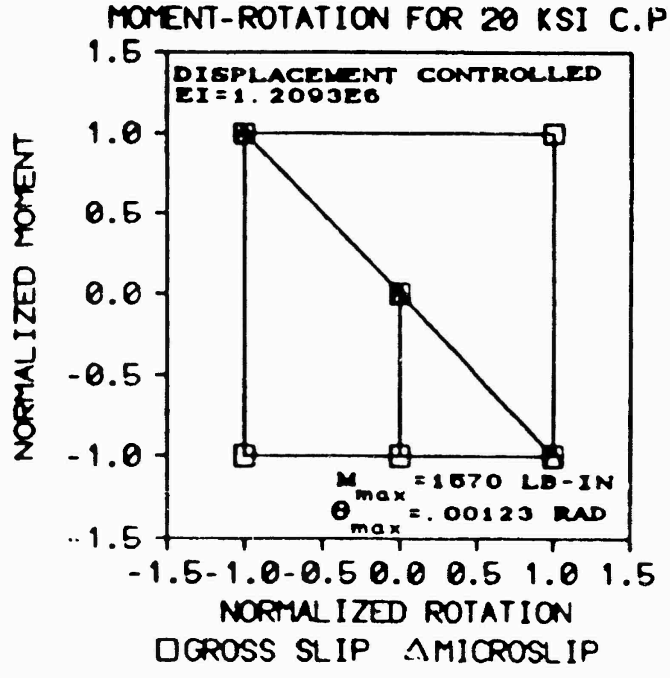


**DISPLACEMENT CONTROLLED LOADING**

**FIGURE 4-10 M-θ CURVES FOR 20 KSI CLAMPING PRESSURE**

the damping is maximized at a clamping pressure just above the clamping pressure required to prevent gross slip (19).

Lazan shows that the low end clamping pressures are dominated by gross slip behavior while the high end clamping pressure is dominated by the micro-slip behavior of joint damping (13). Keeping this in mind, Figure 4-11 shows the point at which the behavior of the slip characteristics are changing from a gross slip dominated behavior to a micro-slip dominated behavior. Since the gross slip model cannot take into account the micro-slip dominated behavior it shows a higher energy dissipation than the micro-slip model which is accounting for the micro-slip behavior in the joint. Figure 4-11 shows that the micro-slip curves and the gross slip curves are identical in the low end clamping pressures where gross slip dominates behavior and at approximately 4-5 Ksi in the displacement controlled and approximately 8-10 Ksi is the force controlled loading cycle the micro-slip dominated behavior begins.

The highest energy dissipation for a given loading case and amplitude of vibration can be determined from the micro-slip curves. This optimum occurs at the peak of the energy dissipation versus clamping pressure curves shown in Figure 4-11.

The displacement controlled loading shows a case where the moment in the friction joint builds up to the value of threshold moment, but in so doing it exceeds the maximum deflection allowed for this loading case. The gross slip

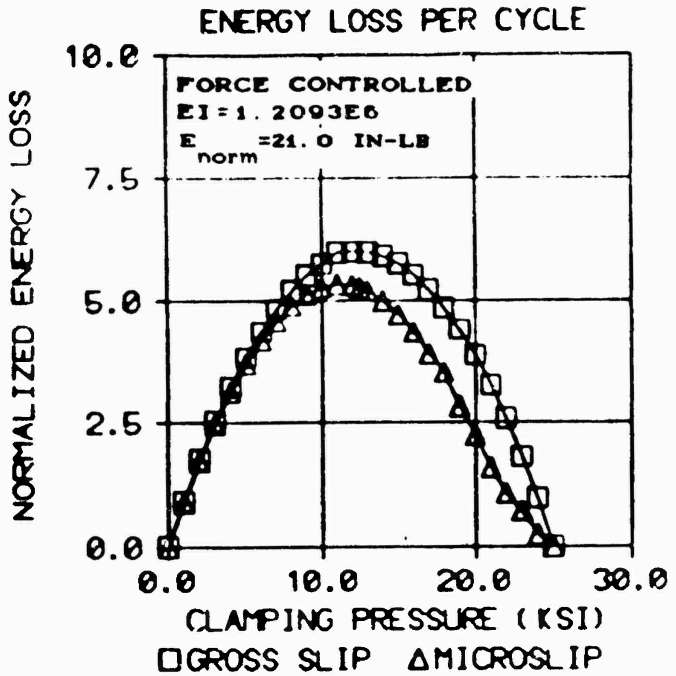


**FORCE CONTROLLED LOADING**

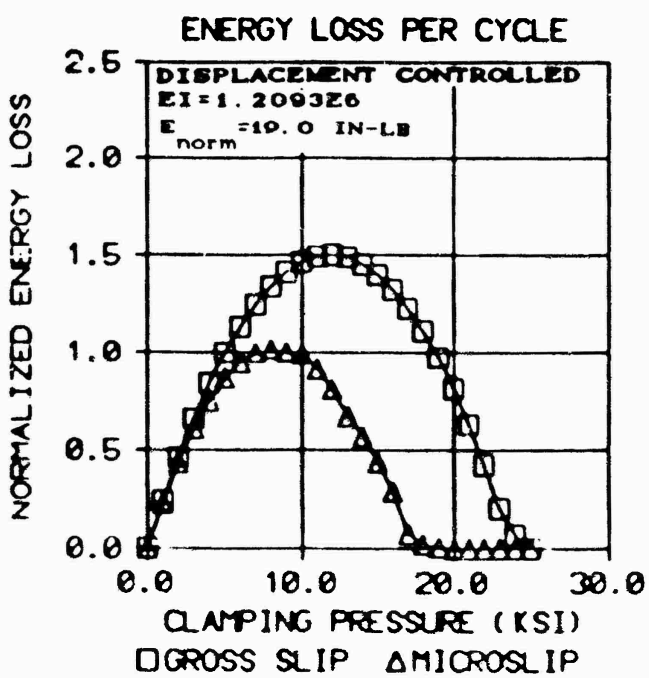


**DISPLACEMENT CONTROLLED LOADING**

**FIGURE 4-11 NORMALIZED ENERGY LOSS PER CYCLE VERSUS CLAMPING PRESSURE**

model however has a steeper $P$-$\delta$ and M-$\theta$ curve and thus reaches a value of $M_{gs}$ before $\delta_{max}$ is reached. For this case Figure 4-11 shows the gross slip model is dissipating energy while the micro-slip model has already gone to zero.

The final remarks to be made in this section deal with the case opposite to the one just discussed. Figure 4-12 shows the case where the micro-slip model is dissipating energy while the gross slip model shows no energy dissipation. This is a major advantage of the micro-slip model over the gross slip model in that energy can be dissipated during low amplitude loading or displacement cycles. This case is presented here as a point of interest and to validate the discussion in section 3. Further study of this feature is left to other investigators.

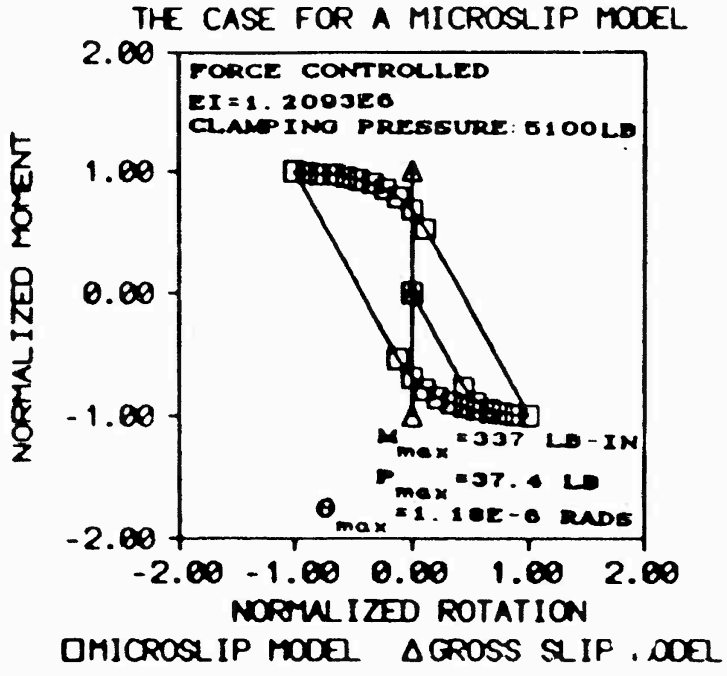


FIGURE 4-12 THE CASE FOR MICRO-SLIP MODEL

# V. Summary and Conclusions

## 5.1 Summary.

The objective of this thesis was to develop a better model of the damping in structural joints due to dry friction when slip occurs in the joint. In Chapter 1 the motivation for the thesis was put forward and the method to meet the objective outlined.

In Chapter 2 the appropriate theory was introduced which served as the underlying foundation for the prediction of the friction at the structural joint. The micro-slip friction model of Richardson and Nolle was outlined as a method to predict the friction response at the joint. However, the assumption that the unslipped region of the joint behaves as a rigid body was seen to be to restrictive and a method to account for the moment carrying capacity of the unslipped region of the joint was developed.

Chapter 2 also served to introduce the Boundary Element Method of the beam joint analysis. The results of the BEM analysis of several beam geometries and loading conditions was confirmed from a simple beam theory analysis of the identical problem. Results from the BEM calculations of several geometries and loadings are presented in Appendix A.

Chapter 3 introduced and discussed in some detail the gross slip model and the micro-slip model of joint behavior.

Here the method of assuming the unslipped region behaves as an elastic shaft under torsional loading, was developed. The length, *b*, of the torsional shaft was assumed to be the width of one of the beams. This length was arbitrarily chosen as a first approximation in the analysis process. The algorithms to carry out the analysis of both micro-slip and gross slip friction models in both a force controlled and displacement controlled loading were developed.

In Chapter 4 the results of the actual computer runs were presented. The energy loss versus clamping pressure plots follow the expected trend of increasing from zero at the no-clamp case up to some maximum energy loss at some "optimum" clamping pressure and then continuing back to zero at the no-slip case.

## 5.2 Conclusions.

The following conclusions are drawn from this thesis:

1. A one-dimensional indirect Boundary Element Method computer code has been developed to calculate the response of free span beams. The code is general enough to allow for concentrated and distributed loads as well as concentrated moments. The code calculates the shear, moment, rotation and displacement at any location in the beam and produces files with which shear and moment diagrams can be plotted. Based on the literature search conducted, a boundary element code for free span beams was not in existence before this thesis was started.

2. The BEM code was modified to calculate moment-rotation

friction damping in a structural joint. Either force controlled or displacement controlled loading can be specified.

3. A new micro-slip model of Coulomb friction damping in structural joints was developed. The model, depending on the applied moment, allows for elastic rotation of the joint up to a breakaway or threshold moment where partial slip begins. As the applied moment increases, the region of partial slip grows until the entire joint is slipping.

4. The new model of micro-slip Coulomb friction was implemented in the BEM code. Once again, either force controlled or displacement controlled loading of the joint is allowed.

5. The results of computer calculations show that the micro-slip model behaves in a similar manner to previously published reports and data. The variation of energy loss per cycle versus clamping pressure, for both the gross slip model and the micro-slip model, shows that a clamping pressure which yields the greatest energy loss per cycle for the given loading case and amplitude response, does exist.

6. Compared to the gross slip model, the micro-slip model developed herein gives more accurate results of damping behavior for values of applied moment both above and below the gross slip moment value.

7. The micro-slip model developed herein is more accurate than the Richardson and Nolle model in that it accounts for the existence of a threshold moment below which the behavior is elastic and the energy lost due to Coulomb friction damping is zero.

# VI. Recommendations

This thesis has presented two novel ideas in the analysis of the Coulomb friction damping, first, the analysis of the beam joint system using the boundary element method; second, the assumption of a circular shaft under torsional loading in the region where the joint has not slipped, and as a result many new questions and ideas have arisen. Many areas for investigation and development have opened up. Some additional work could be completed in the following areas:

1. A major assumption in this analysis was the assumed length of the elastic circular shaft, *b*. As a first approximation *b* was chosen to be the width of one of the beams connected at the joint. Studies need to be made to determine if this length is correct or if a more accurate length can be found. Suggested studies are:
    a. A parametric study to determine the sensitivity of the micro-slip model to this parameter.
    b. A three-dimensional stress analysis of the Coulomb friction joint to determine the correct value of *b*.
2. The present model should be investigated further to study the nature of the hysteresis loops for the case where the joint dissipates energy in micro slip without extending into the gross slip region.

3. The development of a truly dynamic Coulomb friction damping model based on the one dimensional BEM.

4. A variation of the clamping pressure with radius should be implemented to account for nonuniform pressure distribution as a result of bolting or riveting of the joint.

5. A variation of the coefficient of friction over time should be implemented to account for the wear of the contact surfaces that results from Coulomb friction damping.

6. An experimental analysis of the two-beam model should be accomplished in order to experimentally verify the micro-slip model. Equation 2-9 relates the energy loss per cycle to the difference in successive peaks of a vibrating system with Coulomb friction damping, and could be used in conjunction with experimental data to verify the micro-slip model.

## Appendix: BEM Baseline Solutions

### ** BUILT-IN BEAM PROBLEM **

THIS IS BEM RUN W/O FRICTION

Young's Modulus = .29e+8 psi
Moment of Inertia = .0417 $in.^4$
Length = 39.370 $in.^4$
Epsilon = .000001 in.

Point Load At x = 19.685 in.
Load = 400.0 lb.

BOUNDARY CONDITONS:

***LEFT END***

DISPLACEMENT = 0
SLOPE = 0

***RIGHT END***

DISPLACEMENT = 0
SLOPE = 0

SELECTED OUTPUT POINTS

**** X = .000****
DISPLACEMENT = -.5551E-15
RO TA T I ON = -.9527E-17
M O M E N T = .1969E+04
S H E A R = -.2000E+03

**** X = 19.685****
DISPLACEMENT = .1051E+00
RO TA T I ON = .6511E-07
M O M E N T = -.1968E+04
S H E A R = -.2000E+03

**** X = 39.370****
DISPLACEMENT = .1117E-15
RO TA T I ON = .2604E-16
M O M E N T = .1969E+04
S H E A R = .2000E+03

PROBLEM GEOMETRY

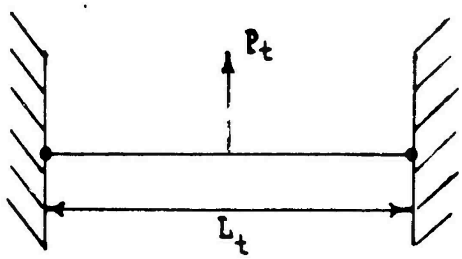


SHEAR DIAGRAM

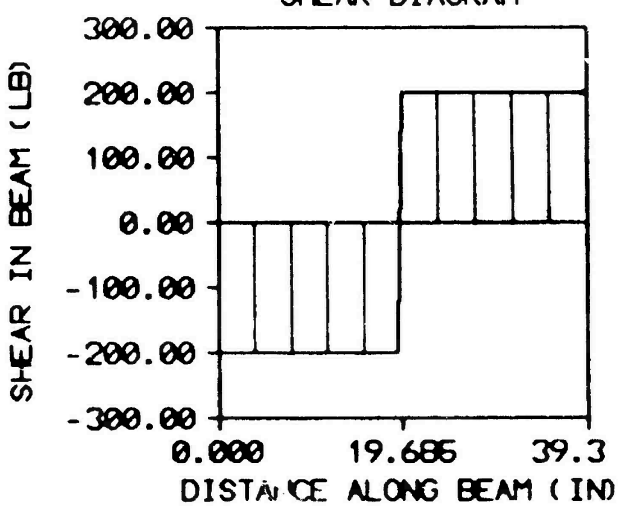


MOMENT DIAGRAM

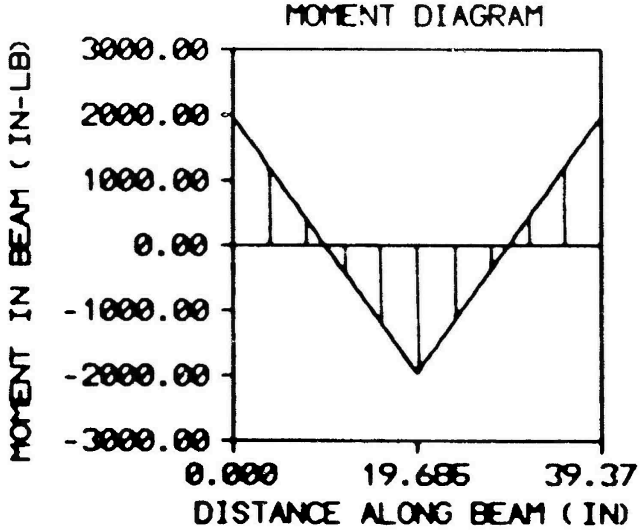

** BUILT-IN BEAM PROBLEM **

SYMMETRIC GEOMETRY
FORCE CONTROLLED LOADING

THIS IS BEM RUN W/O FRICTION

Young's Modulus = .29e+8 psi
Moment of Inertia = .0417 $in.^4$
Length = 19.685 $in.^4$
Epsilon = .000001 in.

Point Load At x = 19.685 in.
Load = 200.0 lb.

BOUNDARY CONDITONS:

***LEFT END***

DISPLACEMENT = 0
SLOPE = 0

***RIGHT END***

SLOPE = 0
SHEAR = 0

SELECTED OUTPUT POINTS

**** X = .000****
DISPLACEMENT = .0000E+00
ROTATION = .0000E+00
MOMENT = .1969E+04
SHEAR = -.2000E+03

**** X = 19.685****
DISPLACEMENT = .1051E+00
ROTATION = .3469E-17
MOMENT = -.1968E+04
SHEAR = .0000E+00

PROBLEM GEOMETRY

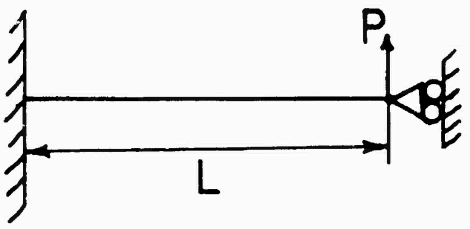


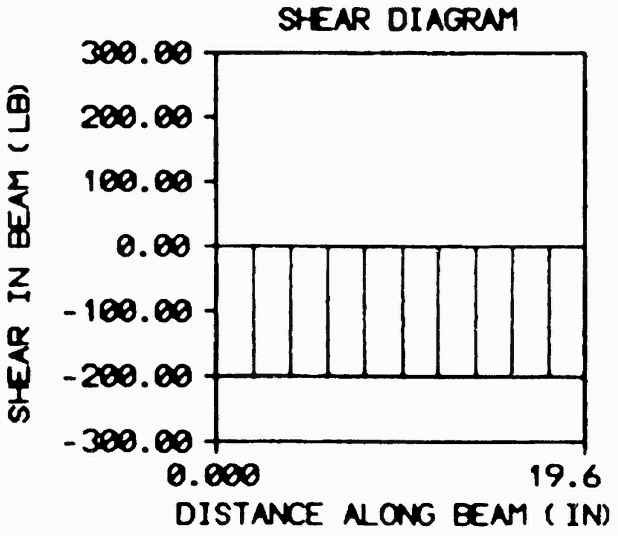


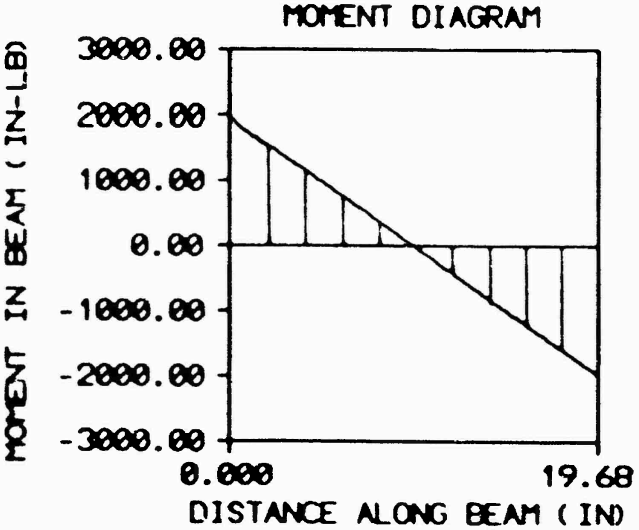

** BUILT-IN BEAM PROBLEM **

SYMMETRIC GEOMETRY
DISPLACEMENT CONTROLLED LOADING

THIS IS BEM RUN W/O FRICTION

Young's Modulus = .29e+8 psi
Moment of Inertia = .0417 $in.^4$
Length = 19.685 $in.^4$
Epsilon = .000001 in.

PROBLEM GEOMETRY

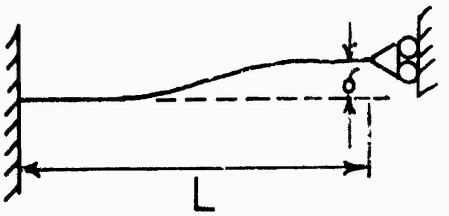


Point Load At x = 19.685 in
Load = 0.0 lb

BOUNDARY CONDITONS:

***LEFT END***

DISPLACEMENT = 0
SLOPE = 0

***RIGHT END***

DISPLACEMENT = .10
SLOPE = 0

SELECTED OUTPUT POINTS

**** X = .000****
DISPLACEMENT = .0000E+00
ROTATION = .0000E+00
MOMENT = .1872E+04
SHEAR = -.1902E+03

**** X = 19.685****
DISPLACEMENT = .1000E+00
ROTATION = -.1735E-17
MOMENT = -.1872E+04
SHEAR = -.1902E+03

SHEAR DIAGRAM

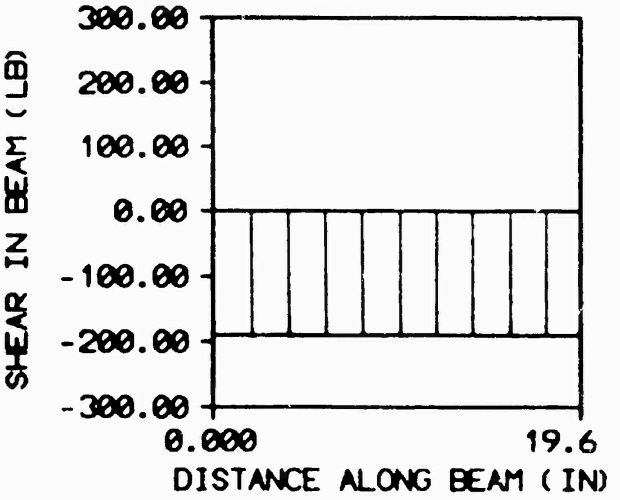


MOMENT DIAGRAM

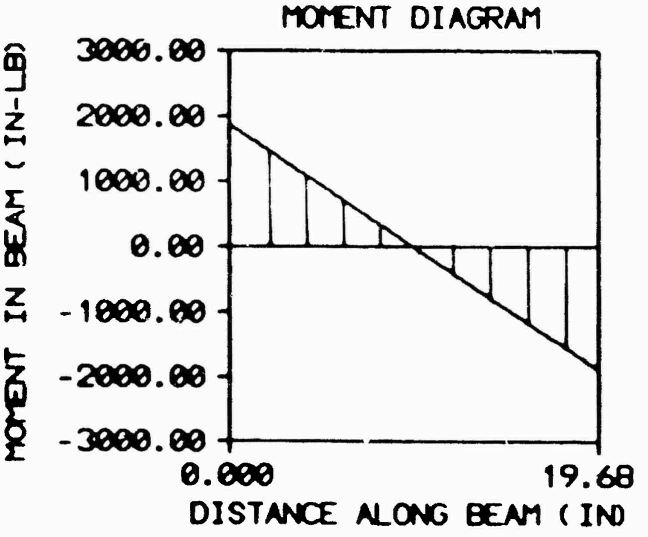

** CANTILEVER BEAM PROBLEM **

FORCE CONTROLLED LOADING

THIS IS BEM RUN W/O FRICTION

Young's Modulus = .29e+8 psi
Moment of Inertia = .0417 $in.^4$
Length = 19.685 $in.^4$
Epsilon = .000001 in.

Point Load At x = 19.685 in.
Load = 200.0 lb.

PROBLEM GEOMETRY

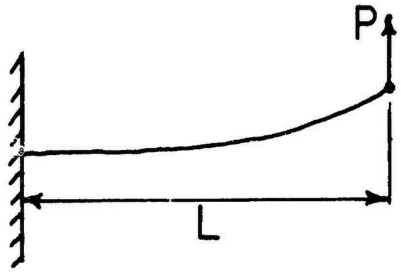


BOUNDARY CONDITONS:

***LEFT END***

DISPLACEMENT = 0
SLOPE = 0

***RIGHT END***

MOMENT = 0
SHEAR = 0

SELECTED OUTPUT POINTS

**** X = .000****
DISPLACEMENT = .0000E+00
RO TA T I ON = -.1577E-17
M O M E N T = .3937E+04
S H E A R = -.2000E+03

**** X = 19.685****
DISPLACEMENT = .4205E+00
RO TA T I ON = .3204E-01
M O M E N T = -.3411E-12
S H E A R = .0000E+00

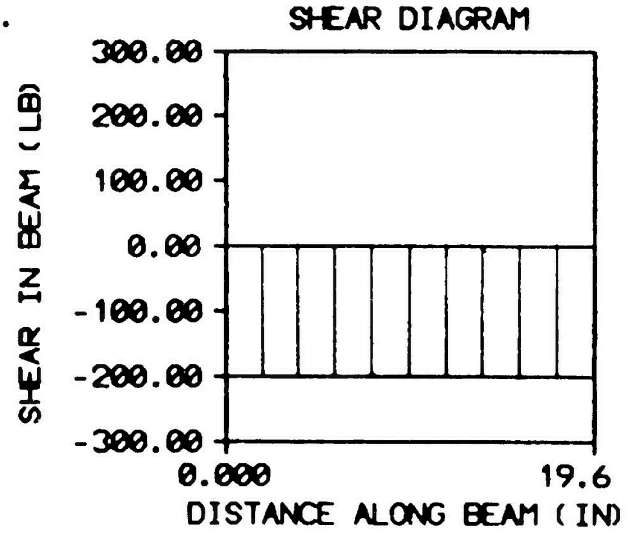


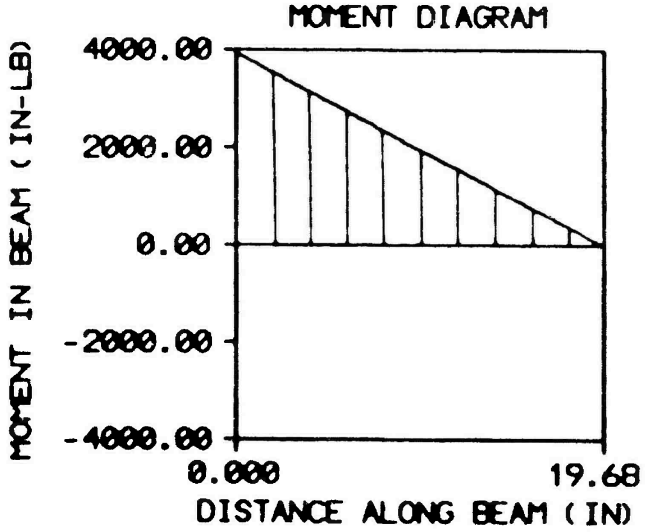

** CANTILEVER BEAM PROBLEM **

DISPLACEMENT CONTROLLED LOADING

THIS IS BEM RUN W/O FRICTION

Young's Modulus = .29e+8 psi
Moment of Inertia = .0417 $in.^4$
Length = 19.685 $in.^4$
Epsilon = .000001 in.

PROBLEM GEOMETRY

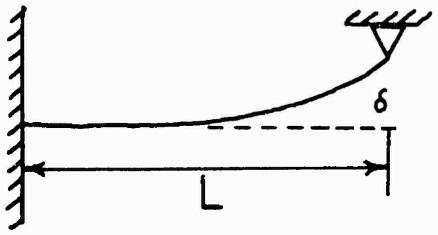


Point Load At x = 19.685 in
Load = 0.0 lb

BOUNDARY CONDITONS:

***LEFT END***

DISPLACEMENT = 0
SLOPE = 0

***RIGHT END***

DISPLACEMENT = .10
MOMENT = 0

SELECTED OUTPUT POINTS

**** X = .0000****
DISPLACEMENT = .0000E+00
RO TA T I ON = -.4418E-18
M O M E N T = .9362E+03
S H E A R = -.4756E+02

**** X = 19.685****
DISPLACEMENT = .1000E+00
RO TA T I ON = .7620E-02
M O M E N T = -.5684E-13
S H E A R = -.4756E+02

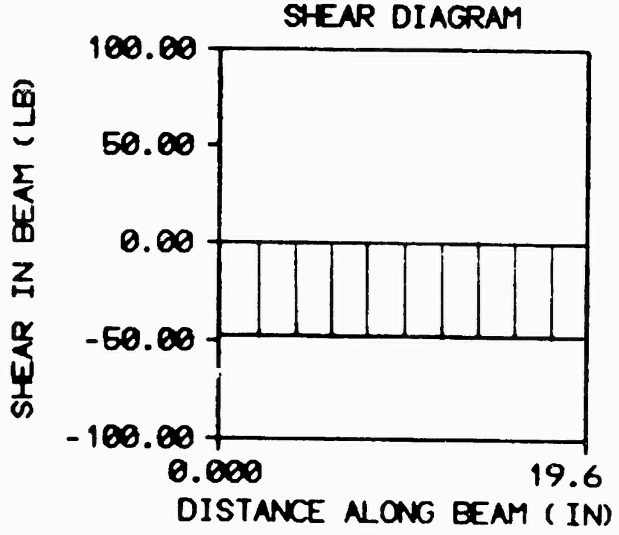


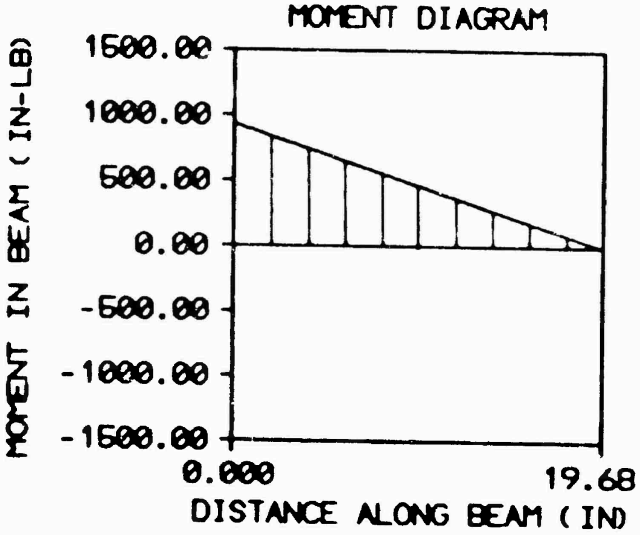

** BUILT-IN BEAM PROBLEM **

DISTRIBUTED LOAD LOADING

THIS IS BEM RUN W/O FRICTION

Young's Modulus = .29e+8 psi
Moment of Inertia = .0417 $in.^4$
Length = 39.370 $in.^4$
Epsilon = .000001 in.
Distributed Load

From x = 0
To x = 39.370

Uniform Load = 10.0 lb/in

PROBLEM GEOMETRY

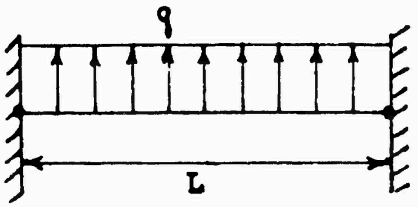


BOUNDARY CONDITONS:

***LEFT END***

DISPLACEMENT = 0
SLOPE = 0

***RIGHT END***

DISPLACEMENT = 0
SLOPE = 0

SELECTED OUTPUT POINTS

**** X = .000****
DISPLACEMENT = -.4996E-15
RO TA T I ON = .1093E-16
M O M E N T = .1292E+04
S H E A R = -.1969E+03

**** X = 19.685****
DISPLACEMENT = .5174E-01
RO TA T I ON = .7469E-17
M O M E N T = -.6456E+03
S H E A R = .1865E-13

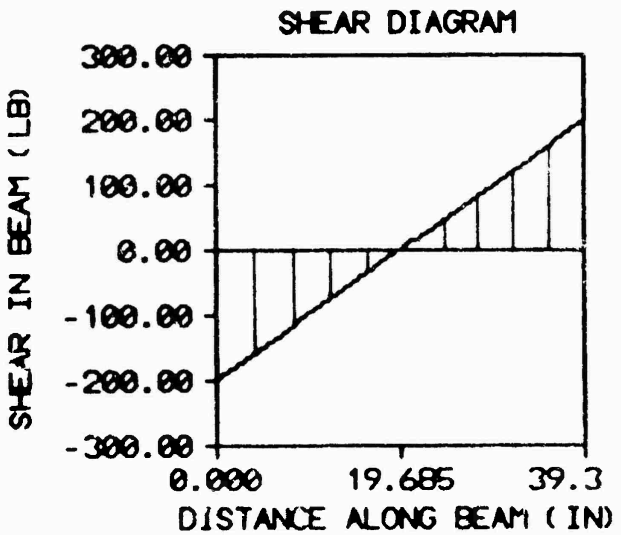


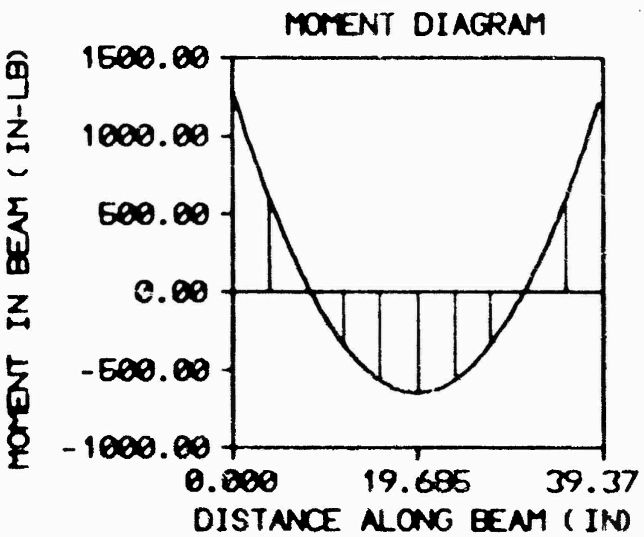

** BUILT IN BEAM PROBLEM **

SYMMETRIC GEOMETRY
DISTRIBUTED LOAD LOADING

PROBLEM GEOMETRY

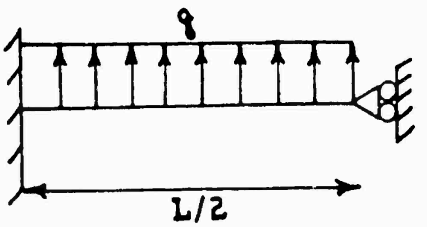


THIS IS BEM RUN W/O FRICTION

Young's Modulus = .29e+8 psi
Moment of Inertia = .0417 $in.^4$
Length = 19.685 $in.^4$
Epsilon = .000001 in.
Distr buted Load

From x = 0
To x = 19.68

Uniform Load = 10 lb/in

BOUNDARY CONDITONS:

***LEFT END***

DISPLACEMENT = 0
SLOPE = 0

***RIGHT END***

SLOPE = 0
SHEAR = 0

SELECTED OUTPUT POINTS

**** X = .000****
DISPLACEMENT = -.4996E-15
RO TA T I ON = .1093E-16
M O M E N T = .1292E+04
S H E A R = -.1969E+03

**** X = 19.685****
DISPLACEMENT = .5174E-01
RO TA T I ON = .7469E-17
M O M E N T = -.6456E+03
S H E A R = .0000E-00

SHEAR DIAGRAM

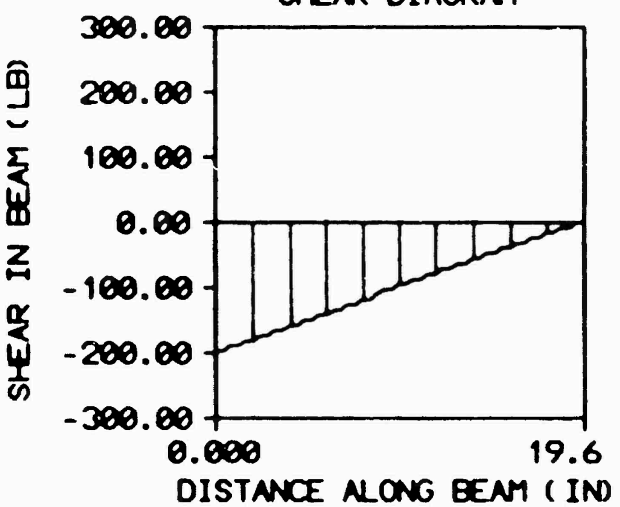


MOMENT DIAGRAM

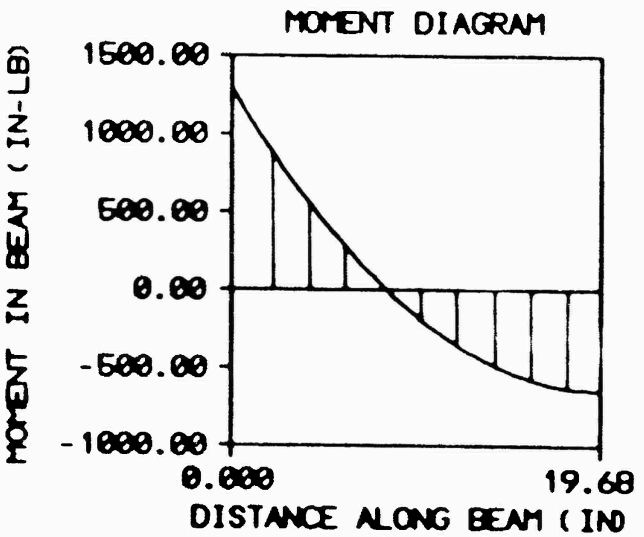

## Bibliography


1. Allen, David H., Introduction to Aerospace Structural Analysis, USA, John Wiley and Sons, INc., 1985.

2. Ashley, Holt, "On Passive Damping Mechanisms in Large Space Structures," Journal of Spacecraft, Vol 21(5): 448-455, 1984.

3. Beards, C. F., "Damping in Structural Joints," Shock and Vibration Digest, Vol 11(9): 35-41, 1979.

4. Beards,C. F., "Some Effects of Interface Preparation on Frictional Damping in Joints," International Journal of Machine Tool Design and Research, Vol 15: 77-85, 1975.

5. Beards, C. F., Williams, J.L., "The Damping of Strucural Vibration by Rotational Slip in Joints," Journal of Sound and Vibration, Vol 53(3): 333-340, 1977.

6. Bannerjee, P. K., Butterfield R., Boundary Element Methods in Engineering Science, London, McGraw-Hill Book Company (UK) Limited, 1981.

7. Brebbia, C. A., The Boundary Element Method for Engineers, New York, John Wiley and Sons, Inc., 1978.

8. Donnelly, Capt Robert P., The Effect of Energy Dissipation Due To Friction At The Joint of a Simple Beam Structure. MS Thesis, AFIT/GAE/AA/85d-5. School of Engineering, Air Force Institute of Technology (AU). Wright-Patterson AFB OH, December 1985.

9. Greenwood, D. T., Principles of Dynamics, New Jersey, Prentice-Hall, Inc., 1965.

10. Griffel, William, Beam Formulas, New York, Frederick Ungar Publishing Co., 1979.

11. Henderson, John P., Jones, David I., Nashie, Ahid D., Vibration Damping, USA, John Wiley and Sons, Inc., 1985.

12. Higdon, Archie, Ohlsen, Edward H., Stiles, William B.,Mechanis of Materials, USA, John Wiley and Sons, Inc., 1960.

13. Lazan, B. J., "Review of Structural Damping Mechanisms," Wright Air Development Center Technical Report 59-676, 1961.

14. Meirovitch, L., Elements of Vibration Analysis, USA, McGraw-Hill, Inc., 1975.

15. Richardson, R. S. H., Nolle, H., "Energy Dissipation in Rotary Structural Joints," Journal of Sound and Vibration, Vol 54(4): 577-588, 1977.

16. Shugar, T. A., Cox, J. V., "An Investigation Of The Indirect Boundary Element Method In One and Two-Dimensional Elastostatics," Naval Civil Engineering Laboratory Technical Note N-1664, 1983.

17. Thomson, William T., Theory of Vibrations With Applications, 2nd Ed., New Jersey, Prentice-Hall, Inc., 1981.

18. Torvik, P. J., "Damping: Its Application In Transportation Vehicles," Materials on the Move, Vol 6, 1974.

19. Ungar, E. E., "The Status of Engineering Knowledge Concerning The Damping of Built-Up Structures," Journal of Sound and Vibration, Vol 26(1): 141-154, 1973.

# Vita

PII Redacted

Gregory L. Leiker was born [redacted] He graduated [redacted], [redacted] On 2 June 1982 he received a B. S. in Engineering Mechanics from the United States Air Force Academy. He was stationed at Kirtland AFB, Albuquerque, N.M. at the Air Force Weapons Lab in the Civil Engineering Research Division where he held the job of Research Structural Engineer. In May of 1985 he came to the Air Force Institute of Technology to pursue a M. S. Degree in Aeronautical Engineering.

He married [redacted].

[redacted] PII Redacted

UNCLASSIFIED
SECURITY CLASSIFICATION OF THIS PAGE

AD-A177 111

# REPORT DOCUMENTATION PAGE

Form Approved
OMB No. 0704-0188

| | |
|---|---|
| 1a. REPORT SECURITY CLASSIFICATION<br>UNCLASSIFIED | 1b. RESTRICTIVE MARKINGS |
| 2a. SECURITY CLASSIFICATION AUTHORITY | 3. DISTRIBUTION/AVAILABILITY OF REPORT<br>Approved for public release; distribution unlimited |
| 2b. DECLASSIFICATION/DOWNGRADING SCHEDULE | |
| 4. PERFORMING ORGANIZATION REPORT NUMBER(S)<br>AFIT/GAE/AA/86D-9 | 5. MONITORING ORGANIZATION REPORT NUMBER(S) |
| 6a. NAME OF PERFORMING ORGANIZATION<br>School of Engineering<br>6b. OFFICE SYMBOL (If applicable)<br>AFIT/EN | 7a. NAME OF MONITORING ORGANIZATION |
| 6c. ADDRESS (City, State, and ZIP Code)<br>Air Force Institute of Technology<br>Wright Patterson AFB, Ohio 45433 | 7b. ADDRESS (City, State, and ZIP Code) |
| 8a. NAME OF FUNDING/SPONSORING ORGANIZATION<br>8b. OFFICE SYMBOL (If applicable) | 9. PROCUREMENT INSTRUMENT IDENTIFICATION NUMBER |
| 8c. ADDRESS (City, State, and ZIP Code) | 10. SOURCE OF FUNDING NUMBERS<br>PROGRAM ELEMENT NO. / PROJECT NO / TASK NO / WORK UNIT ACCESSION NO |

11. TITLE (Include Security Classification)
IMPROVED MODELING OF STRUCTURAL JOINT DAMPING (UNCLASSIFIED)

12. PERSONAL AUTHOR(S)
Gregory L. Reiker, CAPT, USAF

| 13a. TYPE OF REPORT | 13b. TIME COVERED | 14. DATE OF REPORT (Year, Month, Day) | 15. PAGE COUNT |
|---|---|---|---|
| MS Thesis | FROM _____ TO _____ | 1986 December | 111 |

16. SUPPLEMENTARY NOTATION

| 17. COSATI CODES | | | 18. SUBJECT TERMS (Continue on reverse if necessary and identify by block number) |
|---|---|---|---|
| FIELD | GROUP | SUB-GROUP | Damping, Joint Damping, Friction Damping Coulomb Damping, Boundary Element Method Micro-slip |
| 13 | 05 | | |
| | | | |

19. ABSTRACT (Continue on reverse if necessary and identify by block number)

Thesis Advisor: Terry D. Hinnerichs, MAJOR, USAF
Department of Aeronautics and Astronautics

Approved for public release: IAW AFR 190-1.
13 March 87
Director of Research and Consultant Development
Air Force Institute of Technology (AU)
Wright-Patterson AFB OH 45433

| 20. DISTRIBUTION/AVAILABILITY OF ABSTRACT | 21. ABSTRACT SECURITY CLASSIFICATION |
|---|---|
| ☐ UNCLASSIFIED/UNLIMITED ☑ SAME AS RPT ☐ DTIC USERS | UNCLASSIFIED |
| 22a. NAME OF RESPONSIBLE INDIVIDUAL<br>Terry D. Hinnerichs, MAJOR, USAF | 22b. TELEPHONE (Include Area Code)<br>513-255-3069 |
| | 22c. OFFICE SYMBOL<br>AFIT/ENY |

DD Form 1473, JUN 86 — Previous editions are obsolete — SECURITY CLASSIFICATION OF THIS PAGE

UNCLASSIFIED

Block 19

The purpose of this thesis is to develop a better model of damping that occurs in structural joints due to coulomb friction when rotational slip occurs in the joints. A one-dimensional, indirect formulation, of the Boundary Element Method (BEM) is developed to calculate the displacement, rotation, moment and shear in beams which obey the assumptions of simple beam theory. This BEM code is then modified to account for friction damping at the joint of two beams due to a relative rotation between them. A gross slip model of the friction in the joint is used to establish basic behavior of the beam joint with friction damping. Next, a micro-slip model of friction is developed. The micro-slip model, depending on the applied moment, allows for the elastic rotation of the joint up to some threshold moment where partial slip begins. As the applied moment increases the region of partial slip expands until the entire joint is slipping and the gross slip condition exists.

Both the gross slip model and the micro-slip model of the joint friction are used to obtain measures of energy loss per cycle versus clamping pressure in the joint. Load controlled and deflection controlled loading cycles are used to exercise the joint in a quasi-dynamic model and generate hysteresis loops in both force-diplacement and moment-rotation space.

The clamping pressure was varied between 0 Ksi and 20 Ksi. The energy loss per cycle curves generated show that there is a range of clamping pressures for which the energy loss per cycle curve reaches a peak for a given loading and amplitude of vibration.

The micro-slip model developed herein shows better behavior than the gross slip model both above and below the moment which causes gross slip. The hysteresis loops generated in both the load-deflection and moment-rotation space are comparable to other published data, however the allowance for the breakaway moment before partial slip begins seems to give a more conservative estimate of the energy loss per cycle for a given clamping pressure.